

Alma Mater Studiorum – Università di Bologna

DOTTORATO DI RICERCA IN  
Scienze Chimiche

Ciclo XXVI

**Settore Concorsuale di afferenza:** 03/A2

**Settore Scientifico disciplinare:** CHIM/02

**Advanced lithium battery chemistries for  
sustainable transportation**

**Presentata da:** *Simone Monaco*

**Coordinatore Dottorato**

*Prof. Aldo Roda*

**Relatore**

*Prof.ssa Marina Mastragostino*

**Correlatore**

*Dott.ssa Francesca Soavi*

**Esame finale anno 2014**







# Abstract

The practical specific energy of lithium-ion batteries (LIBs), which are the most advanced rechargeable batteries on the market, is today  $200 \text{ Wh kg}^{-1}$  at the maximum. This value is not sufficient to power fully electric vehicles with a driving range of 400 km (range of the internal combustion car) which requires a battery pack of 90 kWh. To deliver such energy the weight of the battery system should be higher than 400 kg and the corresponding increase of the mass of the vehicle would narrow the practical driving range to ca. 280 km. Two main strategies are today pursued by the scientific community and automotive companies to improve the energy of the rechargeable lithium batteries up to the transportation targets. The first is the increase of the working voltage of LIBs by the use of cathode materials with high-voltage  $\text{Li}^+$  intercalation/deintercalation reactions. The second is the increase of battery capacity by the development of a new cell chemistry where oxygen redox reaction (ORR) is the process that occurs at the cathode and metal lithium is the anode. This kind of system is called lithium/air (or  $\text{Li}/\text{O}_2$ ) battery. This PhD work is focused on the development of high-voltage safe cathodes for LIBs (in the frame of the Italian national program “*Ricerca di sistema elettrico*”), and on the investigation of the feasibility of  $\text{Li}/\text{O}_2$  battery operating with ionic liquid (IL)-based electrolytes (in the frame of the European project “*Lithium-Air Batteries with split Oxygen Harvesting and Redox processes-LABOHR*”).

Chapter 1 reports the state of art in the fields of high voltage cathodes for LIBs and  $\text{Li}/\text{O}_2$  batteries operating in organic electrolytes, for application in Hybrid and full Electric Vehicles.

In Chapter 2 are reported the chemicals used, the description of the instruments used for synthesis and chemical-physical characterizations, the electrodes preparation, the batteries configuration and the electrochemical characterization procedure of electrodes.

In Chapter 3 is discussed the use of  $\text{LiMn}_{1-x}\text{Fe}_x\text{PO}_4$  ( $x = 0, 0.2, 0.3$ ) as high-voltage cathode material for LIBs. The synthesis, the characterization and the electrochemical tests of three different carbon-coated phosphates,  $\text{LiMnPO}_4$ ,  $\text{LiMn}_{0.8}\text{Fe}_{0.2}\text{PO}_4$  and

$\text{LiMn}_{0.7}\text{Fe}_{0.3}\text{PO}_4$  which are more stable and safe cathode materials than transition metal oxides are reported.

In Chapter 4 is discussed the feasibility of  $\text{Li}/\text{O}_2$  battery operating in IL-based electrolytes. Three aspects have been investigated: basic aspects of oxygen redox reaction (ORR) in different IL-based electrolytes (Section 4.1), synthesis and characterization of porous carbons as positive electrode materials for high capacity  $\text{Li}/\text{O}_2$  batteries (Section 4.2) and study of limiting factors to the electrode capacity and cell cycle life (Section 4.3).

In conclusion regarding the study of LIBs the findings on  $\text{LiMnPO}_4$  prepared by soluble precursors demonstrate that a good performing Mn-based olivine is viable, even without the coexistence of iron. Regarding  $\text{Li}/\text{O}_2$  battery, the ORR was studied from the basic point of view and oxygen diffusion coefficient ( $D_{\text{O}}$ ) and concentration ( $C_{\text{O}}$ ) values in different ILs were obtained. The stability of the selected IL, N-butyl-N-methyl pyrrolidinium bis (trifluoromethanesulfonyl) imide ( $\text{PYR}_{14}\text{TFSI}$ ), to oxygen reduced species was demonstrated, confirming the good choice of this organic melted salt as electrolyte. This PhD work highlighted that the key factor that limits the  $\text{Li}/\text{O}_2$  capacity at the high currents of interest for automotive application is the  $\text{O}_2$  mass transport. Furthermore, it gave indications on how to increase battery capacity at high discharge rate by the use of a flow-cell and a cathode constituted by a meso-macro porous carbon obtained by a simple, low-cost template synthesis.

# Table of Contents

<b>Chapter 1. Introduction</b>	p.1
1.1 High-voltage cathode material for lithium-ion batteries	p.4
1.2 Lithium/air batteries	p.7
1.2.1 Ionic liquids as electrolytes	p.11
1.2.2 Energy calculations for lithium/oxygen battery	p.13
1.3 Aim of the thesis	p.15
1.4 References	p.15
<b>Chapter 2. Experimental Section</b>	p.19
2.1 Experimental for lithium-ion battery	p.19
2.1.1 Chemicals	p.19
2.1.2 Equipments for synthesis and chemical-physical characterizations	p.20
2.1.3 Electrodes preparation, cells configuration and electrochemical characterization	p.20
2.2 Experimental for lithium-oxygen battery	p.22
2.2.1 Chemicals	p.22
2.2.1.1 Ionic Liquid environmental sustainability	p.23
2.2.2 Equipments for synthesis and chemical-physical characterizations	p.26
2.2.3 Electrodes preparation, cells configuration and electrochemical characterization	p.26
2.2.4 Lithium protective membrane	p.28
2.3 References	p.29
<b>Chapter 3. <math>\text{LiMn}_{1-x}\text{Fe}_x\text{PO}_4</math> (<math>x = 0; 0.2; 0.3</math>) as cathode materials for lithium-ion batteries</b>	p.31
3.1 Synthesis and characterization	p.31
3.2 Electrochemical test	p.34
3.3 Summary of $\text{LiMn}_{1-x}\text{Fe}_x\text{PO}_4$ ( $x = 0; 0.2; 0.3$ ) as cathode materials for lithium-ion batteries	p.38
3.4 References	p.39

<b>Chapter 4. Lithium-oxygen battery</b>	p.41
4.1 Oxygen redox reaction in ionic liquid-based electrolytes	p.41
4.1.1 ORR at GC electrodes in ILs without lithium salt	p.42
4.1.2 ORR in IL-LiTFSI solutions	p.56
4.1.3 Summary of ORR basic aspects in IL-based electrolytes	p.61
4.2 Synthesis and characterization of porous carbons as cathode materials for high capacity Li/O <sub>2</sub> batteries	p.63
4.2.1 Syntheses of novel carbon architectures by disordered template method	p.64
4.2.2 Porosity analysis of disordered template carbons	p.66
4.2.3 Electrochemical characterization of meso-macro porous ZL carbon in O <sub>2</sub> -saturated PYR <sub>14</sub> TFSI - 0.1 M LiTFSI	p.68
4.2.4 Electrochemical characterization of TMb, NZL and BZL template carbons in O <sub>2</sub> -saturated PYR <sub>14</sub> TFSI - 0.4 M LiTFSI	p.75
4.2.5 Electrochemical characterization of carbon/catalyst systems in O <sub>2</sub> -saturated PYR <sub>14</sub> TFSI – LiTFSI solutions	p.77
4.2.6 Summary of the synthesis and characterisation of meso-macro porous carbons for ORR process	p.85
4.3 Limiting factors to the electrode capacity and cell cycle life	p.85
4.3.1 Role of oxygen mass transport	p.86
4.3.2 Recharge efficiency and cathode cycle life	p.93
4.3.3 Summary of the limiting factors to the electrode capacity and cell cycle life	p.97
4.4 References	p.98
<b>Chapter 5. Conclusions</b>	p.101
<b>Acknowledgements</b>	p.103
<b>List of Presentation to Conferences</b>	p.105
<b>List of Publications</b>	p.109

# Chapter 1

## Introduction

The intense consumption of fossil fuels used for powering the increasing number of machineries results in the emission of high amount of greenhouse gases that influences the global climate change. For preserving the health of our and future generations, and because the increasing prices of fossil fuels, it is necessary to reconsider which kind of energy to adopt and how to use it, taking into account that a new energy economy should be based on a sustainable and cheap energy supply. It has been estimated that about 30% of world energy consumption is due to the transportation and it is in this field that the use of battery, as energy storage and conversion systems, can potentially provide a solution to the energetic problem, especially if they can be used to store energy from sustainable sources such as solar power and wind. One of the first electric car was produced at the beginning of XX century. It was the lack of good batteries (due to the shortage of suitable electrode materials and electrolytes) that delayed the development of electric cars compared to internal combustion vehicles [1.1]. In the past few decades the technology of lithium batteries has led to great revolutions in the context of portable electronic devices encouraging the development of large size batteries. Due to their energy density, which is higher than that of other power sources such as Ni-MH batteries, lithium-ion batteries are being considered able to satisfy the increasing automotive energy demand [1.2]. For small vehicles, with a limited drive autonomy current-day lithium battery technology may prove adequate. However, despite that about the 80 % of automotive customers use their car for covering daily distances less than 60 km the electric car market is still limited. Batteries of higher energy, higher power densities and with faster charge times than the today systems are required to effectively replace the more conventional internal combustion vehicles, providing a total electric drive autonomy of ca. 400 km [1.3]. The electric vehicles can be divided into two main classes: full Electric Vehicles (EVs) and Hybrid Electric Vehicles (HEVs). An EV uses only an electric motor for propulsion powered by a battery which operates in *charge-depleting* mode. The advantages of EVs are the high energy conversion

efficiency (c.a. 90 % compared to only 25 % of a conventional car with internal combustion engine), the possibility to convert kinetic energy back into stored electricity and the lower emission of air pollutants. The main disadvantages are the limited driving range (related to the low energy density of today batteries) and the long recharge time compared to the fast process of refueling a conventional car. Power-assist HEV is constituted by a conventional engine and an electric motor (powered by a batteries system), both used to move the car. The two motors can work both attached to the driveshaft (parallel hybrid car) or it is only the electric motor that propels the car, so the gasoline engine is used after that the battery has been depleted as a generator to power the electric motor (series hybrid car). Today most available HEVs works with the internal combustion engine that provides all the electricity for the battery (*charge-sustaining* system). It also exists a quite new class of HEVs, called *plug-in*, where the batteries can be charged from the electric grid. This class of vehicles can operate in *charge-depleting* mode and switch to *charge-sustaining* mode after the battery has reached its minimum state of charge threshold.

Table 1.1 reports some battery pack targets for EVs and *plug-in* HEVs, defined by the United States council for automotive research.

**Table 1.1:** End of life targets for battery pack for EVs and *plug-in* HEV (pHEV)

End of life characteristics	Units	EV	pHEV
Driving range	km	--	65
Maximum system weight	kg	190	120
Peak pulse discharge power (10 sec)	kW	--	38
Peak pulse discharge power (2 sec)	kW	--	46
Peak pulse specific discharge power (30 s)	W/kg	470	--
Peak regen pulse specific power (10 s)	W/kg	200	208
Useable specific energy at C/3 discharge rate	Wh/kg	235	--
Useable energy at C/3 discharge rate	kWh	45	--
Available energy for charge-depleting mode (10 kW Rate)	kWh	--	11.6
Charge-depleting mode life	Cycles	1000	5000
Charge-sustaining mode life (50 Wh profile)	Cycles	--	300000
Recharge time	Hours	< 7	--
Maximum operating voltage	V	420	420
Minimum operating Voltage	V	220	220
Calendar life	Years	15	15

Lithium-ion intercalation/deintercalation chemistry is the most advanced commercially available technology in rechargeable batteries field and it is considered to play a key role for the development of full Electric Vehicles and *plug-in* Hybrid Electric Vehicles. However, the application of this technology in the automotive field is still limited, mainly because of safety issues (lithium-ion batteries use highly energetic materials with a flammable electrolyte that, under abuse conditions, can lead to fire or explosion), high costs and low specific energy that, at the state of the art, reaches at battery pack level of  $180 \text{ Wh kg}^{-1}$  at the maximum. For a medium-size car a specific energy of 18 kWh has been estimated for a driving range of 100 km [1.4], this energy can be delivered by well-optimized state of art Li-ion battery pack featuring a weight higher than 100 kg. Considering a driving range of 400 km the Li-ion battery pack will reach a mass higher than 400 kg and, if used in a car, would significantly increase the total weight of the vehicle compromising the car efficiency and narrowing the practical driving range to c.a. 280 km [1.5]. An increase of 400 kg for a medium-size car with an average weight of 1500 kg is not a sustainable value, making unfeasible the use of Li-ion battery for a EVs with driving range comparable to those of conventional internal combustion vehicles. Moreover the 18 kWh estimated for 100 km driving range, applies only for optimal driving conditions, e.g. very moderate performance demand, no hill climbing and no motorway driving. In a realistic drive cycle the driving range is estimated to be up to 40 % shorter.

Figure 1.1 shows that the today's Li-ion systems are suitable for HEVs (that required lower total electric driving range) and that a battery with a higher specific energy is required in order to have EVs with a driving range comparable with conventional vehicles. Many research efforts have been focused to enhance the cell energy by increasing the cell capacity or voltage, according to the relation:

$$E = Q \cdot V$$

where  $E$  is the energy,  $Q$  the capacity and  $V$  the open circuit voltage of the battery.

Two main strategies, in the field of rechargeable lithium batteries technology, are today pursued by scientific community and automotive companies to improve the energy of such systems up to the transportation targets. The first is the increase of cell working voltage by the use of lithium-ion batteries that have cathode materials with high-voltage potential of  $\text{Li}^+$  intercalation/deintercalation reaction. The second strategy is the increase of

battery capacity by the development of a new cell chemistry where oxygen redox reaction (ORR) is the process that occurs at the cathode and the anode is a metal lithium. This kind of systems are called lithium/air or lithium/oxygen batteries. While some predictions show that Li-ion batteries operating with high-voltage (4.5 V) and high-capacity (275 mAh g<sup>-1</sup>) cathode may reach a final pack energy of 400 Wh kg<sup>-1</sup>, significantly higher values are needed to have a competitive EVs. Higher specific capacity values can be obtained, on the basis of theoretical calculation, with lithium/air batteries (Figure 1.1).

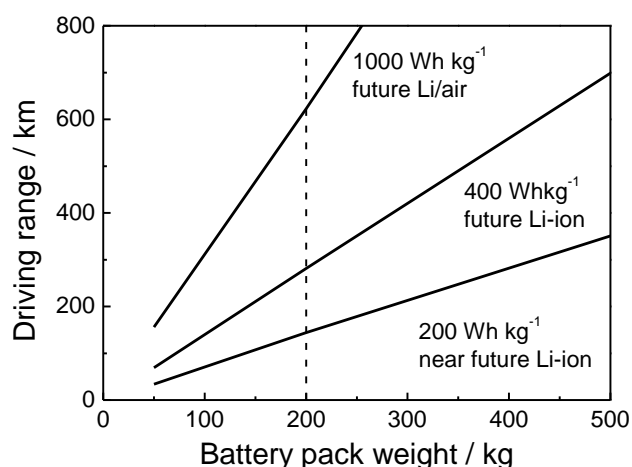


**Figure 1.1:** Driving range vs. battery pack weight for different cell types. [adapted from Ref. 1.5]

## 1.1 High-voltage cathode material for lithium-ion batteries

The working principle of Li-ion batteries (LIBs) consists in a reversible intercalation/deintercalation of lithium cations in the two coupled electrodes with simultaneous electron transfer process. While during the charge of the battery Li<sup>+</sup> ions are extracted from the positive electrode and inserted into the negative, during the discharge the reverse process takes place.

Combination of graphite (the most used anode material) with high-voltage (> 4 V vs Li<sup>+</sup>/Li) cathode plays a fundamental role for the development of high energy (≥ 200 Wh kg<sup>-1</sup>) and power rechargeable LIBs. The main problem that limits the use of high-voltage cathodes such as, for example, Nickel manganese spinel oxides (LiNi<sub>0.5-y</sub>Mn<sub>1.5-y</sub>O<sub>4</sub>) which show an average potential of 4.7 V vs Li<sup>+</sup>/Li, [1.6] is the electrochemical instability of

conventional electrolytes towards oxidation at potential higher than 4.5 V vs  $\text{Li}^+/\text{Li}$ . Usually, electrolytes for commercial LIBs comprise  $\text{LiPF}_6$  in a mixture of ethylene carbonate, important for SEI (solid electrolyte interface) formation process on graphite electrodes, with one or more linear alkyl carbonates. During the first cycles of the battery, at the low working potential of negative electrode, the electrolyte decomposes generating a SEI that acts as protective film on the electrode surface, preventing further decomposition reactions. The progress of high-voltage LIBs is strongly connected with the development of novel stable electrolytes or additives able to provide, in conventional electrolytes, a protective film also at the cathode, preventing the electrolyte oxidative degradation.

One possibility to avoid additives, which can interfere with electrode redox processes, and to work with conventional electrolytes, is to use  $\text{LiMnPO}_4$  as cathode material.  $\text{Li}^+$  intercalation/deintercalation potential of  $\text{LiMnPO}_4$  is 4.1 V vs  $\text{Li}^+/\text{Li}$ , which is 650 mV more positive than that of  $\text{LiFePO}_4$ , already used in commercial LIBs, and still within the stability window of ethylene carbonate-based electrolytes.

At the end of nineties Padhi e Goodenough [1.7] proposed the use of phosphates of transition metals ( $\text{LiMPO}_4$ ) with olivine structure (orthorhombic space group  $Pnma$ ) as cathode materials. The phosphate anion, changing the chemical environment of the metal ( $M$ ), shifts the potential of the pair  $M^{2+}/M^{3+}$  at higher values. The first phosphate proposed as cathode material was the lithium iron phosphate ( $\text{LiFePO}_4$ ) which shows a  $\text{Li}^+$  intercalation/deintercalation potential of 3.45 V vs.  $\text{Li}^+/\text{Li}$ , with a theoretical capacity of 170 mAh  $\text{g}^{-1}$ . This material can deintercalate  $\text{Li}^+$  ions with simultaneous oxidation of  $\text{Fe}^{2+}$  to  $\text{Fe}^{3+}$ ; the process is biphasic and reversible, the two phases  $\text{LiFePO}_4$  and  $\text{FePO}_4$  have the same structure so the passage of one phase in the other involves only small changes in volume (< 6%) which is a benefit for electrode cycling stability. An advantage that the phosphate shows, in comparison with other oxides such as  $\text{LiCoO}_2$  which is one of the most common cathode material in the commercial LIBs, is the strong covalent bond between phosphorus and oxygen, which stabilizes the oxygen even at high temperatures, avoiding the well-known problems of poor safety of the oxide-based battery. One disadvantage of the phosphates is the low electrical conductivity that limits their electrochemical performance. After ten years of intense research by the scientific community, carbon-coated  $\text{LiFePO}_4$  that gives excellent performance at high C-rate, reaching the theoretical capacity of 170 mAh  $\text{g}^{-1}$  is now marketed. Padhi and Goodenough

[1.7] took into account also the  $\text{LiMnPO}_4$ , a more promising material than  $\text{LiFePO}_4$ , which shows always a biphasic  $\text{Li}^+$  intercalation/deintercalation process but at the higher potential of 4.1 V vs.  $\text{Li}^+/\text{Li}$ , and which maintains a theoretical specific capacity of  $170 \text{ mAh g}^{-1}$ . The use of  $\text{LiMnPO}_4$ , instead the iron phosphate, would enable the development of a Li-ion battery with energy of approximately 20% higher. From the beginning, however, the difficulty of completely lithiate/delithiate such material because the high overpotentials was highlighted and the use of mixed compounds of the type  $\text{LiMn}_{1-x}\text{Fe}_x\text{PO}_4$  with a low amount of Mn was suggested.

Two main causes prevent the practical use of  $\text{LiMnPO}_4$  in LIBs, one is the low electronic conductivity which is about two orders of magnitude smaller compared to that of iron phosphate [1.8, 1.9] and the second is the distortion of the crystal lattice, generated at the interface between  $\text{LiMnPO}_4$  and  $\text{MnPO}_4$  during the  $\text{Li}^+$  insertion/extraction, due to the Jahn-Teller effect [1.10, 1.11]. Due to the oxidation of Mn from  $\text{Mn}^{2+}$  to  $\text{Mn}^{3+}$  the crystal structure shows variation in cell parameters sufficient to generate a mismatch between the  $\text{LiMnPO}_4$  and  $\text{MnPO}_4$  phases (see Figure 1.2). The lattice distortion produces a speed slowdown of  $\text{Li}^+$  intercalation/deintercalation process, resulting in a higher charge transfer resistance of  $\text{LiMnPO}_4$  with respect to  $\text{LiFePO}_4$ .

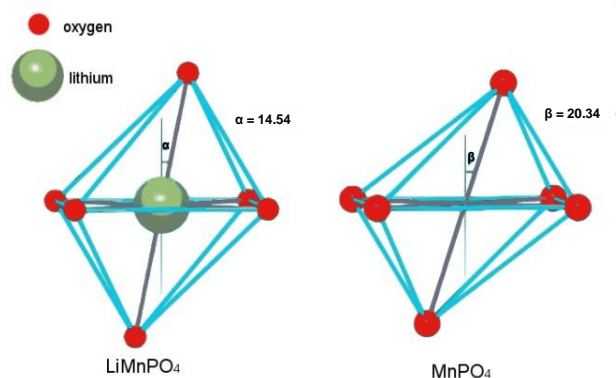


**Figure 1.2:** Scheme of interstitial octahedral site of  $\text{LiMnPO}_4$  and  $\text{MnPO}_4$  framework. [adapted from Ref. 1.10]

Given that the electrochemical performance of  $\text{LiMnPO}_4$  are, until now, significantly lower than those of  $\text{LiFePO}_4$ , further studies are required in order to practically use this material as high-voltage cathode in LIBs.

## 1.2 Lithium/air batteries

Due to their high theoretical energy density, metal-air batteries represent a promising technology for application in the automotive field. Their operation is based on the electrochemical reduction of  $O_2$  (taken directly from the air or stored inside the battery) at a high surface area positive electrode, coupled with a metallic negative electrode. Metal/air batteries can be based on different metal species and electrolytes and, thus, their reaction mechanisms are variable [1.2]. Moreover, the metal nature affects the negative electrode potential, changing the cell working voltage, and the rechargeability. Figure 1.3 compares theoretical energy densities of different metal-air battery systems and of gasoline; it is clear that only lithium-air systems can reach similar theoretical energy density of fuel. Due to the fact that the typical tank-to wheel efficiency of an internal combustion machine is less than 13%, the practical energy density of gasoline for automotive applications drops to c.a.  $1.7 \text{ kWh kg}^{-1}$ . This value is the 15% of the Li/air battery theoretical energy and it seems to be practically achievable even taking into account that the efficiency of electric propulsion system is c.a. 90% and that the commercialized metal/air batteries, such as Zn/air, show a practical energy density of about 40% of their theoretical value [1.12].

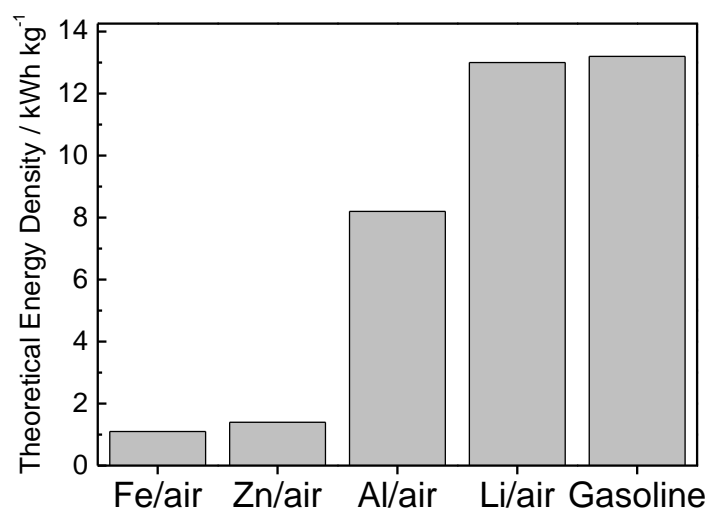


**Figure 1.3:** Comparison of theoretical energy density of different metal/air technologies and gasoline [adapted from Ref. 1.13]

The first lithium/air battery was proposed in the second half of seventies [1.14]. This type of battery worked in an aqueous alkaline electrolyte but, because of safety issues due to the high reactivity of Li with water, the project was abandoned. At the end of nineties the scientific community rediscovered a great interest for Li/air batteries thanks to Abraham and Jiang work. In the 1996 the two Authors demonstrated that using a nonaqueous electrolyte it is possible to obtain a rechargeable Li/air battery with promising performance [1.15]. The cell proposed by Abraham et al. was made by a Li metal anode, a high surface area carbon cathode and a Li conductive solid polymer electrolyte and this cell reached with a bad cyclability and a specific energy of ca.  $300 \text{ Wh kg}^{-1}$ . After this work much research efforts have been focusing on lithium-air batteries, especially on nonaqueous cell designs, to improve battery performance. Figure 1.4 reports the scheme of Li/air battery operating in organic electrolyte, where the oxygen is directly taken from the air. Often, in order to avoid any contamination by other gases like water vapour and  $\text{CO}_2$ , lab-scale tests are done with pure oxygen and not using atmospheric air, and in this case it is better to define the system as Li/oxygen battery

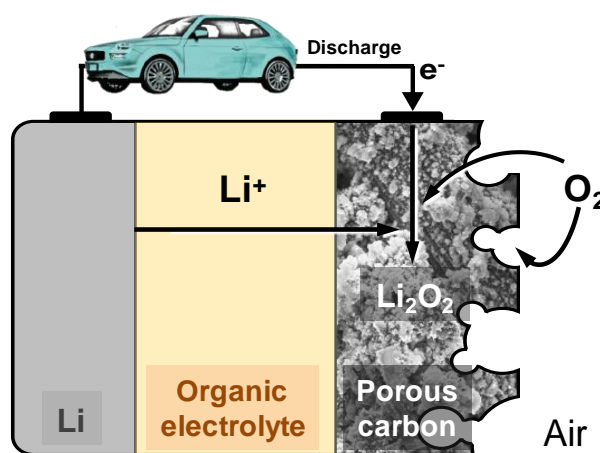


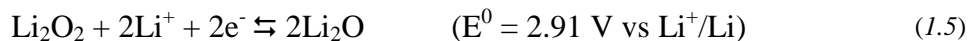
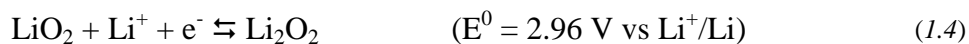
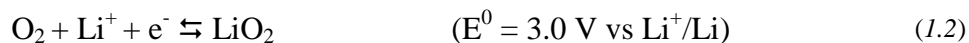
**Figure 1.4:** Schematic cell configurations of nonaqueous Li/air battery

In nonaqueous aprotic electrolyte the oxygen reduction reaction proceeds step by step from superoxide ( $\text{O}_2^{\cdot-}$ ) to peroxide ( $\text{O}_2^{2-}$ ) and, finally, to oxide ( $\text{O}^{2-}$ ) anions formation. The first step that involves the  $\text{O}_2^{\cdot-}$  production, according to equation 1.1, is a mono-electronic process [1.16-1.18].



The electrochemical reversibility of this process depends on the kind of cations present in solution as well as by the electrolyte nature. Laoire et al. reported that solvent influences the reaction kinetics, performing the ORR study in different organic electrolytes like 1,2-dimethoxyethane, tetraethylene glycol dimethyl ether, acetonitrile and dimethyl sulfoxide [1.19]. They also studied the ORR mechanism in acetonitrile with different cations like tetrabutylammonium ( $\text{TBA}^+$ ),  $\text{K}^+$ ,  $\text{Na}^+$  and  $\text{Li}^+$  [1.20]. The interpretation of the resulting data was done according to the hard soft Lewis acid base theory (HSAB), proposed by Pearson in 1963 [1.21] that defined the “hard” and “soft” properties of an acid or a base depending on its charge/radius ratio. Atoms (or molecules) with high charge and small radius were defined as “hard”, in contrast atoms with low charge and large size were defined as “soft”. The principal statement of this theory is that “*hard acids prefer to coordinate to hard bases and soft acids prefer to coordinate to soft bases*” [1.22]. Laoire and co-authors found that with tetrabutylammonium hexafluorophosphate ( $\text{TBAPF}_6$ ) salt the redox couple  $\text{O}_2/\text{O}_2^-$  appears electrochemically reversible, this is due to the formation of a complex  $\text{O}_2^- \cdot \text{TBA}^+$  with a coordination bond between superoxide anion (“soft” base) and the alkylammonium cation (“soft” acid) that stabilizes the  $\text{O}_2^-$  and prevents its further reduction to peroxide. Also the acceptor number of the solvent, that is an expression of its acidity, influences the reversibility of the process. When a solvent with a higher acceptor number is used, for example acetonitrile instead of 1,2-dimethoxyethane,  $\text{TBA}^+ \cdot \text{PF}_6^-$  bond weakens as consequence of an increase in the interaction between solvent and  $\text{PF}_6^-$ .  $\text{TBA}^+$  assumes a character of naked ion and its bond with  $\text{O}_2^-$  becomes stronger, stabilizing the superoxide anion and increasing the reversibility of  $\text{O}_2/\text{O}_2^-$  redox process.

The one-electron reduction of oxygen to superoxide becomes electrochemically irreversible when lithium salt is used instead of tetrabutylammonium salt.  $\text{Li}^+$  is a “hard” Lewis acid and has higher affinity to a “hard” bases such as peroxide or oxide. For this reason the lithium superoxide ( $\text{LiO}_2$ ) produced in the first reduction step (equation 1.2) is not enough stable and easily evolves to lithium peroxide ( $\text{Li}_2\text{O}_2$ ) by chemical disproportion or as consequence of a second mono-electronic reduction step, as described in equations 1.3 and 1.4 respectively. A further reduction at lower potential, with formation of lithium oxide ( $\text{Li}_2\text{O}$ ) is also possible (equation 1.5). Equations 1.2 - 1.5, moreover, report the theoretical potentials for each reaction calculated from the Gibbs free energies [1.23].



In a practical Li-air battery operating in nonaqueous solvent that works in presence of  $\text{Li}^+$  ions,  $\text{Li}_2\text{O}_2$  results as the main discharge product if the system operates at reduction potentials sufficiently high to avoid  $\text{Li}_2\text{O}$  formation. The lithium peroxide produced during the battery discharge, being very low soluble in organic electrolyte, clogs the pores of the cathode material reducing the total achievable capacity. Moreover, due to the fact that  $\text{Li}_2\text{O}_2$  is an electrical insulator, its presence increases the internal resistance of the cell, causing a high charge overpotential [1.13] which makes the battery recharge more difficult. However, lithium peroxide is a better discharge product than lithium oxide, not only because  $\text{Li}_2\text{O}_2$  reduction potential is higher than that of  $\text{Li}_2\text{O}$  (reflecting in a higher discharge potential of the whole battery) but also because lithium oxide has higher insulating characteristic that implies higher recharge irreversibility of the system.

The material forming the positive electrode for oxygen reduction reaction should have low density, low electrical resistance, porous structure and high surface area. The porosity of the cathode material is important to store the greatest amount of discharge products and to favour a fast oxygen diffusion (enabling higher oxygen and electrolyte transport). The electrode materials can play an important role as electro-catalysts for example acting as electron transfer enhancer or changing the electronicity of the process. Different studies have been performed on a large variety of materials, for example metal foam as nanoporous Au [1.24], polycrystalline Pt [1.4], carbon-supported transition metal systems and structured porous carbons, in order to identify the better cathode system. Low density carbonaceous materials are widely used because it is possible to easily change their structure or functionalize their surface with organic or inorganic catalysts and, hence, to obtain a large range of different materials.

To allow the use of metal lithium as anode, a protective layer (SEI) has to be formed on the top of the electrode surface. If this SEI is not spontaneously formed as a consequence of electrolyte reduction, it must be artificially prepared and thus depends on

the electrolyte nature. SEI is an electronically insulating layer that kinetically stabilizes the anode, preventing further side reactions but allowing  $\text{Li}^+$  ion diffusion.

The choice of the electrolyte is one of the key factors that must be taken into account, because its physical and chemical properties strongly influence the battery performance. An ideal electrolyte should be characterized by wide electrochemical stability window, low viscosity and volatility, high oxygen solubility and high stability toward oxygen reactive species. The carbonate-based electrolytes commonly used in Li-ion batteries were the first choice also for testing nonaqueous Li-air cells [1.15, 1.25]. These electrolyte solutions can efficiently stabilize the lithium metal surface and show low viscosity and quite good oxygen solubility. Unfortunately carbonate-based electrolytes are unstable to oxygen reduction products and decompose during battery cycling, producing lithium carbonates and other by-products. The cyclability showed by Li-air cells operating in such carbonate-based solutions was mainly affected by the irreversible decomposition of the electrolyte. The ability to achieve repeated reversible charge/discharge cycles is fundamental for a practical use of Li-air batteries. A variety of electrolytes, including ethers, dimethyl sulfoxide, ionic liquids and other organic media, are under study with a particular attention to their electrochemical and chemical stability [1.26-1.29].

### 1.2.1 Ionic liquids as electrolytes

As previously discussed in paragraph 1.2, the electrolyte is a key cell component that influences the lithium-air battery performance. Room temperature molten salts, commonly known as ionic liquids (ILs), are a large class of solvents that exhibits attractive features for applications in electrochemical devices. Low volatility, high chemical and electrochemical stability, non-flammability and good ionic conductivity are the main properties that make ILs “key electrolytes” for the development of advanced and more safe lithium secondary batteries [1.30]. Due to the molecular nature of IL cationic and anionic components, it is possible to synthesize a large variety of different salts, changing their size, chemical nature and functionality. This wide synthetic option gives the possibility to have ILs with the desired physicochemical properties, in relation to the considered application (e.g. hydrophobicity, Lewis acidity, lower viscosity etc.). The interaction of the

weak Lewis acid cation with the weak Lewis basic anion, forming the ionic liquid, is not enough strong to maintain the ionic association even at room temperature, defining ILs as “self-dissociable liquid salts” [1.31]. It is this characteristic that mainly differentiates ILs from ionic crystals (that exhibit strong ions interaction) and conventional organic solvents (that do not show charge separation). Due to their low vapour pressure ILs are low flammable solvents, considered “key electrolytes” for the development of safe electrochemical devices. The ionic nature of ILs is the reason for their low vapour pressure but it is also at the base of their high viscosity that can negatively affects the mass transport of electroactive species as oxygen and lithium ions in Li-air batteries.

For lithium/air battery applications the oxygen redox reaction in ionic liquids must be well known. In 1991 Carter et al. [1.32] proposed the first voltammetric study of  $O_2$  at a glassy carbon electrode in 1-ethyl-3-methylimidazolium chloride, mixed with  $AlCl_3$ . In the cathodic scan it was observed a single peak, related to the one-electron reduction of oxygen to superoxide anion (equation 1.1), but no peak was detected in the reverse anodic scan, underlining the irreversibility of the whole redox process in this ionic liquid. The lack of reversibility of the oxygen redox reaction in imidazolium chloride-based ionic liquids is a consequence of the reaction of superoxide with  $H^+$  impurities (“hard” acid) existing in the electrolyte. After Carter’s work, several papers were published reporting the ORR study in different ionic liquids and experimental conditions. The main derivable conclusion is that oxygen redox reaction is possible in a large variety of ILs, but the presence of impurities can have a dramatic effect on the stability of the superoxide ion, making ORR electrochemically irreversible. Generally superoxide anion is stable in ILs with aliphatic and alicyclic organic cations, such as pyrrolidinium and ammonium ions, but reacts with imidazolium aromatic based ILs which exhibit an acid proton on N-1 position. Pyrrolidinium-based cations coupled with anions like bis(trifluoromethylsulfonyl)imide (TFSI), seem to guarantee the best conditions for the electrochemical oxygen reactions, and also provide a system that can be easily functionalized [1.30, 1.33, 1.34]. Even in ILs the ORR proceed is like in organic solvent,s as previously discussed in paragraph 1.2 (equations 1.1-1.5). The  $O_2^-$  is stabilized by the “soft” IL cation in pure electrolyte, while the presence of  $Li^+$  “hard” cation makes ORR irreversible, with the formation of insoluble  $Li_2O_2$  as the main discharge product.

The literature reports different conclusions about the stability of lithium metal electrode and the formation of a good SEI which allows good cyclability of the anode, in pyrrolidinium-based ionic liquids. Howlett and co-authors reported about a low cycle life, ascribable to the poor stability of the TFSI anion in contact with metallic lithium [1.35]. However Passerini et al. demonstrated that high purity pyrrolidinium-based ionic liquids are electrochemically stable at the lithium-metal deposition potential, performing more than 1000  $\text{Li}^+$  deposition and dissolution cycles with an efficiency approaching 100% [1.36-1.38]. It is also reported that bis(fluorosulfonyl)imide (FSI) seems to be one of the best electrolyte because it is a good SEI forming [1.39], unfortunately its synthesis and purification is too difficult with some safety concerns, preventing its use on a large scale. In conclusion, ILs can offer some advantages compared to more volatile organic solvents but more studies are needed to better understand their electrochemical response both with lithium and oxygen species.

From the voltammetric point of view, ionic liquid behaviour can be quite different from those of the traditional organic solvents containing a supporting electrolyte. Usually ILs show wide electrochemical window as direct consequence of the cation and anion high stability, this characteristic can allow the observation of larger number of voltammetric process usually not detectable in the potential range of the traditional solvents. However, two major disadvantages in the use of ILs have been reported: i) the decrease of the heterogeneous electron transfer kinetic respect to conventional organic electrolyte, related to the different nature of the double layer and ii) small diffusion coefficients of the electroactive species, as consequence of the IL high viscosity (two or three order of magnitude higher than that of organic solvents). In addition literature reports that, because of their ionic nature, the diffusion coefficients of not charged (e.g.  $\text{O}_2$ ) and charged (e.g.  $\text{O}_2^{\cdot-}$ ) species can be considerably different [1.40].

### 1.2.2 Energy calculations for lithium/oxygen battery

The energy of practical lithium-oxygen battery is difficult to estimate because of the absence of standard cell designs. The major difference that influences the final achievable energy is the ability of the cell to operate directly or not with ambient air. If the use of an oxygen tank will be needed, although it is not proper a part of the battery, its

mass will be included in the calculation revealing the large disparity between the specific energy of closed (with tank) and open systems. The closed system, however, has the advantage of limiting irreversible side reactions, preventing electrolyte contamination by water or other gases. In any case, it is expected that a practical cell realizes less than half of the energy calculated on the base of the active materials alone. Christensen and co-authors proposed an estimation of lithium/oxygen battery energy [1.5] identifying  $O_2$  and Li as active materials in the charged state, and  $Li_2O$  or  $Li_2O_2$  in the discharged state (depending on which cell working reduction potential was considered). Energy calculations for a metal/air battery with a open design differ from those of LIB which is a closed system with a constant weight during its operation. The mass of Li/ $O_2$  battery, during the discharge process, increases adding the  $O_2$  contribution proportionally to the stoichiometry of the final products. Figure 1.5 shows the specific energy that the Authors calculated for practical Li/ $O_2$  cells by considering two different battery designs, one with a stainless steel oxygen tank (c.a. 20 % of the total weight of the device) and one in direct contact with the ambient air. As expected the closed systems show lower specific energy values compared to the open designs as a consequence of the additional mass of the tank and oxygen. With the models considered by Christensen and co-author a closed cell design seems to be a non convenient way to replace LIBs. However, due to the importance of increase cell cycle life limiting side reactions, different kind of oxygen harvesting devices can be proposed to make the use of a closed design feasible.

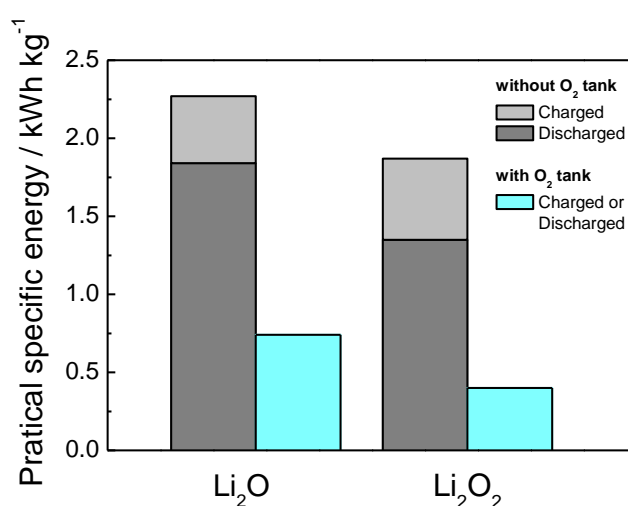


**Figure 1.5:** Practical specific energy values for selected Li-oxygen active materials without and with  $O_2$  tank. [adapted from Ref 1.5]

### 1.3 Aim of the thesis

The aim of this PhD work was the development of advanced lithium battery chemistries for application on hybrid electric vehicle and electric vehicle. This thesis is focused on: i) the development of high-voltage safe cathodes for LIBs (in the frame of the Italian national program “*Ricerca di sistema elettrico*”), ii) the investigation of the feasibility of Li/O<sub>2</sub> battery with ionic liquid-based electrolytes (in the frame of the European project “*Lithium-Air Batteries with split Oxygen Harvesting and Redox processes-LABOHR*”).

Regarding the first subject, three lithium transition metal phosphates, LiMnPO<sub>4</sub>, LiMn<sub>0.8</sub>Fe<sub>0.2</sub>PO<sub>4</sub> and LiMn<sub>0.7</sub>Fe<sub>0.3</sub>PO<sub>4</sub> which are more thermal stable and safe cathode materials than transition metal oxides were synthesized and characterized. As it concerns the second research work three main aspects have been investigated: basic aspect of oxygen redox reaction (ORR) in different ionic liquid-based electrolytes, synthesis and characterization of porous carbons for high capacity electrode materials for ORR and study of limiting factors to the O<sub>2</sub>-electrode capacity and Li/O<sub>2</sub> cell cycle life.

### 1.4 Refereces

- [1.1] M. Armand, J.M. Tarascon, *Nature*, **451** (2008) 652
- [1.2] J. Lee, S.T. Kim, R. Cao, et al, *Adv. Energy Mater.*, **1** (2011) 34
- [1.3] F.T. Wagner, B. Lakshmanan, M.F. Mathias, *J. Phys. Chem. Lett.*, **1** (2010) 2204
- [1.4] Y. Lu, H.A. Gasteiger, E.Crumlin, et al, *J. Electrochem. Soc.*, **157**-9 (2010) A1016
- [1.5] J.Christensen, P.Albertus, R.S. Sanchez-Carrera, et al, *J. Electrochem. Soc.*, **159**-2 (2012) R1 (*Original figures Copyright The Electrochemical Society*)
- [1.6] C. Arbizzani , F. De Giorgio, L. Porcarelli, et al, *J. Power Sources*, **238** (2013) 17
- [1.7] A.K. Padhi, K.S. Nanjundaswamy, J.B. Goodenough, *J. Electrochem. Soc.*, **144**-4 (1997) 1188
- [1.8] M. Yonemura, A. Yamada, Y. Takei, et al, *J. Electrochem. Soc.*, **151**-9 (2004) A1352
- [1.9] S.M. Oh, S.W. Oh, S.T. Myung, et al, *J. Alloy Compd.*, **506** (2010) 372

- [1.10] Y. Dong, L. Wang, S. Zhang, et al, *J. Power Sources*, **215** (2012) 116 (Original figure Copyright Elsevier)
- [1.11] D.Wang, H. Buqa, M. Crouzet, et al, *J. Power Sources*, **189** (2009) 624
- [1.12] G. Girishkumar, B. McCloskey, A.C. Luntz, et al, *J. Phys. Chem. Lett.*, **1** (2010) 2193
- [1.13] R.Padbury, X.Zhang, *J. Power Sources*, **196** (2011) 4436
- [1.14] A. Galbraith, “*The Lithium-Water-Air Battery for Automotive Propulsion*”, in *4<sup>th</sup> International Electric Vehicle Symposium*, Duesseldorf, West Germany (1976)
- [1.15] K.M. Abraham, Z. Jiang, *J. Electrochem. Soc.*, **143** (1996) 1 (Original figure Copyright The Electrochemical Society)
- [1.16] C.J. Allen, S. Mukerjee, E.J. Plichta, et al, *J. Phys. Chem. Lett.*, **2** (2011) 2420
- [1.17] D.T. Sawyer, G. Chiericato, C.T. Angelis, et al, *Anal. Chem.* **54** (1982) 1720
- [1.18] H. Sugimoto, S. Matsumoto, D.T. Sawyer, *Environ. Sci. Technol.*, **22** (1988) 1182
- [1.19] C.O. Laoire, S.Mukerjee, K.M. Abraham, et al, *J. Phys. Chem. C*, **114** (2010) 9178
- [1.20] C.O. Laoire, S. Mukerjee, K.M. Abraham, et al, *J. Phys. Chem. C*, **113** (2009) 20127
- [1.21] R.G. Pearson, *J. Am. Chem. Soc.*, **85**-21 (1963) 3533
- [1.22] E. Koch, *Propellants, Explosives, Pyrotechnics*, **30**-1(2005) 5
- [1.23] Y.C. Lu, H.A. Gasteiger, M.C. Parent, et al, *Electrochem. Solid State Lett.*, **13** (2010) A69
- [1.24] Y. Chen, S.A. Freunberger, Z. Peng, et al, *Nature Chem.*, **5** (2013) 489
- [1.25] T. Ogasawara, A. Débart, M. Holzapfel, et al, *J. Am. Chem. Soc.*, **128**-4 (2006) 1390
- [1.26] B.D. McCloskey, D.S. Bethune, R M. Shelby, et al, *J. Phys. Chem. Lett.*, **3** (2012) 3043
- [1.27] D. Sharon, V. Etacheri, A. Garsuch, et al, *J. Phys. Chem. Lett.*, **4** (2013) 127
- [1.28] B.D. McCloskey, D.S. Bethune, R.M. Shelby, et al, *J. Phys. Chem. Lett.*, **2** (2011) 1161
- [1.29] T. Laino, A. Curioni, *Chem. Eur. J.*, **18** (2012) 3510
- [1.30] F. De Giorgio, F. Soavi, M. Mastragostino, *Electrochem. Commun.*, **13** (2011) 1090
- [1.31] H. Tokuda, S. Tsuzuki, M.A.B.H. Susan, et al, *J. Phys. Chem. B*, **110** (2006) 19593

- [1.32] M.T. Carter, C.L. Hussey, S.K. D. Strubinger, et al, *Inorg. Chem.*, **30** (1991) 1149
- [1.33] I.M. AlNashef, M.L. Leonard, M.C. Kittle, et al, *Electrochem. Solid St*, **4** (2001) D16
- [1.34] Y. Katayama, H. Onodera, M. Yamagata, et al, *J. Electrochem. Soc.*, **151** (2004) A59
- [1.35] P.C. Howlett, E.I. Izgorodina, M. Forsyth, et al, *Z. Phys. Chem.*, **220** (2006) 1483
- [1.36] S. Randstroem, G.B. Appetecchi, C. Lagergren, et al, *Electrochim. Acta*, **53** (2007) 1837
- [1.37] S. Randstroem, M. Montanino, G.B. Appetecchi, et al, *Electrochim. Acta*, **53** (2008) 6397
- [1.38] G. Kim, G.B. Appetecchi, M. Montanino, et al, *ECS Transactions*, **25** (2010) 127
- [1.39] M. Ishikawa, T. Sugimoto, M. Kikuta, et al, *J. Power Sources*, **162** (2006) 658
- [1.40] L.E. Barrosse-Antle, A. M. Bond, R. G. Compton, et al, *Chem. Asian J.*, **5** (2010) 202



# Chapter 2

## Experimental Section

The following paragraphs report materials and methods used for lithium-ion battery (LIB) and lithium-oxygen battery studies. For a better clarity, the experimental for the two different investigated lithium-based battery systems are separately reported in Section 2.1 and 2.2 respectively.

### 2.1 Experimental for lithium-ion battery

#### 2.1.1 Chemicals

The carbon-coated  $\text{LiMnPO}_4$ ,  $\text{LiMn}_{0.8}\text{Fe}_{0.2}\text{PO}_4$  and  $\text{LiMn}_{0.7}\text{Fe}_{0.3}\text{PO}_4$ , used as cathode materials, were prepared via two sol-gel methods from partially water soluble precursors (method *I*) or totally soluble precursors (method *II*). Carbon-coated  $\text{LiMn}_{0.8}\text{Fe}_{0.2}\text{PO}_4$  and  $\text{LiMn}_{0.7}\text{Fe}_{0.3}\text{PO}_4$  were prepared according to the method *I* while carbon-coated  $\text{LiMnPO}_4$  was synthesized following both the methods and the materials are named MF8020(I), MF7030(I), M100(I) and M100(II) respectively. The chemicals employed in the syntheses of the mixed olivines are reported in Table 2.1. All the reagents were used as received.

**Table 2.1:** Precursors used for the synthesis of carbon-coated  $\text{LiMn}_{1-x}\text{Fe}_x\text{PO}_4$  ( $x = 0; 0.2; 0.3$ )

Precursor	Supplier	Sol-gel synthesis
Manganese carbonate - $\text{MnCO}_3$	Sigma Aldrich	method <i>I</i>
Manganese (II) acetate tetrahydrate - $\text{Mn}(\text{CH}_3\text{COO})_2 \cdot 4\text{H}_2\text{O}$	Sigma Aldrich	method <i>II</i>
Iron oxalate dehydrate - $\text{FeC}_2\text{O}_4 \cdot 2\text{H}_2\text{O}$	Sigma Aldrich	method <i>I</i>
Phosphoric acid - $\text{H}_3\text{PO}_4$	Sigma Aldrich	methods <i>I</i> and <i>II</i>
Lithium phosphate - $\text{Li}_3\text{PO}_4$	Sigma Aldrich	method <i>I</i>
Lithium hydroxide monohydrate - $\text{LiOH} \cdot \text{H}_2\text{O}$	Fluka	method <i>II</i>
Citric acid monohydrate - $\text{C}_6\text{H}_8\text{O}_7 \cdot \text{H}_2\text{O}$	Fluka	methods <i>I</i> and <i>II</i>

Electrodes were prepared using slurries made with the active material and polyvinylidene fluoride (PVDF, Kynar HSV 900) as binder, carbon SuperP (Erachem) as conductive additive and N-methyl-2-pyrrolidone (NMP, Fluka, purity grade >99%) as solvent. Lithium metal discs (Sigma Aldrich, 0.38 mm thick) were used as anode and reference electrodes. Electrochemical tests were done in ethylene carbonate (EC): dimethylcarbonate (DMC) 1:1-1 M LiPF<sub>6</sub> (Merck LP30) as electrolyte.

### 2.1.2 Equipments for synthesis and chemical-physical characterizations

Pyrolyses of the dry gels were done in a tube furnace (Carbolite) with a quartz tubular chamber. The synthesized powders were grounded by a planetary miller (Pulverisette 6 Fritsch) in a tungsten carbide jar.

The powder X-ray diffraction analyses (XRD) were performed by a Philips X'pert diffractometer, a Cu K<sub>α</sub> ( $\lambda=1.5406 \text{ \AA}$ ) radiation source and Ni filter with continuous acquisition in 10-80° 2 $\theta$  range, 0.05 °2 $\theta$  s<sup>-1</sup> scan rate. Sherrer's analysis of the olivine 020 diffraction peak was used to evaluate the crystallite size.

The thermo-gravimetric analyses (TGA) were carried out with a TA Q50 balance from room temperature (RT) to 700 °C (heating rate of 10 °C min<sup>-1</sup>) in O<sub>2</sub> flow.

The scanning electron microscopy (SEM) images were acquired with a ZEISS EVO 50 apparatus while high resolution transmission electron microscopy (HRTEM) images were obtained by a JEOL-JEM 2010 microscope equipped with a X-EDS analysis system.

### 2.1.3 Electrodes preparation, cells configuration and electrochemical characterization

The composite electrodes used for the electrochemical tests were prepared by lamination technique. For each sample a slurry in NMP with 85 wt.% of synthesized materials, 10 wt.% of conductive carbon SuperP, and 5 wt.% of PVDF binder was prepared using an IKA Ultra-Turrax Tube Dispenser. The slurries were laminated onto aluminum foil current collector, with a mini coating machine (MC 20, Hohsen Corp.) and dried at 120 °C for two hours. For a better adhesion of the composite to the current collector, the

aluminum sheets were previously etched by immersion in a 5% wt. KOH solution for one minute, subsequent washing and drying at 60 °C. Circular electrodes (0.64 cm<sup>2</sup>) were cut from the foil, pressed at 3000 psi (ICL-12, Ton EZ-Press) and dried at 150 °C under dynamic vacuum overnight in a glass oven (Büchi B-580). The composite mass loading per geometric area for all the tested electrodes was in the range of 3-8 mg cm<sup>-2</sup>.

Three-electrode “Swagelok-type” electrochemical cells (see Figure 2.1) with Li reference electrode were used for cathode characterization with excess of Li at the anode.

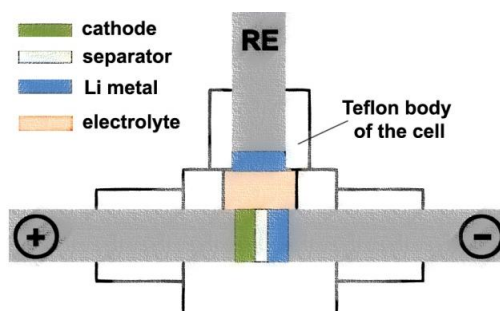


**Figure 2.1:** Schematic representation of a “Swagelok-type” electrochemical cell

A dried and degassed fiber glass separator (Whatman GF/D 400  $\mu\text{m}$  thick) was used between cathode and anode electrodes, after soaking in EC:DMC 1:1 - 1 M LiPF<sub>6</sub> electrolyte. Cell assembly and sealing, as well as lithium metal counter and reference electrodes (0.64 cm<sup>2</sup>) preparation were done in an argon atmosphere dry box (MBraun Labmaster 130, H<sub>2</sub>O and O<sub>2</sub> levels < 1 ppm) and the electrochemical tests were performed by Perkin-Elmer VMP multichannel potentiostat. The electrochemical characterization was done by discharge and charge capability tests. The general protocol for the discharge capability tests consisted in galvanostatic (CC)-potentiostatic (CV) charge and CC discharge cycles. The electrodes were charged in CC at 0.1C up to a defined potential cut-off value, followed by CV with current cut off at 0.05C; the cells were then discharged at different C-rates from 0.1C to 2C down to a defined voltage. The voltage charge cut-off and discharge cut-down values were 4.4 V and 2.3 V for material from synthesis I and 4.6 V and 2.5 V for M100(II). For M100(II) was also evaluated the charge capacity by CC charge up to 4.6 V at various C-rates from 0.1C to 2C and CC discharge at 0.1C down to 2.5 V. C-rates were determined on the basis of the theoretical specific capacity of the

active materials ( $170 \text{ mAh g}^{-1}$ ) and the electrode coulombic efficiencies, for a defined cycle, were calculated as the ratio of the discharge and charge capacities. The reported potentials were referred to  $\text{Li}^+/\text{Li}$  and the specific capacity data to the mass of the active material (excluding carbon-coating) in the electrode.

## 2.2 Experimental for lithium-oxygen battery

### 2.2.1 Chemicals

The oxygen redox reaction and the  $\text{Li-O}_2$  cell performance were studied using different pyrrolidinium-based ionic liquids (ILs) as electrolytes (see Figure 2.2): N-butyl-N-methyl pyrrolidinium bis (trifluoromethanesulfonyl) imide ( $\text{PYR}_{14}\text{TFSI}$ ), N-methoxyethyl-N-methylpyrrolidinium bis (trifluoromethanesulfonyl) imide ( $\text{PYR}_{1(201)}\text{TFSI}$ ), N-butyl-N-methyl pyrrolidinium bis (fluorosulfonyl) imide ( $\text{PYR}_{14}\text{FSI}$ ), N-butyl-N-methyl pyrrolidinium (trifluoromethanesulfonyl) (nonafluorobutylsulfonyl) imide ( $\text{PYR}_{14}\text{IM}_{14}$ ) and N-butyl-N-methyl pyrrolidinium bis (pentafluoroethanesulfonyl) imide ( $\text{PYR}_{14}\text{BETI}$ ).

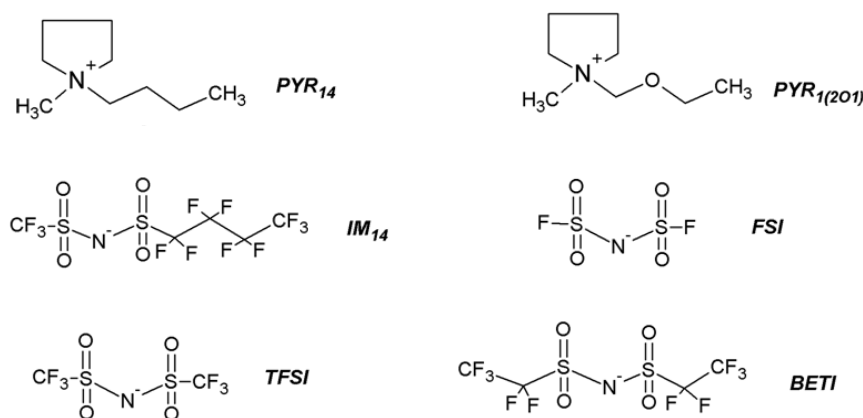


**Figure 2.2:** Structures of the ILs ions

All the used ultrapure ILs were synthesized by the group of Prof. Stefano Passerini (MEET Institute, Münster University - Germany) [2.1] in the frame of the European project

LABOHR (FP7-2010-GC-ELECTROCHEMICALSTORAGE, contract no. 265971).  $\text{PYR}_{14}\text{TFSI}$  was also purchased from Solvionic (purity 99.5%). ORR was investigated in pure ILs as well as in solutions with lithium bis (trifluoromethanesulfonyl) imide ( $\text{LiTFSI}$ ;  $3\text{M}^{\text{TM}}$ ) which was the most appropriate salt for lithium-air batteries because of the good conductivity and high electrochemical stability of its solutions. Table 2.2 lists some properties of the investigated ILs. Along this IL series, the formula weight increases while the density is almost constant, resulting in the molar concentration lowering from  $3.4 \text{ mol L}^{-1}$  of  $\text{PYR}_{14}\text{TFSI}$  down to  $2.8 \text{ mol L}^{-1}$  of  $\text{PYR}_{14}\text{BETI}$  and  $2.6 \text{ mol L}^{-1}$  of  $\text{PYR}_{14}\text{IM}_{14}$ .

**Table 2.2:** Formula weight, melting point, water content and density at 30 °C (d) of the investigated ILs.

IL	FW $\text{g mol}^{-1}$	m.p. $^{\circ}\text{C}$	$\text{H}_2\text{O}$ ppm	d $\text{g cm}^{-3}$
$\text{PYR}_{14}\text{FSI}$	322	-18	n.d.	1.31
$\text{PYR}_{14}\text{TFSI}$	422	-6.5	< 1	1.43
$\text{PYR}_{1(201)}\text{TFSI}$	424	n.d.	< 3	1.46
$\text{PYR}_{14}\text{BETI}$	522	8.9	< 1	1.48
$\text{PYR}_{14}\text{IM}_{14}$	572	n.d.	< 1	1.51

A variety of disordered porous carbons were prepared following a template method, using a formaldehyde (> 37% Fluka) - resorcinol (puriss. p.a. Riedel-de-Haën) resin as a carbon precursor and commercial colloidal silica (40%  $\text{SiO}_2$ , 70-100 nm, SNOWTEX ZL, NISSAN CHEMICAL INDUSTRIES ,Ltd.) as template (see Chapter 4, Section 4.2.1 for the synthetic procedure).

### 2.2.1.1 Ionic Liquid environmental sustainability

Some of the ionic liquids used in this PhD are commercially available, thus safety data can be easily obtained by the data sheet of the producer. Table 2.2.1 summarized, as example, the data sheet reported by Sigma-Aldrich for  $\text{PYR}_{14}\text{TFSI}$  (CAS Number 223437-11-4):

**Table 2.2.1:** Safety data for PYR<sub>14</sub>TFSI.

<b>Classification according to Regulation (EC) No 1272/2008 [EU-GHS/CLP]</b>
Skin irritation (Category 2)
Eye irritation (Category 2)
Specific target organ toxicity - single exposure (Category 3)
<b>Precautionary statements</b>
P261 Avoid breathing dust/ fume/ gas/ mist/ vapors/ spray.
P305 + P351 + P338 IF IN EYES: Rinse cautiously with water for several minutes.
Remove contact lenses, if present and easy to do. Continue rinsing

The major advantage in the use of ionic liquids in terms of environmental sustainability is correlated to their low vapour pressure and flammability. This characteristics avoid any risk of polluting emissions to air during processing and battery operation.

The ILs toxicity is mainly related to the nature of the cation [2.2-2.5], and increases from ammonium to tetrazolium as follow [2.6]:



The pyrrolidinium-based IL used in this PhD work belong to the class of ammonium salts, with low toxicity compared to aromatic cations. In addition to the aromatic nature of the cation, also the increase of the alkyl chain length substituent have a negative influence as a result of an increase of the IL lipophilicity [2.6]. The mechanism proposed is the incorporation of the long alkyl chain within the cell membranes which induces membrane expansion or swelling, lowering the phase transition temperature and change the ion permeability of the membranes [2.7]. The addition of an ether function on the alkyl chain substituent drastically reduces the toxicity of the ionic liquids. Thus, the use of the PYR<sub>1(201)</sub><sup>+</sup> cation seems more sustainable from an environmental point of view than PYR<sub>14</sub><sup>+</sup>. Also the anion has an effect on the IL toxicity, not only has result of TFSI intrinsic toxicity, but also because it can enhance the cation transport inside the cell membrane in the case of lipophilic ILs [2.7]. Literature reports a method based on the bacterium *Vibrio fischeri* for the evaluation of the ecotoxicity of ionic liquids. According to this study, the experimental ecotoxicity (log EC50, expressed on a molar basis) of

PYR<sub>14</sub>TFSI is 2.54, to be compared with the values of 2.33, 5.77 and 7.00 for toluene, acetonitrile and methanol, respectively [2.8].

If pyrrolidinium cations are less toxic as compared to imidazolium, their high electrochemical and chemical stability results in very low biodegradability and risk of accumulation in the environment, especially coupled with TFSI<sup>-</sup> anion [2.9]. It is clear that a widespread use of very stable ionic liquids, needed for battery application operating within the 0-4 V vs Li<sup>+</sup>/Li range, should be accompanied with a good recycling policy.

Ionic liquids are more thermally stable and more difficult to ignite and burn than conventional organic electrolytes. Literature reports that PYR<sub>14</sub>TFSI is thermally stable over 350 °C even under oxygen atmosphere, i.e. up to temperature more than 100 °C higher than those for the conventional organic electrolyte as EC:DMC 1:1-1 M LiPF<sub>6</sub> [2.10]. While ionic liquids are often classified as non-flammable materials, a more appropriate description would be non-volatile (up to the decomposition temperature) class IIIB combustible materials (flashpoints above 200 °C). The thermal and inflammation properties of mixtures based on EC:DMC 1:1-1 M LiPF<sub>6</sub> and PYR<sub>14</sub>TFSI have also been investigated [2.10]. These mixtures appeared less volatile than the pure organic electrolyte. The mixtures containing PYR<sub>14</sub>TFSI ignite because of the presence of the organic solvent and feature self-extinguishing times proportional to the amount of IL, which acts as a retardant rather than a flame-inhibitor. Mixtures with high amounts of ionic liquids are more difficult to ignite, but burn for a longer time once they are ignited. Hence, benefit in terms of safety is more guaranteed by the use of solvent-free ionic liquids.

Usually, conventional electrolytes used in Li-ion battery are not recyclable due to their high volatility and their degradation during cell operation. The sustainability of the used IL greatly depends on their easy recycling. Electrolyte recovery is feasible and economically convenient because PYR<sub>14</sub>-based IL containing LiTFSI are very stable and it is possible to separate the ionic liquid from the lithium salt for recycling purposes. A simple washing of the electrolyte with water allows to extract the water soluble compounds formed during battery operation and LiTFSI and obtain a rather pure IL. Then the lithium salt could be easily recycled using an aprotic solvent where LiTFSI shows high solubility contrary to most of inorganic salts.

### 2.2.2 Equipments for synthesis and chemical-physical characterizations

The formaldehyde-resorcinol resin, used for the synthesis of meso-macro disordered porous carbons, was carbonized in tube furnace (ELITE) with a quartz tubular chamber.

TGA were carried out with a TA Q50 balance from room temperature (RT) to 900 °C (heating rate of 10 °C min<sup>-1</sup>) in O<sub>2</sub> flow.

Porosimeter ASAP 2020 (Micromeritics) was used to evaluate the carbons porosity by analyzing the obtained isothermal curves by Brunauer, Emmett and Teller (B.E.T.) and Density Functional (DFT) Theories.

Scanning electron microscopy observations (SEM) and energy dispersion spectroscopy (EDS) were carried out with a ZEISS EVO 50 apparatus equipped with an energy dispersive X-ray analyzer system (Oxford model INCA ENERGY350).

XRD were performed by a Philips X'Pert diffractometer, a Cu K<sub>α</sub> (λ=1.5406 Å) radiation source and Ni filter by continuous (0.05 °2θ s<sup>-1</sup> scan rate) or step scanning (0.005 °2θ s<sup>-1</sup> scan rate) mode; Sherrer's analysis of the main diffraction peak of carbon was used to evaluate the crystallite size. A thin polymer film (Mylar) was used to protected cycled electrodes from during XRD analyses.

Raman spectra were recorded by a Raman Microscope RENISHAW Mod. INVIA with Argon ion laser (λ=514 nm, 4 scans, 10 s per scan, 1.4 cm<sup>-1</sup> resolution).

### 2.2.3 Electrodes preparation, cells configuration and electrochemical characterization

The basic aspect of the oxygen redox reaction was investigated in different ILs by cyclic voltammetry (CV), rotating disk electrode (RDE), and chronoamperometric potential step measurements (CA). The study was performed with different glassy carbon electrodes (GC, Tokai Carbon Ltd., 3 mm diameter for CV; Radiometer Analytical GC, 5 mm diameter for RDE; PAR GO226 UGC ultramicroelectrode, 10.8 μm diameter for potential steps) in a 5 mL cell which was thermostated at 30 °C and 60 °C by a HAAKE K40 thermocryostat (see Figure 2.3a). The experiments with ultramicroelectrode were

performed with the cell placed in a Faraday cage (NS-FAR600) which was ground to the potentiostat and to the water pipes of the thermocryostat. The determination of UGC diameter was done by calibration in 1 mM hydroxymethyl ferrocene (FcMeOH) - 0.1 M tetraethylammonium tetrafluoroborate - acetonitrile solution, considering a FcMeOH diffusion coefficient of  $2.5 \cdot 10^{-5} \text{ cm}^2 \text{ s}^{-1}$  at room temperature. Before each electrochemical test, the RDE and GC working electrodes were polished with 0.25  $\mu\text{m}$  diamond paste on a Selvylt cloth; for the UGC, 0.05  $\mu\text{m}$  alumina powder was used. For the RDE and GC studies a three electrodes set up was chosen with Pt wire used as counter electrode while two electrodes mode was preferred for UGC tests, using reference electrode also as counter one. Oxygen (>99.999%, SIAD) was bubbled through the cell for at least 30 min before measurements and for 30 s between consecutive runs. The CA curves recorded with UGC were collected by sampling current variations higher than 0.01 nA at least every 0.2 ms.

ORR on meso-macro porous ZL carbon was studied by CV and galvanostatic measurements (GLV) at carbon coated glassy carbon (GC, Tokai Carbon Ltd., 0.28  $\text{cm}^2$  coating area), rotating glassy carbon disk (RGC, Radiometer Analytical, 0.196  $\text{cm}^2$  coating area) or carbon paper (CP, Spectracarb 2050, Spectracorp, 0.35  $\text{cm}^2$  coating area) electrodes, at 30 °C and 60 °C in the same cell previously described and schematized in Figure 2.3a. Carbon coating on the electrodes were done by evaporation at 60 °C for several hours of aliquots of an ink comprising ZL carbon (28  $\text{mg mL}^{-1}$ ), PVDF KYNAR HSV900 (1.4  $\text{mg mL}^{-1}$ ) and NMP (Fluka, >99.0%) that was sonicated before use.

A Pt counter electrode was used for the CVs and a lithium foil for the galvanostatic measurements. The electrolyte was  $\text{PYR}_{14}\text{TFSI}$  (Solvionic, 99.5%) with LiTFSI 0.1 M or 0.4 M (i.e. IL:Li molar ratio 9:1);  $\text{PYR}_{14}\text{TFSI}$  was dried under dynamic vacuum at 80 °C overnight in a glass oven (Büchi B-580) before use, LiTFSI was stored in dry box (MBraun Labmaster 130,  $\text{H}_2\text{O}$  and  $\text{O}_2$  levels < 1 ppm) and used as received. Oxygen (>99.999%, SIAD) was bubbled through the cell for at least 30 min before the CVs and was continuously flowed for the galvanostatic discharge and interrupted under charge.

ORR was also investigated in a flow-cell (see Figure 2.3b) with ZL-coated carbon paper electrodes (CP, Spectracarb 2050, Spectracorp, 0.64  $\text{cm}^2$  coating area). The electrolyte used for the flow-cell was  $\text{PYR}_{14}\text{TFSI}$  (99.5%, Solvionic):LiTFSI 9:1. Circulation of the electrolyte through the cell was obtained by a peristaltic pump (Watson-Marlow 120S/DV) operating at 200 rpm.

The electrochemical measurements were performed with a PerkinElmer VSP multichannel potentiostat/galvanostat. A Radiometer Analytical apparatus with electrode rotation set by a CTV101 speed control unit was used for RDE tests. The cyclic voltammetric scans were corrected for the ohmic drop evaluated by impedance spectroscopy in the 10 kHz - 1 Hz range. For all the experiments was used a silver wire in  $6 \cdot 10^{-2}$  M AgTFSI (97%, Aldrich) - PYR<sub>14</sub>TFSI as reference electrode [2.11], the potential was checked vs. lithium and the working potentials are reported vs. the Li<sup>+</sup>/Li couple.

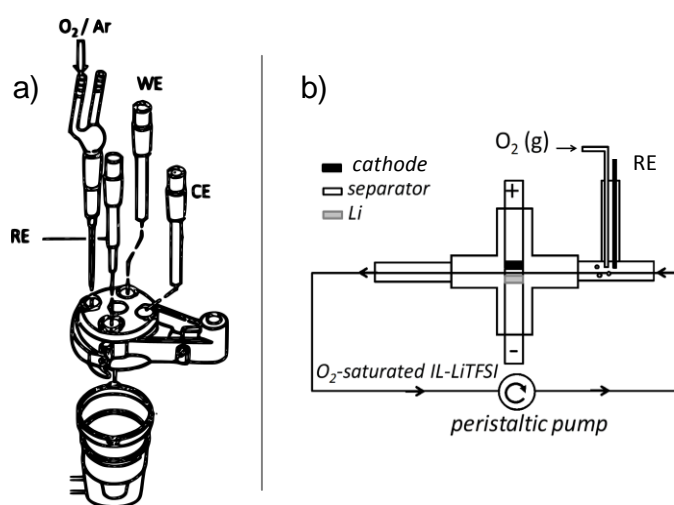


**Figure 2.3:** Scheme of the used three electrodes cell a) and flow-cell b)

## 2.2.4 Lithium protective membrane

A ternary Poly(ethylene oxide) (PEO)-based solid electrolyte, feasible protective membrane of Li in the flow-cell, was prepared in a very low relative humidity dry room (relative humidity < 0.1% at 20 °C) at the MEET Institute (Münster – Germany) by hot-pressing procedure according to [2.12, 2.13]. The ternary system was composed by PEO:LiTFSI:PYR<sub>14</sub>TFSI (10:1:4 molar ratio), at which 0.1 molar ratio of benzophenone (BP, Sigma Aldrich) was added as photo-initiator of the cross-linking process. LiTFSI and PYR<sub>14</sub>TFSI were dried before use under high vacuum ( $10^{-7}$  mbar) at 120 °C for 36 h and PEO (Dow Chemical, WSR 301, molecular weight =  $4 \cdot 10^6$ ) was dried at 50 °C under vacuum for 48 h. BP and PEO were gently mixed in an agate mortar and transferred in a

beaker, adding LiTFSI, the blend was further mixed to obtain Li<sup>+</sup> cations coordination by PEO, revealed by flake-like aspect of the system. As final step PYR<sub>14</sub>TFSI was added. The system was stored in a vacuum sealed pouch bag and annealed under vacuum at 100 °C overnight to produce a homogeneous rubber-like material. In order to have a ca. 80 μm thick layer, the annealed material pressed at 100 °C between two Mylar foils (pressure ramp: three 2 minutes steps at 10 bar, 14 bar and 18 bar). The ternary solid polymer electrolyte membrane was cross-linked using a UV Cube photo-irradiator (350WHg lamp) for 10 minutes and then housed in a sealed pouch bag.

## 2.3 References

- [2.1] G.B. Appetecchi, S. Scaccia, C. Tizzani, et al, *J. Electrochem. Soc.*, **153** (2006) A1685
- [2.2] J. Pernak, J. Kalewska, H. Ksycinska, et al, *J. Med. Chem.*, **36** (2001) 899
- [2.3] J. Ranke, K. Molter, F. Stock, et al, *Ecotoxicol. Environ. Saf.*, **58** (2004) 396
- [2.4] K.M. Docherty, C.F. Kulpa Jr., *Green Chem.*, **7** (2005) 185
- [2.5] R.P. Swatloski, J.D. Holbrey, S.B. Memon, et al, *Chem. Commun.*, (2004) 668
- [2.6] D.J. Couling, R. D. Bernot, K.M. Docherty, et al, *Green Chem.*, **8** (2006) 82
- [2.7] S.Stolte, M.Matzke, J.Arning, et al, *Green Chem.*, **9** (2007) 1170
- [2.8] M. Alvarzez-Guerra, A. Irabien, *Green Chem.*, **13** (2011) 1507
- [2.9] S. Stolte, S. Steudte, O. Areitioaurtena, et al, *Chemosphere*, **89** (2012) 1135
- [2.10] C. Arbizzani, G. Gabrielli, M. Mastragostino, *J. Power Sources*, **196** (2011) 4801
- [2.11] G.A. Snook, A.S. Best, A.G. Pandolfo, et al, *Electrochem. Commun.*, **8** (2006) 1405
- [2.12] G.T. Kima, G.B. Appetecchia, M. Carewska, et al, *J. Power Sources*, **195** (2010) 6130
- [2.13] M. Wetjen, G. Kim, M. Joost et al, *J. Power Sources*, **246** (2014) 846



# Chapter 3

## LiMn<sub>1-x</sub>Fe<sub>x</sub>PO<sub>4</sub> (x = 0; 0.2; 0.3) as cathode materials for lithium-ion batteries

As previously discussed in Chapter 1, a good strategy to increase the energy of actual lithium-ion batteries is the use of a phosphate with general formula LiMn<sub>1-x</sub>Fe<sub>x</sub>PO<sub>4</sub> ( $0 \leq x < 0.3$ ) as cathode material, mainly for safety issues. In the frame of Italian national program “*Ricerca di sistema elettrico*”, promoted by Ministero dello Sviluppo Economico and ENEA (Agenzia Nazionale per le Nuove Tecnologie, l’Energia e lo Sviluppo Economico Sostenibile) this strategy was pursued and in this PhD work three different carbon-coated phosphates, LiMnPO<sub>4</sub>, LiMn<sub>0.8</sub>Fe<sub>0.2</sub>PO<sub>4</sub> and LiMn<sub>0.7</sub>Fe<sub>0.3</sub>PO<sub>4</sub> were synthesized and characterized. The results of this study are reported in the following sections and have been published in Ref. [3.1].

### 3.1 Synthesis and characterization

Two different sol-gel methods were performed to obtain the desired products. Method *I* involved the use of partially water soluble precursors while in method *II* were used totally soluble precursors for a better dispersion. Carbon-coated LiMn<sub>0.8</sub>Fe<sub>0.2</sub>PO<sub>4</sub> and LiMn<sub>0.7</sub>Fe<sub>0.3</sub>PO<sub>4</sub> were prepared according to sol-gel method *I* and indicated MF8020(I) and MF7030(I), whereas LiMnPO<sub>4</sub> was prepared by the two methods and the synthesized materials were named M100(I) and M100(II). Table 3.1 reports the precursors used in each synthesis.

**Table 3.1:** List of the reagents used in sol-gel methods I and II for M100, MF8020 and MF7030 synthesis

Product code	Reagents
M100(I)	MnCO <sub>3</sub> , H <sub>3</sub> PO <sub>4</sub> , Li <sub>3</sub> PO <sub>4</sub> and C <sub>6</sub> H <sub>8</sub> O <sub>7</sub> ·H <sub>2</sub> O
M100(II)	Mn(CH <sub>3</sub> COO) <sub>2</sub> ·4H <sub>2</sub> O, LiOH·H <sub>2</sub> O, H <sub>3</sub> PO <sub>4</sub> and C <sub>6</sub> H <sub>8</sub> O <sub>7</sub> ·H <sub>2</sub> O
MF8020(I) and MF7030(I)	MnCO <sub>3</sub> , Fe(C <sub>2</sub> O <sub>4</sub> )·2H <sub>2</sub> O, H <sub>3</sub> PO <sub>4</sub> , Li <sub>3</sub> PO <sub>4</sub> and C <sub>6</sub> H <sub>8</sub> O <sub>7</sub> ·H <sub>2</sub> O

In both sol-gel method *I* and *II* all the precursors were added to water in stoichiometric molar ratio with the exclusion of citric acid monohydrate which was in double concentration for synthesis of M100(II). Citric acid was used as cation chelating agent and carbon source for the coating of phosphate particles. The aqueous batches were heated at 100 °C to obtain a dry gels as consequence of water evaporation. The so obtained dry systems were manually grounded in an agate mortar with a pestle and subsequently pyrolyzed under argon flow (200 ml min<sup>-1</sup>) for 1 h at 700 °C (20 °C min<sup>-1</sup>). The resulting black powders were further grounded by wet ball milling using water or acetone in tungsten carbide jar (20 WC balls of 10mm diameter) at 300 rpm for 6 h. For all the obtained products were performed XRD, SEM and TGA characterizations.

Figure 3.1 shows the X-ray patterns of the four synthesized phosphates compared with that of tabulated LiMnPO<sub>4</sub> (ICDD diffraction pattern 00-044-0073). All the main peaks are related to the expected products, demonstrating the efficacy of the sol-gel methods. The only exception is the small peak at 40.6 °2θ visible in the M100(II) pattern due to manganese oxide impurity in the product. The crystallite size of M100(I), MF8020(I) and MF7030(I), synthesized from partially soluble precursors, ranged from 34 to 43 nm, while the use of totally soluble precursors provided LiMnPO<sub>4</sub> crystallite size of 28 nm. The smaller crystallite dimensions of M100(II) might positively affect its electrochemical performance.

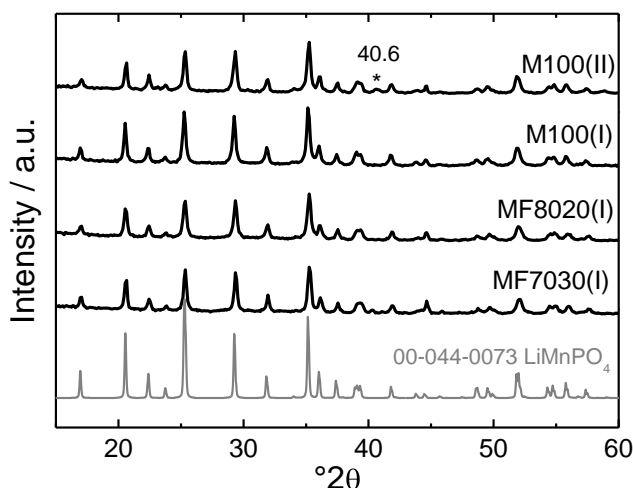


**Figure 3.1:** XRD patterns of all synthesized phosphates compared with that of LiMnPO<sub>4</sub> (ICDD diffraction pattern 00-044-0073) [adapted from Ref. 3.1].

The amount of carbon coating of each powder was evaluated by TGA, heating the samples in O<sub>2</sub> atmosphere from room temperature up to 700 °C. The oxygen burns off the carbon leaving different products depending on the presence or not of iron in the sample. Only LiMnPO<sub>4</sub> is obtained from the carbon coated M100 powders whereas LiMnPO<sub>4</sub>, Li<sub>3</sub>Fe<sub>2</sub>(PO<sub>4</sub>)<sub>3</sub> and Fe<sub>2</sub>O<sub>3</sub> are produced after heat treatment of MF8020 and MF7030 samples [3.2]. The phosphates showed the following carbon content: 14 wt.% for M100(II), 6 wt.% for M100(I), 9 wt.% for MF7030(I) and 11 wt.% for MF8020(I).

The carbon coating on the particles was confirmed by HRTEM analysis. Figure 3.2 shows, as an example, an image recorded for M100(II) powder with two areas analyzed with X-EDS which proves the presence of carbon layer on the LiMnPO<sub>4</sub> grains.

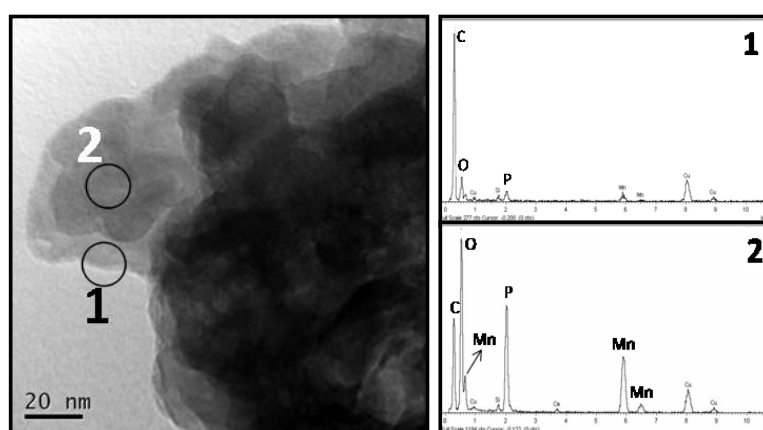


**Figure 3.2:** HRTEM image and X-EDS analysis of M100(II) [adapted from Ref. 3.1].

Figure 3.3 reports the SEM images of MF8020(I) and M100(II) powders after ball milling. It is possible to see that the powders were mainly composed of quite large aggregates constituted by particles with size smaller than 1 μm.

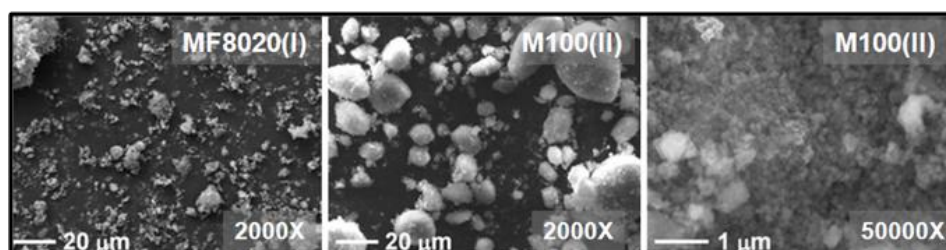


**Figure 3.3:** SEM images of ball milled MF8020(I) and M100(II) powders [adapted from Ref. 3.1].

### 3.2 Electrochemical tests

The electrochemical characterization of M100(I), MF8020(I) and MF7030(I) composite electrodes was carried out by galvanostatic-potentiostatic charge (CC-CV) and galvanostatic discharge cycles (CC) at 30 °C and 50 °C. The charge steps consisted in CC at 0.1C up to 4.4 V, followed by CV with current cut off at 0.05C; the cells were then discharged at 0.1C with potential cut-down of 2.3 V. Figure 3.4 compares voltage discharge profiles at 0.1C and 50 °C of fully charged electrodes. As already reported in literature [3.3], the coexistence of Mn and Fe in the olivine structure produces a beneficial effect, enhancing the total discharge capacity. At the first discharge cycle electrode MF8020(I) delivered a capacity of 135 mAh g<sup>-1</sup> with a columbic efficiency of ca. 80% while MF100(I) shows a lower capacity of 80 mAh g<sup>-1</sup> (columbic efficiency ca. 50%). Figure 3.5 shows the cycling stability at 50 °C of the three electrodes tested by charge (CC-CV)-discharge (CC) at 0.1C.

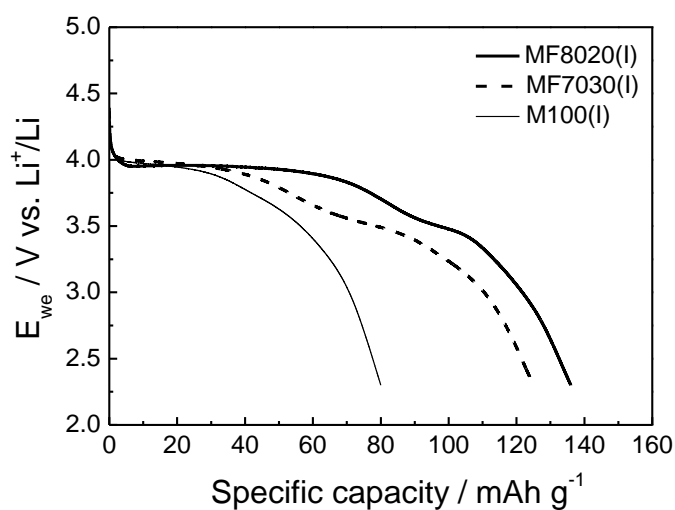


**Figure 3.4:** First CC discharge curves (50 °C) at 0.1C of M100(I), MF8020(I) and MF7030(I) fully charged, CC(0.1C)-CV, electrodes [adapted from Ref. 3.1].

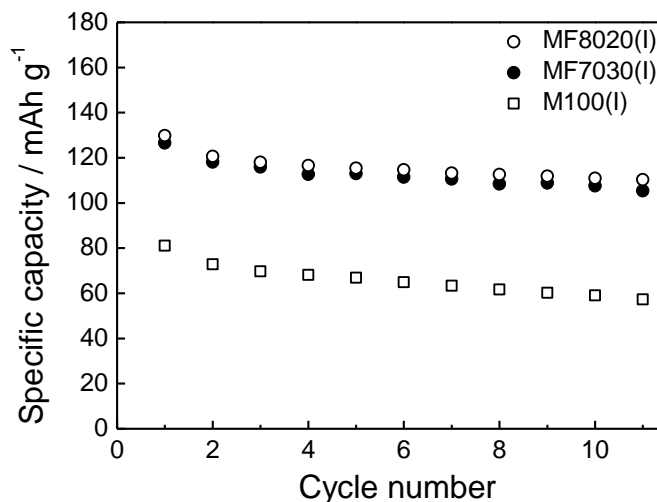


**Figure 3.5:** Specific discharge capacity at 0.1C and 50 °C vs. cycle number of MF8020(I), MF7030(I) and M100(I) electrodes [adapted from Ref. 3.1].

With the aim to evaluate the discharge capability of MF8020(I) at 50 °C, different charge/discharge cycles were performed changing the discharge current. At each cycle the electrode was fully oxidized by CC (0.1C)-CV charge and discharged at different C-rates from 0.1C to 2C down to 2.3 V. Figure 3.6 shows the so obtained results. It is possible to notice that, as expected, higher is the C-rate lower is the discharge capacity, however at the highest C-rate (2C) a delivered capacity of 80 mAh g<sup>-1</sup> represents a good value for a manganese-iron phosphate electrode with a total carbon content of ca. 20%.

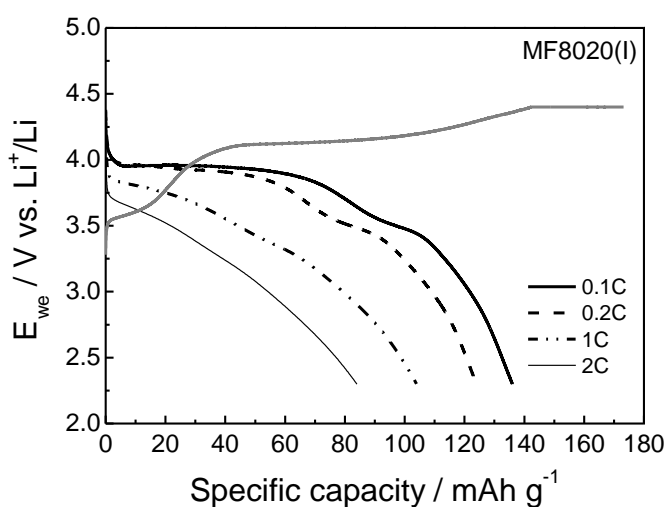


**Figure 3.6:** Discharge capability (50 °C) at 0.1C, 0.2C, 1C and 2C of fully charged CC(0.1C)-CV MF8020(I) electrode [adapted from Ref. 3.1].

The electrochemical behavior of M100(II), was tested by a discharge capability protocol at 50 °C and the results are reported in Figure 3.7. The electrode was charged at CC (0.1C up to 4.6 V), followed by CV (current cut off at 0.05C) and discharge at CC at various C-rates from 0.1C to 2C (down to 2.5 V).

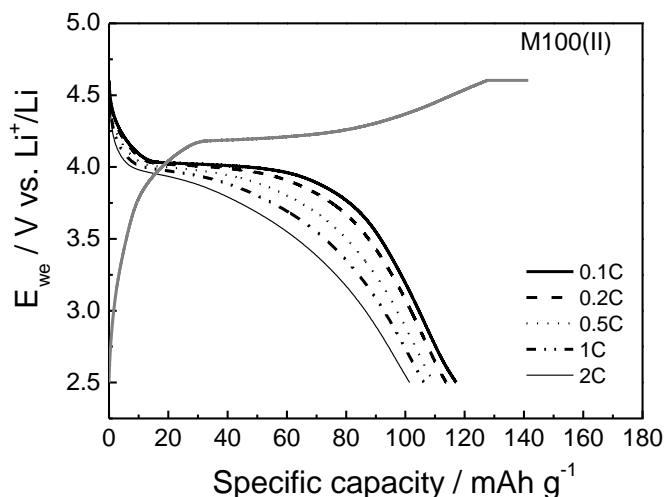


**Figure 3.7:** Discharge capability (50 °C) at 0.1C, 0.2C, 0.5C, 1C and 2C of fully charged CC(0.1C)-CV M100(II) electrode [adapted from Ref. 3.1].

From Figure 3.7 it is possible to see that the M100(II) composite electrode provided a discharge capacity of about 100 mAh g<sup>-1</sup> at the higher current of 2C, this capacity amount represent an interesting value for LiMnPO<sub>4</sub> - based electrode at this C-rate.

For the same M100(II) - based cell was also evaluate the charge capability at 50 °C by CC charge (up to 4.6 V) at various C-rates from 0.1C to 2C and CC discharge at 0.1C (down to 2.5 V). Figure 3.8 shows the results of this charge capability test. As an example the discharge profiles related to the charge at 0.1C and 2C are reported, all the other discharge profiles showed a similar behavior with a recovered charge > 96 %. The reported store charge value of 65 mAh g<sup>-1</sup> at 2C can be considered a good result for such material.

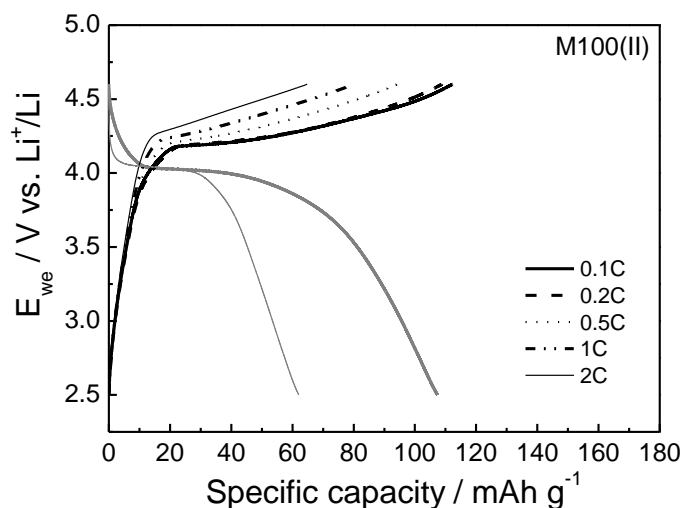


**Figure 3.8:** Charge capability (50 °C) at 0.1C, 0.2C, 0.5C, 1C and 2C of M100(II) electrode discharge at CC (0.1C) [adapted from Ref. 3.1].

Figure 3.9 reports the stability tests on M100(II) electrodes performed at two temperatures, 30 °C and 50 °C, by CC (0.1C up to 4.6 V) - CV (0.05C) charge and CC discharge (0.1C down to 2.5 V) cycles. The results demonstrate the good stability of the M100(II) electrodes over 20 cycles at both temperatures with coulombic efficiency values at the first cycle of ca. 75% increasing to ca. 93% in the subsequent cycles.

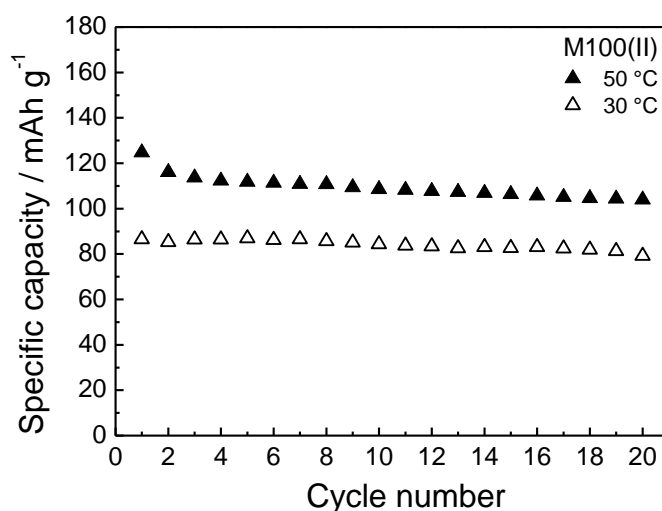


**Figure 3.9:** Specific discharge capacity at 0.1C vs. cycle number of M100(II) electrodes [adapted from Ref. 3.1].

Comparing the results of Figure 3.5 and Figure 3.9 it is possible to see that the M100(II) performs significantly better than M100(I), and comparable to the iron-containing MF8020(I). This evidence demonstrates the efficacy of the sol-gel method II for the synthesis of LiMnPO<sub>4</sub> from completely soluble precursors with a higher amount of citric acid which provides the highest carbon-coating (14 % wt. for M100(II) compared to 6 % wt. for M100(I)).

A summary of the first discharge capacity at 30 °C and 50 °C for the various electrodes is reported in Figure 3.10 which highlights that working at the highest temperature of 50 °C has a beneficial impact on the delivered capacity by all the electrodes, improving the Li<sup>+</sup> intercalation/deintercalation kinetics.

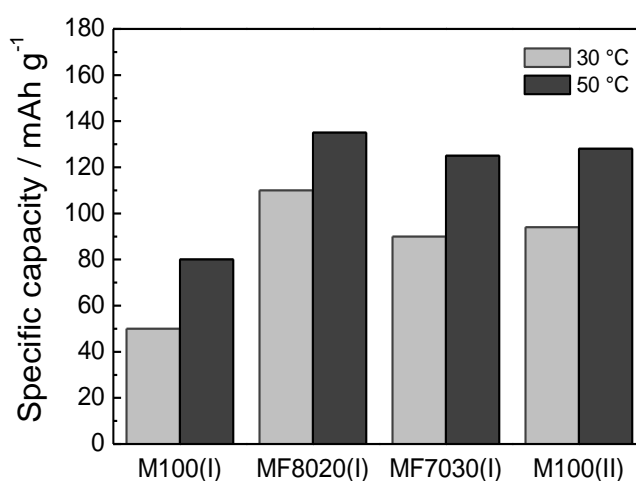


**Figure 3.10:** Comparison of the first discharge capacity value of the fully charged electrodes [adapted from Ref. 3.1].

### 3.3 Summary of LiMn<sub>1-x</sub>Fe<sub>x</sub>PO<sub>4</sub> (x = 0; 0.2; 0.3) as cathode materials for lithium-ion batteries

Carbon-coated LiMnPO<sub>4</sub>, LiMn<sub>0.8</sub>Fe<sub>0.2</sub>PO<sub>4</sub> and LiMn<sub>0.7</sub>Fe<sub>0.3</sub>PO<sub>4</sub> were prepared according to two different sol-gel method from partially water soluble precursors (method I) and, for LiMnPO<sub>4</sub>, even from totally soluble precursors (method II). Synthesis of LiMnPO<sub>4</sub> from method II provided an attractive carbon-coated material with the following

performance at 0.1C: 95 mAh g<sup>-1</sup>, capacity fade per cycle of 0.4% at 30 °C and 125 mAh g<sup>-1</sup>, capacity fade per cycle of 0.5% at 50 °C.

Considering the inexpensive nature of proposed synthetic route, the reported results evidence attractive capacity values and demonstrate that a good performing Mn-based olivine is viable, even without the coexistence of iron. The exclusion of Fe, which works at 3.5 V, is an advantage for battery energy because LiMnPO<sub>4</sub> delivers the most part of the charge at 4 V.

### 3.4 References

- [3.1] L. Damen, F. De Giorgio, S. Monaco, et al, *J. Pow. Sources*, **218** (2012) 250  
(Reproduced with permission Copyright 2012 Elsevier)
- [3.2] C. Delacourt, L. Laffont, R. Bouchet, et al, *J. Electrochem. Soc.*, 152 (2005) A913
- [3.3] A. Yamada, Y. Kudo, K.Y. Liu, *J. Electrochem. Soc.*, **148** (2001) A747



# Chapter 4

## Lithium-oxygen battery

As already mentioned in the first Chapter, to have a competitive EV replacing the conventional internal combustion engine cars, specific energy values referred to the battery pack higher than  $1000 \text{ Wh kg}^{-1}$  are requested. This high specific energy can be obtained, on the basis of theoretical calculation, with lithium-oxygen batteries technology. In the frame of the European project LABOHR “*Lithium-Air Batteries with split Oxygen Harvesting and Redox processes*” (FP7-2010-GC-ELECTROCHEMICALSTORAGE, contract no. 265971), the feasibility of  $\text{Li}/\text{O}_2$  battery operating in ionic liquid-based electrolytes was investigated. In this PhD work three aspects have been investigated: basic aspects of the oxygen redox reaction (ORR) in different IL-based electrolytes (Section 4.1 and Ref. [4.1]), synthesis and characterization of porous carbons as electrode materials for high capacity  $\text{Li}/\text{O}_2$  batteries (Section 4.2 and Ref. [4.2]) and study of limiting factors to the electrode capacity and cell cycle life (Section 4.3 and Ref. [4.3]).

### 4.1 Oxygen redox reaction in ionic liquid-based electrolytes

The oxygen redox reaction (ORR) has been investigated in a variety of ILs by several groups, demonstrating a high stability of the superoxide anion and its reoxidation to molecular oxygen [4.4-4.7]. In this PhD work, in order to assess the feasibility of a lithium/oxygen battery operating in pyrrolidinium-based electrolytes, the ORR was investigated at different temperatures in the ultrapure ILs reported in Section 2.2.1, in absence and with 0.1M LiTFSI.  $\text{PYR}_{14}\text{TFSI}$  and  $\text{PYR}_{1(201)}\text{TFSI}$  ionic liquids were already studied as electrolytes for lithium-ion batteries [4.8], the alkylether side chain gives a lower viscosity and higher ionic conductivity to  $\text{PYR}_{1(201)}\text{TFSI}$  compared to  $\text{PYR}_{14}\text{TFSI}$  and promotes  $\text{Li}^+$  ion diffusion. Preliminary voltammetric studies showed that oxygen solubility is promoted by fluorine content of the IL. Hence, ORR was investigated in liquid

PYR<sub>14</sub>-salts with anions of increasing amount of fluorine atoms like bis(pentafluoroethanesulfonyl)imide (BETI) and (nonafluorobutylsulfonyl) (trifluoromethanesulfonyl)imide (IM<sub>14</sub>). In the following section, results obtained by CV, RDE, and CA at glassy carbon electrodes are reported and discussed in relation to the physical-chemical properties of the used ionic liquids. This study provided the concentration and the diffusion coefficient of O<sub>2</sub> in pure ILs as well as the potentials of the reduction and reoxidation processes. Table 4.1 reports dynamic viscosity ( $\eta$ ) and conductivity ( $\sigma$ ) of the investigated ILs; the conductivities of their solutions with the 0.1 M LiTFSI are reported in brackets. PYR<sub>1(201)</sub>TFSI is the salt with the highest conductivity and lowest viscosity among the investigated ILs. The increase of the anion size from TFSI to BETI and IM<sub>14</sub> results in the increase of viscosity and decrease of ion conductivity. The presence of lithium salt 0.1 M, added to investigate the ORR in a battery-like behavior, only slightly affects viscosity and conductivity of the electrolyte.

**Table 4.1:** Dynamic viscosity ( $\eta$ ) and conductivity ( $\sigma$ ) at 30 °C and 60 °C of the investigated ILs; the conductivities of the corresponding solutions with 0.1 M LiTFSI are reported in brackets.

IL	$\eta$ /cP		$\sigma$ /mS cm <sup>-1</sup>	
	30 °C	60 °C	30 °C	60 °C
PYR <sub>14</sub> FSI [4,9]	48	21	5.0	9.0
PYR <sub>14</sub> TFSI	60	21	3.3 (3.0)	8.5 (8.1)
PYR <sub>1(201)</sub> TFSI	38	15	4.2 (4.0)	9.9 (9.6)
PYR <sub>14</sub> BETI	200	52	0.9 (0.8)	3.2 (2.9)
PYR <sub>14</sub> IM <sub>14</sub>	290	65	0.5 (0.5)	2.1 (1.8)

#### 4.1.1 ORR at GC electrodes in ILs without lithium salt

Figure 4.1.1a reports, as example, the CVs at GC electrode in PYR<sub>14</sub>TFSI without lithium salt at 20 mV s<sup>-1</sup> after saturation with O<sub>2</sub>. Except for the case of PYR<sub>14</sub>FSI (see Figure 4.1.1b) all the other ILs show similar features in agreement with studies reported in literature on the ORR in pure PYR<sub>14</sub>TFSI [4.4, 4.6, 4.7, 4.10]. The first reduction peak (pR) at ca. 1.8 V vs. Li<sup>+</sup>/Li is due to generation of superoxide anion. O<sub>2</sub><sup>-</sup> is stable enough in IL to be reoxidized in the back CV scan at ca. 2 V vs. Li<sup>+</sup>/Li (pO). At 3.5 V vs. Li<sup>+</sup>/Li a

small peak (pO'') appears which may be attributed to oxidation of small amounts of peroxide  $O_2^{2-}$  that can be formed after chemical disproportionation of  $O_2^{\cdot-}$ .

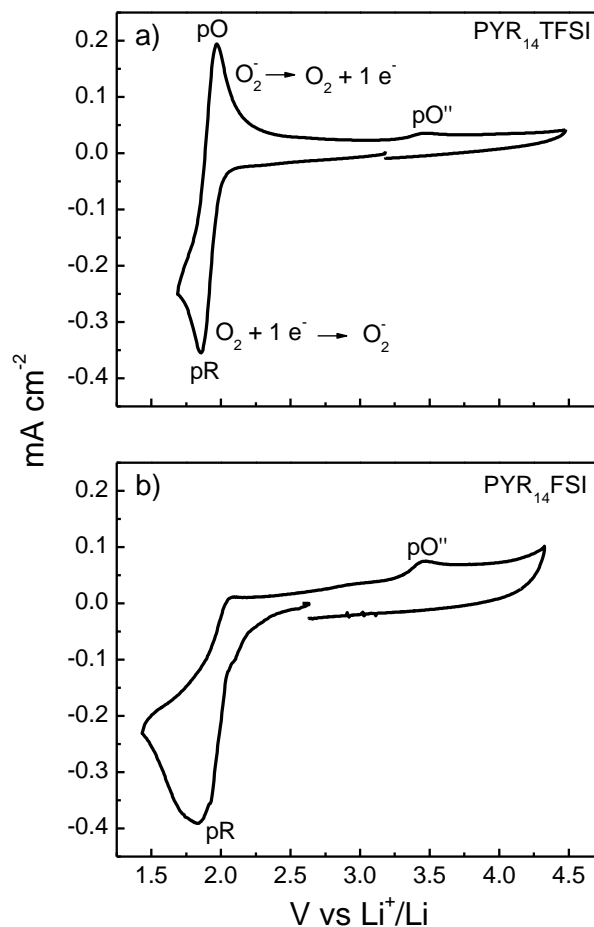


**Figure 4.1.1:** CVs at GC electrode in pure  $PYR_{14}TFSI$  (a) and  $PYR_{14}FSI$  (b) at  $20 \text{ mV s}^{-1}$  and  $30 \text{ }^\circ\text{C}$ .

The absence of the oxidation peak pO and the high difference between reduction and oxidation charges in the  $PYR_{14}FSI$  voltammogram, suggest that  $O_2$  reduction process is irreversible in such electrolyte. For this reason, despite the fact that  $PYR_{14}FSI$  is a good SEI forming for the Li metal anode [4.11], it was not considered for Li/ $O_2$  battery. The ORR was further investigated only in  $PYR_{14}TFSI$ ,  $PYR_{1(2O1)}TFSI$ ,  $PYR_{14}BETI$  and  $PYR_{14}IM_{14}$  ionic liquids and Figure 4.1.2 shows the CVs at different scan rate in these  $O_2$ -saturated pure ILs at  $30 \text{ }^\circ\text{C}$  and  $60 \text{ }^\circ\text{C}$ . Table 4.1.1 summarizes the current density ( $i_{pR}$ ) and potential ( $E_{pR}$ ) of the main reduction peak, the difference ( $E_{pR} - E_{pR/2}$ ) between  $E_{pR}$  and the potential where the reduction current is  $i_{pR}/2$  ( $E_{pR/2}$ ) and the potential difference between reduction and oxidation peaks ( $E_{pR} - E_{pO}$ ) from the CVs reported in Figure 4.1.2.

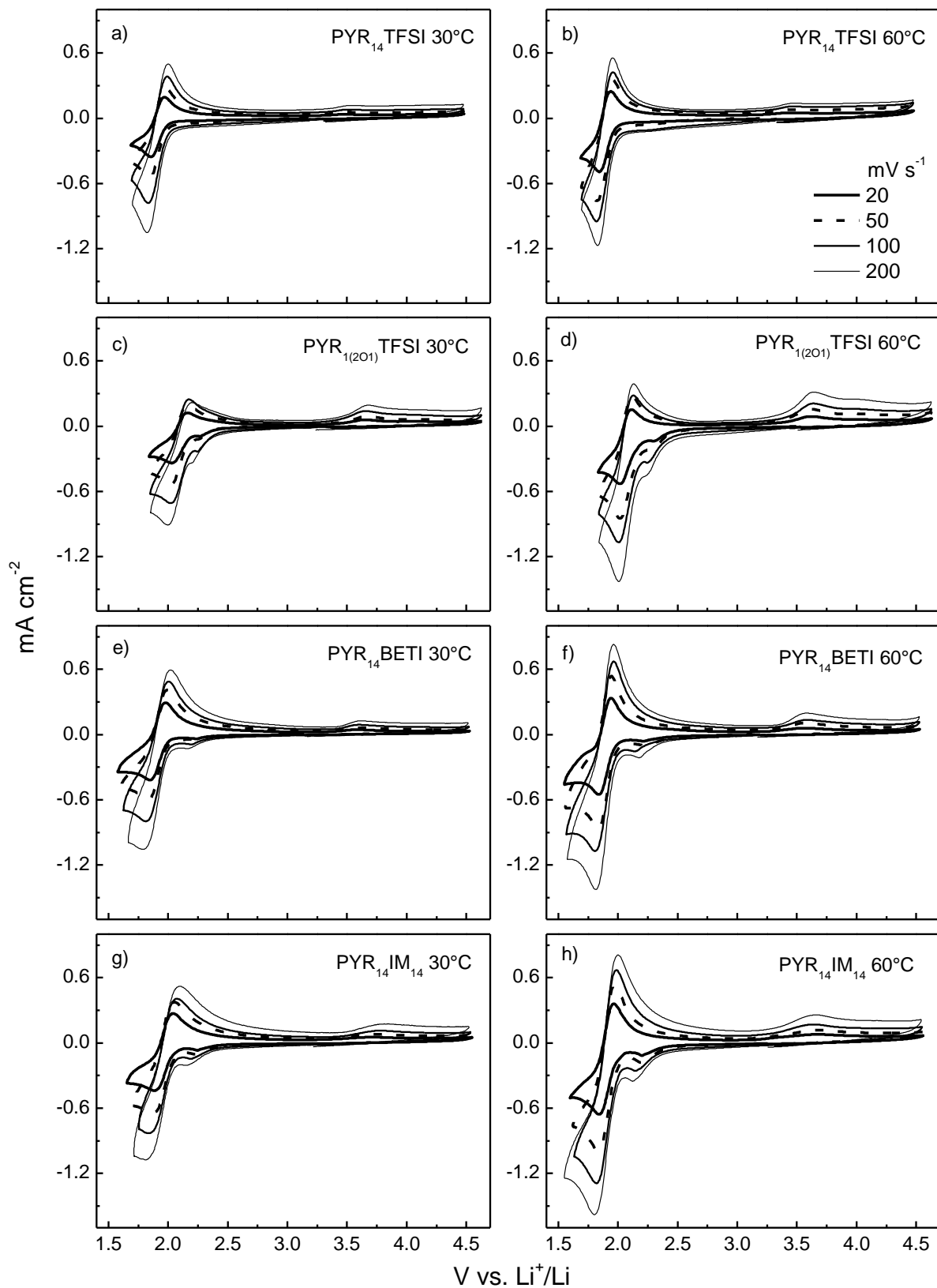


**Figure 4.1.2:** CVs at GC electrode in O<sub>2</sub>-saturated ILs at 30 °C and 60 °C, at different scan rates (20, 50, 100, 200 mV s<sup>-1</sup>) [adapted from Ref. 4.1].

**Table 4.1.1:** Values at different scan rates ( $v$ ) of the principal reduction peak current density ( $i_{pR}$ , background current subtracted) and potential ( $E_{pR}$ ), differences ( $E_{pR}-E_{pR/2}$ ) and ( $E_{pR} - E_{pO}$ ) from GC CVs in different  $O_2$ -saturated ILs at 30 °C and 60 °C and values of  $\psi$ ,  $\chi$ ,  $\alpha$ ,  $K(\psi,\alpha)$  and  $E_{1/2}$  obtained by the Nicholson and Matsuda and Ayabe methods for quasi-reversible processes. The potential values are given vs  $Li^+/Li$ .

IL	T °C	v mV s <sup>-1</sup>	$i_{pR}$ mA cm <sup>-2</sup>	$E_{pR}$ V	$E_{pR} - E_{pR/2}$ mV	$E_{pR} - E_{pO}$ mV	$\psi$	$10^2 \chi$ V <sup>1/2</sup> s <sup>-1/2</sup>	$\alpha$	$K(\psi,\alpha)$	$E_{1/2}$ V
PYR <sub>14</sub> TFSI	30	10	0.26	1.86	73	102	0.54	4.7±0.1	0.40	0.89	1.93 ±0.01
		20	0.33	1.86	77	114	0.40				
		50	0.47	1.84	88	136	0.27				
		100	0.69	1.84	90	153	0.21				
		200	0.96	1.83	93	168	0.18				
	60	10	0.31	1.85	71	86	0.93	8.0±1.1	0.51	0.94	1.90 ±0.01
		20	0.44	1.84	74	97	0.63				
		50	0.65	1.82	86	122	0.34				
		100	0.81	1.82	84	131	0.29				
		150	1.03	1.83	81	119	0.36				
PYR <sub>1(201)</sub> TFSI	30	10	0.27	2.04	100	109	0.46	3.6±0.6	0.35	0.85	2.12 ±0.01
		20	0.31	2.03	106	135	0.27				
		50	0.53	2.02	106	150	0.22				
		100	0.66	2.03	114	147	0.23				
		150	0.72	2.01	115	167	0.18				
	60	10	0.38	2.02	103	88	0.86	7.1±1.2	0.29	0.89	2.08 ±0.01
		20	0.49	2.02	100	91	0.77				
		50	0.80	2.02	105	98	0.61				
		100	0.99	2.01	111	118	0.37				
		150	1.18	2.01	114	127	0.31				
PYR <sub>14</sub> BETI	30	20	0.41	1.85	93	125	0.32	4.9±0.2	0.37	0.85	1.94 ±0.01
		50	0.52	1.83	97	155	0.21				
		100	0.76	1.82	118	186	0.14				
		150	0.88	1.80	129	208	0.10				
		200	1.01	1.79	136	226	0.09				
	60	20	0.52	1.84	82	100	0.58	8.3±1.7	0.40	0.89	1.90 ±0.01
		50	0.84	1.83	89	109	0.45				
		100	0.99	1.81	101	153	0.20				
		150	1.24	1.81	108	155	0.20				
		200	1.33	1.82	107	142	0.24				
PYR <sub>14</sub> IM <sub>14</sub>	30	20	0.43	1.88	108	155	0.24	3.8±0.5	0.35	0.78	1.99 ±0.01
		50	0.61	1.88	117	166	0.17				
		100	0.79	1.84	135	223	0.09				
		150	0.90	1.83	150	240	0.08				
		200	0.99	1.81	160	280	0.06				
	60	20	0.64	1.85	91	120	0.36	4.5±1.0	0.40	0.88	1.92 ±0.01
		50	0.96	1.84	97	131	0.29				
		100	1.21	1.82	111	158	0.20				
		150	1.40	1.82	113	182	0.15				
		200	1.48	1.80	123	190	0.14				

All the CVs of Figure 4.1.2 show the similar features that were previously discussed for the  $\text{PYR}_{14}\text{TFSI}$  voltammogram reported in Figure 4.1.1a. The small prewave visible in some cases before the main reduction peak (pR) is probably due to the adsorption of the  $\text{O}_2$  reduction product on the GC electrode surface.

Unlike the CVs of Nernstian process, the CVs of Figure 4.1.2 show that the  $E_{\text{pR}}$  values shift to more positive potentials and the differences  $(E_{\text{pR}} - E_{\text{pO}})$  and  $(E_{\text{pR}} - E_{\text{pR}/2})$  amplify with the increase of the scan rate ( $\nu$ ). These factors indicate that the  $\text{O}_2$  reduction in the examined ILs is a quasi-Nernstian (alias quasi-reversible) process. An approach different from the Randles-Sevcik equation [4.12], which applies for reversible process, is needed to evaluate from the CVs analysis the  $(D_{\text{O}}^{1/2}C_{\text{O}})$  values, where  $(D_{\text{O}})$  is the diffusion coefficient and  $(C_{\text{O}})$  the concentration of the electroactive species.

For a diffusion-controlled, quasi-reversible process the value of the reduction peak ( $i_{\text{pR}}$ ) is related to  $(D_{\text{O}}^{1/2}C_{\text{O}})$  by equation 4.1

$$i_{\text{pR}} = 0.4463 \sqrt{\frac{F^3}{RT}} n^{3/2} D_{\text{O}}^{1/2} C_{\text{O}} \nu^{1/2} K(\psi, \alpha) \quad (4.1)$$

where  $K(\psi, \alpha)$  is a measure of the difference of the peak current from the value featured in the case of a Nernstian process and depends on the transfer coefficient  $\alpha$  and the  $\psi$  function which in turn depends on the scan rate as shown in equation 4.2.

$$\psi = \frac{\chi}{\sqrt{\nu}} = \frac{(D_{\text{O}}/D_{\text{R}})^{\alpha/2} k^{\circ}}{\sqrt{\pi f D_{\text{O}} \sqrt{\nu}}} \quad (4.2)$$

where  $D_{\text{O}}$  and  $D_{\text{R}}$  are the diffusion coefficients of  $\text{O}_2$  and  $\text{O}_2^-$  respectively,  $k^{\circ}$  represents the standard heterogeneous rate constant, and  $f = nF/RT$  ( $F$  and  $R$  are the Faraday and the ideal gas constants,  $n$  the electron number and  $T$  the temperature).

The  $K(\psi, \alpha)$  values that are given in the Table 4.1.1 were obtained from the Matsuda and Ayabe working function of Figure 4.1.3, once  $\psi$  and  $\alpha$  values were determined at the each scan rates [4.12, 4.13].

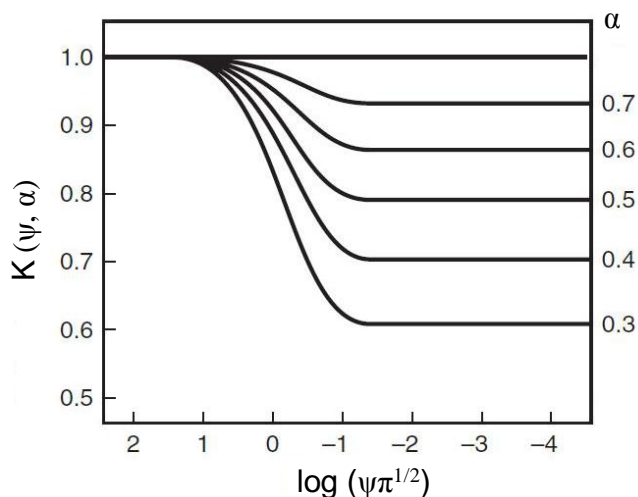


**Figure 4.1.3:** Matsuda and Ayabe working curve showing the variation of  $K(\psi, \alpha)$  with  $\log(\psi \pi^{1/2})$  at different  $\alpha$  values [adapted from Ref. 4.12]

Following the Nicholson method [4.12, 4.14], at each scan rate, the  $\psi$  values were evaluated from the difference ( $E_{pR} - E_{pO}$ ) by the working function reported in Figure 4.1.4 and the results are reported in Table 4.1.1.

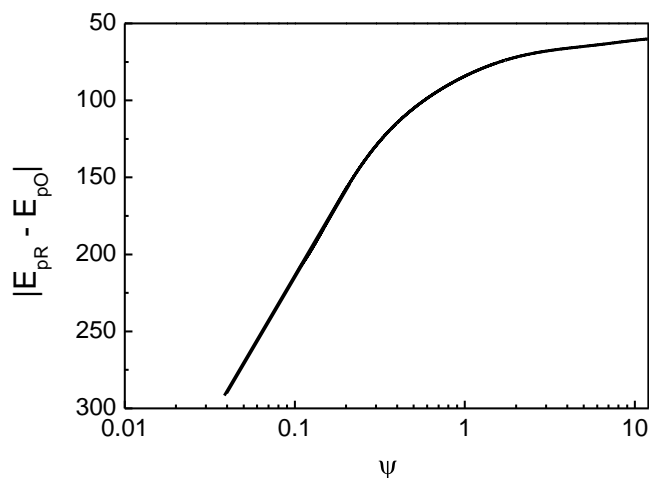


**Figure 4.1.4:** Nicholson working curve showing the variation of  $(E_{pR} - E_{pO})$  with  $\psi$  [adapted from Ref. 4.14]

The  $\alpha$  values were evaluated by the  $\Delta(\psi\pi^{1/2}, \alpha)$  Matsuda and Ayabe working function of Figure 4.1.5 that is related to  $(E_{pR} - E_{pR/2})$  as described by equation 4.3.

$$\Delta(\psi\pi^{1/2}, \alpha) = |E_{pR} - E_{pR/2}| \frac{F}{RT} \quad (4.3)$$

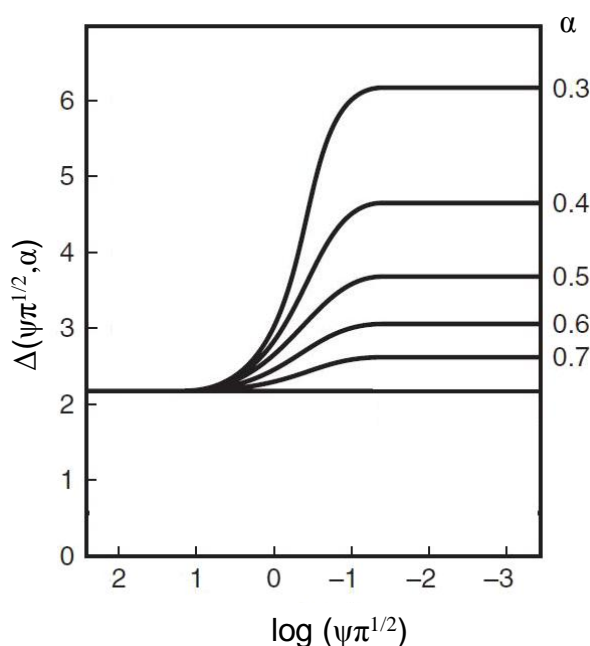


**Figure 4.1.5:** Matsuda and Ayabe working curve showing the variation of  $\Delta(\psi\pi^{1/2}, \alpha)$  with  $\log(\psi\pi^{1/2})$  at different  $\alpha$  values [adapted from Ref. 4.12]

The resulting  $\alpha$  values averaged over the different scan rates and reported in Table 4.1.1 are between 0.3 and 0.5 which is a range where the Nicholson treatment applies.

For all the studied ILs,  $\psi$  showed a linear dependence from  $\frac{1}{\sqrt{v}}$  with a slope that gave the values of  $\chi$  thus validating the method used for the analysis of the CV curves of Figure 4.1.2.

The  $\frac{i_{pR}}{K(\psi, \alpha)}$  vs.  $v^{1/2}$  plots (see equation 4.1) were linear for the various ILs, thus confirming that ORR in the investigated ILs is a diffusion controlled process with  $n = 1$ . Deviation from linearity only occurred for scan rates  $> 150 \text{ mV s}^{-1}$  presumably for a not rigorous correction of the ohmic drop. The slopes of such plots provided the  $(D_O^{1/2}C_O)$

parameters listed in Table 4.1.2 that, at a given temperature, increase in the order  $\text{PYR}_{14}\text{TFSI} \leq \text{PYR}_{1(201)}\text{TFSI} < \text{PYR}_{14}\text{BETI} < \text{PYR}_{14}\text{IM}_{14}$ .

The increase of temperature leads to the increase of the ORR voltammetric currents in all the investigated pure ILs. Table 4.1.1 evidences that at 60 °C  $E_{\text{pR}} - E_{\text{pR}/2}$  and  $E_{\text{pR}} - E_{\text{pO}}$  are narrower and the  $K(\psi, \alpha)$  values are more closed to 1 than those at 30 °C indicating that temperature raise renders  $\text{O}_2$  reduction more Nernstian. Also the slopes of the  $\frac{i_{\text{pR}}}{K(\psi, \alpha)}$  vs.  $v^{1/2}$  plots, hence the  $(D_{\text{O}}^{1/2}C_{\text{O}})$  values, increase with temperature.

Table 4.1.1 reports the value of half-wave potentials  $E_{1/2}$  averaged over the different scan rates. At each scan rate  $E_{1/2}$  depends from  $E_{\text{pR}}$  and the  $\Xi(\psi\pi^{1/2}, \alpha)$  Matsuda and Ayabe working functions as described by equation 4.4.

$$E_{1/2} = E_{\text{pR}} + \Xi(\psi\pi^{1/2}, \alpha) \frac{RT}{F} \quad (4.4)$$

The values of  $\Xi(\psi\pi^{1/2}, \alpha)$  were determined by the working functions of Figure 4.1.6 using the  $\psi$  and  $\alpha$  data determined at the different scan rates.

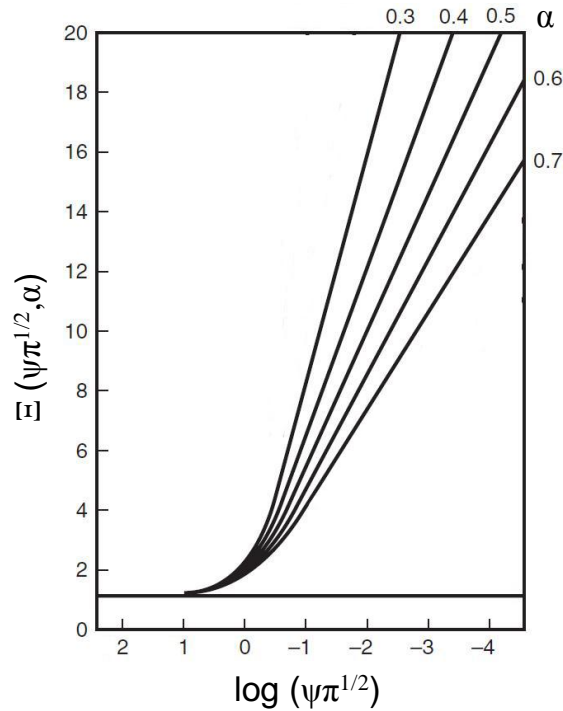


**Figure 4.1.6:** Matsuda and Ayabe working curve showing the variation of  $\Xi(\psi\pi^{1/2}, \alpha)$  with  $\log \psi\pi^{1/2}$  at different  $\alpha$  values [adapted from Ref. 4.12]

$E_{1/2}$  is related to the formal potential  $E^{\circ'}$  by the equation 4.5:

$$E_{1/2} = E^{\circ'} - \frac{RT}{nF} \ln \sqrt{\frac{D_O}{D_R}} \quad (4.5)$$

If  $D_O$  and  $D_R$  show similar values the  $E_{1/2}$  can be taken as a good approximation of  $E^{\circ'}$ . In the case of ILs because of ion association, the diffusion coefficient  $D_R$  of the superoxide anion which is a charged species is lower than that of oxygen and  $D_O/D_R$  may differ from the unity, ranging between 2 up to 60 [4.4, 4.6, 4.15-4.17]. If the highest  $D_O/D_R$  ratio is considered, the  $E_{1/2}$  would differ from  $E^{\circ'}$  by ca. 50 mV. This means that the formal potential of the ORR process in the investigated ILs would be in the 2.0 - 2.2 V vs.  $\text{Li}^+/\text{Li}$  range which well compares with the data for the  $\text{O}_2/\text{O}_2^-$  couple in conventional electrolytes with organic solvent and ammonium salt as supporting electrolyte [4.18].

**Table 4.1.2:** Oxygen diffusion coefficient ( $D_O$ ) and concentration ( $C_O$ ) data from the combination of the  $D_O^{1/2}C_O$  and  $D_O \cdot C_O$  values obtained by analyses of the GC CVs and by the UGC CA stationary currents averaged over the 5-10 s time range ( $\langle i_{ss} \rangle$ ) from experiments at the reported potentials in  $\text{O}_2$ -saturated ILs at 30 °C and, reported in brackets, at 60 °C.

IL	GC CVs	UGC CAs			$10^6 D_O$ $\text{cm}^2 \text{s}^{-1}$	$10^6 C_O$ $\text{mol cm}^{-3}$
	$10^9 D_O^{1/2} C_O$ $\text{mol s}^{-0.5} \text{cm}^{-2}$	V vs. $\text{Li}^+/\text{Li}$	$\langle i_{ss} \rangle$ nA	$10^{11} D_O \cdot C_O$ $\text{mol s}^{-1} \text{cm}^{-1}$		
PYR <sub>14</sub> TFSI	10 (11)	1.65 (1.60)	5.7 (9.4)	3.5 (5.7)	12 (27)	2.9 (2.1)
PYR <sub>1(201)</sub> TFSI	10 (15)	1.81 (1.83)	5.5 (11.2)	3.3 (6.8)	11 (18)	3.0 (3.8)
PYR <sub>14</sub> BETI	17 (22)	1.75 (1.68)	5.0 (11.3)	3.0 (6.2)	3 (8)	10.7 (7.8)
PYR <sub>14</sub> IM <sub>14</sub>	19 (28)	1.76 (1.72)	4.6 (10.6)	2.8 (6.4)	2 (5)	14.3 (14.1)

In order to separately evaluate  $D_{O_2}$  and  $C_{O_2}$ , ORR was studied by chronoamperometric potential step measurements (CA) on GC-ultramicroelectrode (UGC) from the initial potential of 3.3 V vs.  $Li^+/Li$ , where  $O_2$  reduction is not occurring, to final values where stationary currents were reached. The resulting CAs at 30 °C and 60 °C are reported in Figure 4.1.7.

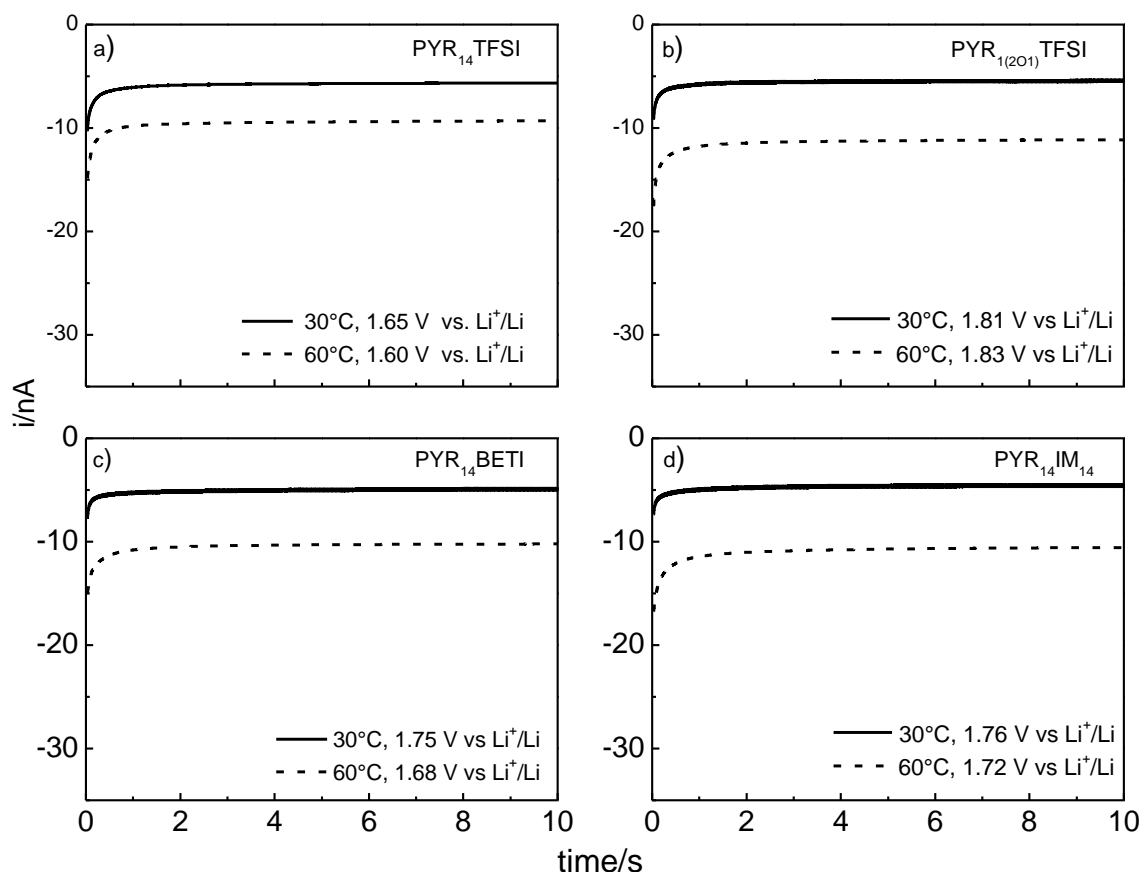


**Figure 4.1.7:** CAs profiles upon potential steps at GC-ultramicroelectrode from 3.3 V vs.  $Li^+/Li$  to the values indicated by the labels, in different  $O_2$ -saturated ILs at 30 °C and 60 °C [adapted from Ref. 4.1].

The stationary current values  $\langle i_{ss} \rangle$  were averaged in the 5-10 s time range and used to evaluate the  $(D_{O_2} \cdot C_{O_2})$  data reported in Table 4.1.2 by equation 4.6:

$$i_{ss} = 4 n F r D_{O_2} C_{O_2} \quad (4.6)$$

where  $r$  is the UGC radius.

By combining the  $(D_O \cdot C_O)$  and  $(D_O^{1/2} C_O)$  values obtained by UGC CAs and GC CVs, respectively, the  $D_O$  and  $C_O$  parameters reported in Table 4.1.2 were obtained. The Table shows that at a given temperature  $D_O$  is affected by IL viscosity and decreases in the order  $\text{PYR}_{1(201)}\text{TFSI} > \text{PYR}_{14}\text{TFSI} > \text{PYR}_{14}\text{BETI} > \text{PYR}_{14}\text{IM}_{14}$ ;  $C_O$  increases in the order  $\text{PYR}_{14}\text{TFSI} \cong \text{PYR}_{1(201)}\text{TFSI} < \text{PYR}_{14}\text{BETI} < \text{PYR}_{14}\text{IM}_{14}$ , i.e. it seems to be affected by fluorine content in the anion. For each IL the temperature increase does not significantly alter  $C_O$  and has the major effect on oxygen diffusion which becomes faster at 60 °C than at 30 °C. However, the  $D_O$  and  $C_O$  values reported in Table 4.1.2 have to be taken as a rough estimation because they may suffer from the fact that, as evinced by the UGC CVs in  $\text{PYR}_{14}\text{BETI}$  reported in Figure 4.1.8, the UGC electrodes did not feature well defined stationary currents. Independent methods for  $\text{O}_2$  solubility determination could provide more robust  $D_O$  data. Note that, in literature, the  $D_O$  and  $C_O$  values obtained by electrochemical methods in a given IL by different laboratories are greatly dispersed [4.4-4.7, 4.16, 4.17].

In Figure 4.1.8, the CVs at UGC feature peak-shaped anodic response even when a steady-state sigmoidal curve is obtained in the forward-going sweep and this supports the fact that the diffusion coefficient of  $\text{O}_2$  is higher than that of the superoxide anion that can associate to IL ions. According to Buzzeo at al., the generated superoxide is constrained to distances much closer to the electrode than those where oxygen is depleted and diffusion of the former specie appears planar while that of the latter is almost spherical (steady state) [4.15].

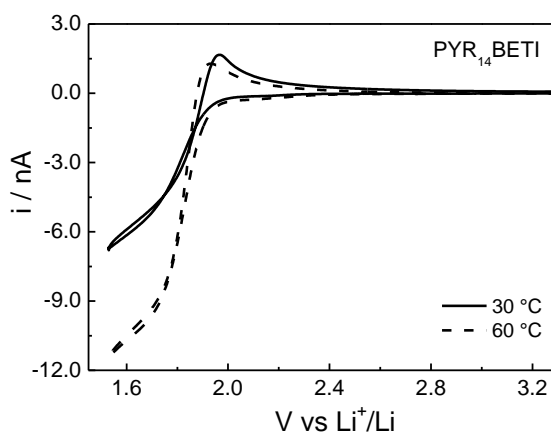


**Figure 4.1.8:** UGC CVs in  $\text{O}_2$ -saturated  $\text{PYR}_{14}\text{BETI}$  at 30 °C and 60 °C at  $50 \text{ mV s}^{-1}$  [adapted from Ref. 4.1].

The  $D_O$  values were used to calculate the tentative heterogeneous rate constants  $k^\circ$  at  $E^\circ$ . The  $k^\circ$  values result  $0.8 \times 10^{-3}$ ,  $0.7 \times 10^{-3}$ ,  $0.4 \times 10^{-3}$  and  $0.3 \times 10^{-3}$   $\text{cm s}^{-1}$  for  $\text{PYR}_{14}\text{TFSI}$ ,  $\text{PYR}_{1(2O1)}\text{TFSI}$ ,  $\text{PYR}_{14}\text{BETI}$  and  $\text{PYR}_{14}\text{IM}_{14}$ , respectively, at 30 °C, when the arbitrary value of  $D_O/D_R = 60$  for  $\text{PYR}_{14}\text{TFSI}$  is used for all the investigated ILs and double when  $D_O/D_R$  is 2. Regardless of the chosen  $D_O/D_R$  value, for all the ionic liquids the  $k^\circ$  nearly double when the temperature raises up to 60 °C. Under the strong approximation of having almost the same  $D_O/D_R$  for the different ILs, the  $k^\circ$  indicates that the ORR electron-transfer rate is favored at the highest temperature and slightly slows in the order  $\text{PYR}_{14}\text{TFSI} \geq \text{PYR}_{1(2O1)}\text{TFSI} > \text{PYR}_{14}\text{BETI} > \text{PYR}_{14}\text{IM}_{14}$ . Such trend could be affected by the  $E^\circ$  potentials at which  $k^\circ$  refers, hence to different activity coefficients ratios ( $\gamma_R/\gamma_O$ ) in the various ILs. In all the investigated ILs the CVs performed by UGC featured the same shape than that of the curves of Figure 4.1.8 that do not display well defined limiting currents, presumably for the onset of secondary reactions taking place below ca. 1.5 V vs.  $\text{Li}^+/\text{Li}$ . Note also that the ORR onset potential is cathodically shifted with respect to what observed in Figure 4.1.2, and this is presumably due to a different nature of the surface of glassy carbon electrodes used in the two experiments.

To validate the results obtained by GC and UGC electrodes, RDE linear sweep voltammetries (LSVs) in  $\text{O}_2$ -saturated  $\text{PYR}_{14}\text{TFSI}$  and  $\text{PYR}_{1(2O1)}\text{TFSI}$  without lithium salt were also performed at 30 °C and different rotation rate ( $\omega$ ). The LSVs were fitted to the Koutecky-Levich equation

$$\frac{1}{i} = \frac{1}{i_k} + \frac{1}{0.62 n F A D_O^{2/3} C_O \nu^{-1/6} \omega^{1/2}} \quad (4.7)$$

where  $i_k$  is the kinetically limited current and  $\nu$  the kinematic viscosity of the IL.

Given that equation 4.7 applies only when the hydrodynamic boundary layer,  $y \approx 3(\nu/\omega)^{1/2}$ , is much higher than the disk radius  $r_{\text{RDE}}$  (0.25 cm), and that  $\text{PYR}_{14}\text{TFSI}$  and  $\text{PYR}_{1(2O1)}\text{TFSI}$  feature kinematic viscosities of  $4.2 \times 10^{-1} \text{ cm}^2 \text{ s}^{-1}$  and  $2.6 \times 10^{-1} \text{ cm}^2 \text{ s}^{-1}$  (at 30 °C), only rotation rates faster than 1000 and 500 rpm were considered, respectively. Rotation speeds above 3000 rpm and 1600 rpm caused turbulence in  $\text{PYR}_{14}\text{TFSI}$  and

PYR<sub>1(2O1)</sub>TFSI, hence the corresponding data are not included in the analysis. At 30 °C, the very high viscosity of PYR<sub>14</sub>BETI and PYR<sub>14</sub>IM<sub>14</sub> causes that, in order to satisfy the  $y \gg i_{RDE}$  condition, the RDE studies of ORR in such ILs would require higher rotation speeds than those adopted for PYR<sub>14</sub>TFSI and PYR<sub>1(2O1)</sub>TFSI. On the other hand, the upper rotation rate limit is constrained by the occurrence of turbulences that make RDE technique fairly viable in the case of PYR<sub>14</sub>BETI and PYR<sub>14</sub>IM<sub>14</sub>. Hence, only the study for PYR<sub>14</sub>TFSI and PYR<sub>1(2O1)</sub>TFSI at 30 °C is reported.

Fitting of the RDE currents to equation 4.7 at the potentials where ORR is under the mixed kinetics/diffusion control provided the linear plots reported in Figure 4.1.9; from the slopes of these plots,  $D_O^{2/3}C_O$  values very similar for the two ILs and well comparing to what expected on the basis of Table 4.1.2 data were obtained (see Table 4.1.3). However, the  $D_O^{2/3}C_O$  parameters obtained by RDE are affected by a 10-20 % relative error which is too high for an accurate evaluation of  $D_O$  and  $C_O$ .

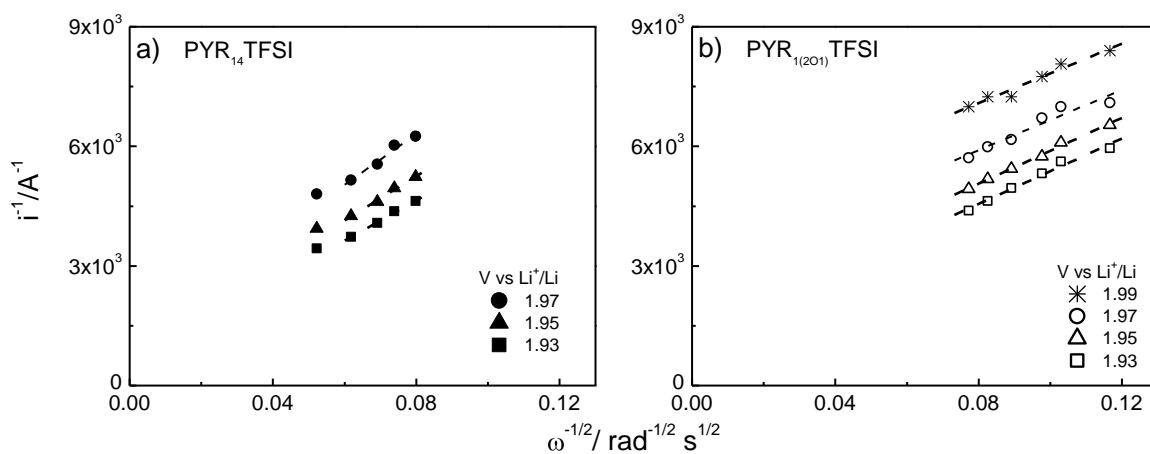


**Figure 4.1.9:** Koutecky-Levich plots of the RDE currents at different rotation rates and 30 °C in O<sub>2</sub>-saturated (a) PYR<sub>14</sub>TFSI at 5 mV s<sup>-1</sup> and (b) PYR<sub>1(2O1)</sub>TFSI at 10 mV s<sup>-1</sup> [adapted from Ref. 4.1].

**Table 4.1.3:**  $D_0^{2/3}C_0$  values, kinetics current at different electrode potentials ( $i_k$ ) from the Koutecky-Levich equation, and Tafel slope by RDE LSVs at 30 °C in  $O_2$ -saturated ILs without lithium salt.

IL	$10^9 D_0^{2/3}C_0$ mol cm <sup>-5/3</sup> s <sup>-2/3</sup>	V vs. Li <sup>+</sup> /Li	$i_k$ mA	Tafel slope mV decade <sup>-1</sup>
PYR <sub>14</sub> TFSI	1.8 ± 0.3	1.97	0.82	130 ± 25
		1.95	1.24	
		1.93	1.67	
PYR <sub>1(201)</sub> TFSI	2.0 ± 0.1	1.99	0.24	124 ± 13
		1.97	0.35	
		1.95	0.57	
		1.93	0.79	

The intercepts of the Koutecky-Levich straight lines reported in Table 4.1.3 were used to build the Tafel plots shown in Figure 4.1.10 where  $\log i_k$  is plotted vs. the electrode potential because we were not able to unambiguously evaluate the equilibrium potentials for ORR at RDE. The slopes of the Tafel plots are of ca. 120 - 130 mV decade<sup>-1</sup> (see Table 4.1.3) and are consistent with a one-electron reduction process, i.e. with the rate determining formation of the superoxide anion, with  $\alpha \cong 0.5$ .

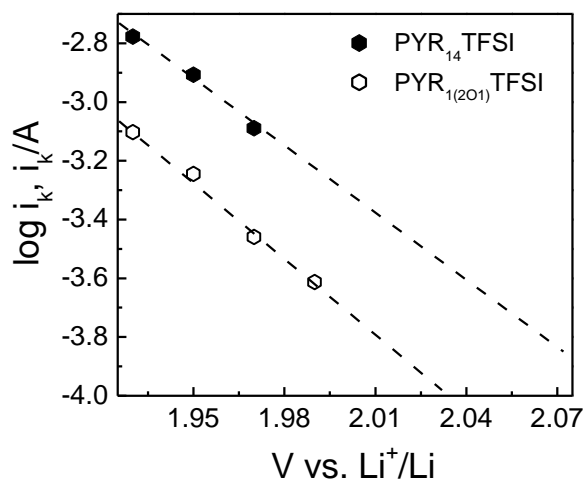


**Figure 4.1.10:** Tafel plots for ORR in PYR<sub>14</sub>TFSI (black) and PYR<sub>1(201)</sub>TFSI (white) at 30 °C [adapted from Ref. 4.1].

### 4.1.2 ORR in IL - LiTFSI solutions

In literature it has already been reported that the presence of 0.1 M LiTFSI makes oxygen reduction electrochemically irreversible in IL, renders superoxide unstable and promotes the formation of insoluble lithium-oxygen species that may passivate the electrode [4.10, 4.19]. Figure 4.1.11a, which reports the GC CV in  $O_2$ -saturated  $PYR_{1(201)}TFSI$  with 0.1 M LiTFSI at 30 °C, shows that the presence of lithium salt brings to disappearance of the oxidation peak which in absence of  $Li^+$  was ascribed to superoxide oxidation. Such peak is replaced by a broader signal displaced toward more positive potentials by about 1 V (peak II). The peak at ca. 3.7 V observed in Figure 4.1.2c is still present in Figure 4.1.11a (peak III).

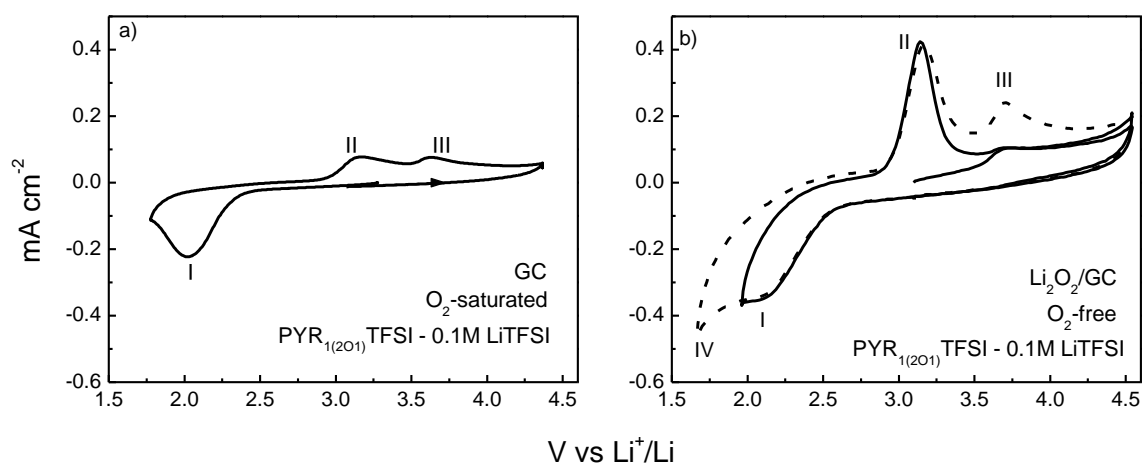
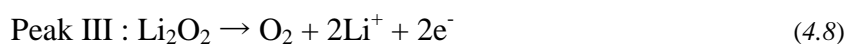


**Figure 4.1.11:** CVs at 20  $mV s^{-1}$  and 30 °C in  $PYR_{1(201)}TFSI$  of (a) GC in  $O_2$ -saturated solution without and with 0.1 m LiTFSI and (b)  $Li_2O_2$  coated GC in  $O_2$ -free 0.1 M LiTFSI solution [adapted from Ref. 4.1].

In order to understand the nature of such peaks, CVs with a GC electrode coated with  $Li_2O_2$  powder were performed in  $O_2$ -free  $PYR_{1(201)}TFSI$ -0.1 M LiTFSI and the results are reported in Figure 4.1.11b. The first CV was carried out from 3.0 V toward 4.5 V, back to 2.0 V and forward to 4.5 V vs.  $Li^+/Li$ ; the first scan (3.0 - 4.5 V vs.  $Li^+/Li$ ) featured a small anodic peak (peak III) related to peroxide oxidation:



and the oxygen generated by  $\text{Li}_2\text{O}_2$  oxidation is reduced in the backward sweep (4.5 V - 2.0 V vs.  $\text{Li}^+/\text{Li}$ ) to give the same cathodic peak I, already observed with uncoated GC in  $\text{O}_2$ -saturated  $\text{PYR}_{1(2\text{O}1)}\text{TFSI}$ -0.1 M  $\text{LiTFSI}$  (Figure 4.1.11a).



The last anodic scan from 2.0 V to 4.5 V vs.  $\text{Li}^+/\text{Li}$  features the novel peak II anticipating peak III and it was attributed to the oxidation of lithium superoxide which is more easy to be oxidized than lithium peroxide. The peak III, related to  $\text{Li}_2\text{O}_2$  oxidation, becomes more pronounced in the second CV of Figure 4.1.11b (dashed line) that was carried out between 4.5 V and 1.7 V vs.  $\text{Li}^+/\text{Li}$  to include the cathodic process IV. Hence, presumably, at the lowest potentials lithium peroxide formation takes place. These considerations are in agreement with Refs. [4.19, 4.20]; however, for unambiguous attribution of CV peaks *in-situ* spectroscopic studies should be performed.

Figure 4.1.12 compares the CVs at 30 °C and 60 °C of  $\text{PYR}_{14}\text{TFSI}$ ,  $\text{PYR}_{14}\text{BETI}$  and  $\text{PYR}_{14}\text{IM}_{14}$  with 0.1 M  $\text{LiTFSI}$  and shows that the  $\text{PYR}_{14}$ -based series of ILs feature almost the same behavior than  $\text{PYR}_{1(2\text{O}1)}\text{TFSI}$  after the addition of lithium salt. Formation of solid products was evidenced by passivation of electrodes: careful cleaning of the GC was required in order to obtain reproducibility of CVs.

Table 4.1.4 reports the current density and potential of the reduction peak I ( $E_{\text{pI}}$ ), the potential of the oxidation peak II ( $E_{\text{pII}}$ ) and total charge involved in the reduction ( $Q_{\text{R}}$ ) and oxidation ( $Q_{\text{O}}$ ) processes at different scan rates. At a given temperature, the  $E_{\text{pI}}$  lower and peaks I broaden with the increase of IL viscosity values, i.e. in the order  $\text{PYR}_{14}\text{TFSI} < \text{PYR}_{14}\text{BETI} < \text{PYR}_{14}\text{IM}_{14}$ , and peaks II are not affected by IL nature. This may support the idea that the first reduction of  $\text{O}_2$  is governed by the properties of the solution and that the re-oxidation process is mainly affected by the electronic properties of the insoluble species on the electrode. Also the temperature increase from 30 °C to 60 °C seems to affect only the peaks I that narrow and shift toward positive values, lowering the difference ( $E_{\text{pI}} - E_{\text{pII}}$ ). The  $E_{\text{pI}}$  values are shifted at more positive potentials than those observed in absence of lithium salt (compare data in Table 4.1.4 and Table 4.1.1) because they are related to an electrochemical process followed by a chemical one involving  $\text{Li}^+$ .

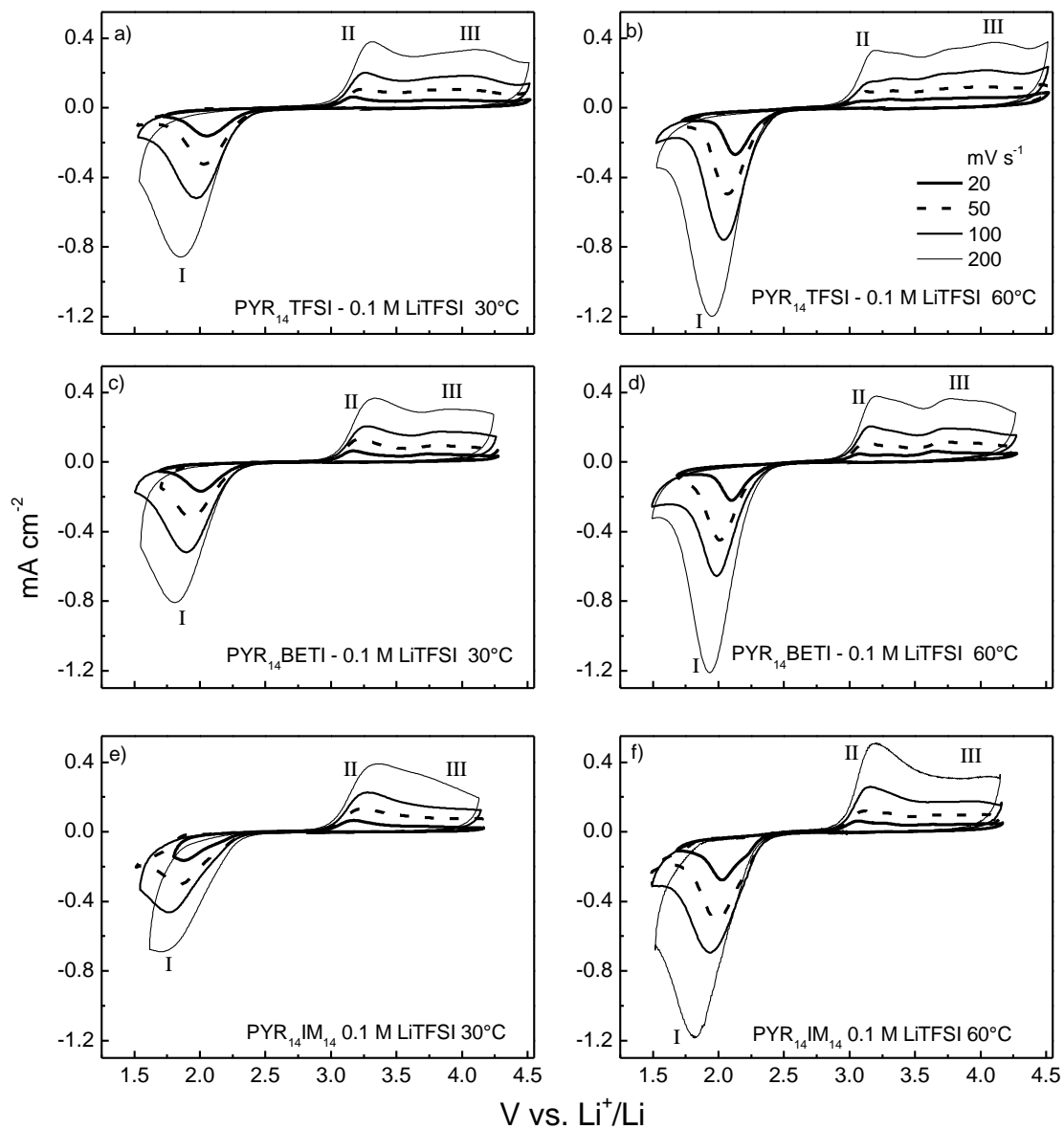


**Figure 4.1.12:** GC CVs at 30 °C and 60 °C in O<sub>2</sub>-saturated PYR<sub>14</sub>TFSI, PYR<sub>14</sub>BETI and PYR<sub>14</sub>IM<sub>14</sub> with 0.1M LiTFSI at different scan rates (20, 50, 100, 200 mV s<sup>-1</sup>) [adapted from Ref. 4.1].

**Table 4.1.4:** Current density ( $i_{pI}$ ) and potential ( $E_{pI}$ ) of the reduction peak I, potential of the oxidation peak II ( $E_{pII}$ ) and total charge involved in the reduction ( $Q_R$ ) and oxidation ( $Q_O$ ) processes at different scan rates ( $v$ ) from GC CVs in  $O_2$ -saturated IL-0.1M LiTFSI solutions.

IL	T °C	v mV s <sup>-1</sup>	$i_{pI}$ mA cm <sup>-2</sup>	$E_{pI}$ V vs. Li <sup>+</sup> /Li	$E_{pII}$ V vs. Li <sup>+</sup> /Li	$Q_R$ mC cm <sup>-2</sup>	$Q_O$ mC cm <sup>-2</sup>
PYR <sub>14</sub> TFSI	30	10	0.10	2.06	3.16	6.3	4.8
		20	0.15	2.05	3.17	3.9	3.6
		50	0.31	2.04	3.23	3.4	3.0
		100	0.50	1.98	3.26	2.9	2.6
		200	0.83	1.85	3.31	2.6	1.4
	60	10	0.15	2.17	3.04	7.1	5.9
		20	0.25	2.13	3.08	5.9	5.0
		50	0.48	2.08	3.12	4.1	3.7
		100	0.74	2.04	3.15	3.8	3.2
		200	1.17	1.95	3.17	3.2	2.7
PYR <sub>14</sub> BETI	30	10	0.10	2.07	3.23	4.5	3.6
		20	0.17	2.01	3.17	3.7	3.0
		50	0.32	1.93	3.21	2.9	2.4
		100	0.51	1.89	3.27	2.8	2.2
		200	0.81	1.81	3.34	2.4	2.0
	60	10	0.16	2.13	3.04	6.8	4.5
		20	0.21	2.10	3.07	5.0	3.7
		50	0.43	2.01	3.10	3.6	2.8
		100	0.64	1.99	3.15	3.5	2.6
		200	1.19	1.93	3.18	3.0	2.3
PYR <sub>14</sub> IM <sub>14</sub>	30	10	0.09	1.99	3.14	4.8	2.5
		20	0.16	1.88	3.17	3.1	2.1
		50	0.29	1.85	3.24	3.9	2.1
		100	0.46	1.76	3.27	2.9	1.8
		200	0.66	1.71	3.37	2.2	1.7
	60	10	0.17	2.08	3.02	8.2	3.5
		20	0.27	2.03	3.05	6.1	3.6
		50	0.49	1.99	3.11	5.5	2.5
		100	0.67	1.94	3.16	3.9	2.4
		200	1.15	1.82	3.21	3.5	2.3

To better highlight the effect of  $\text{Li}^+$  on ORR, Figure 4.1.13 compares the magnifications of the CVs in the  $\text{PYR}_{14}$ -based ILs with and without LiTFSI in the 2.75-1.5 V vs.  $\text{Li}^+/\text{Li}$  range at two selected scan rates.

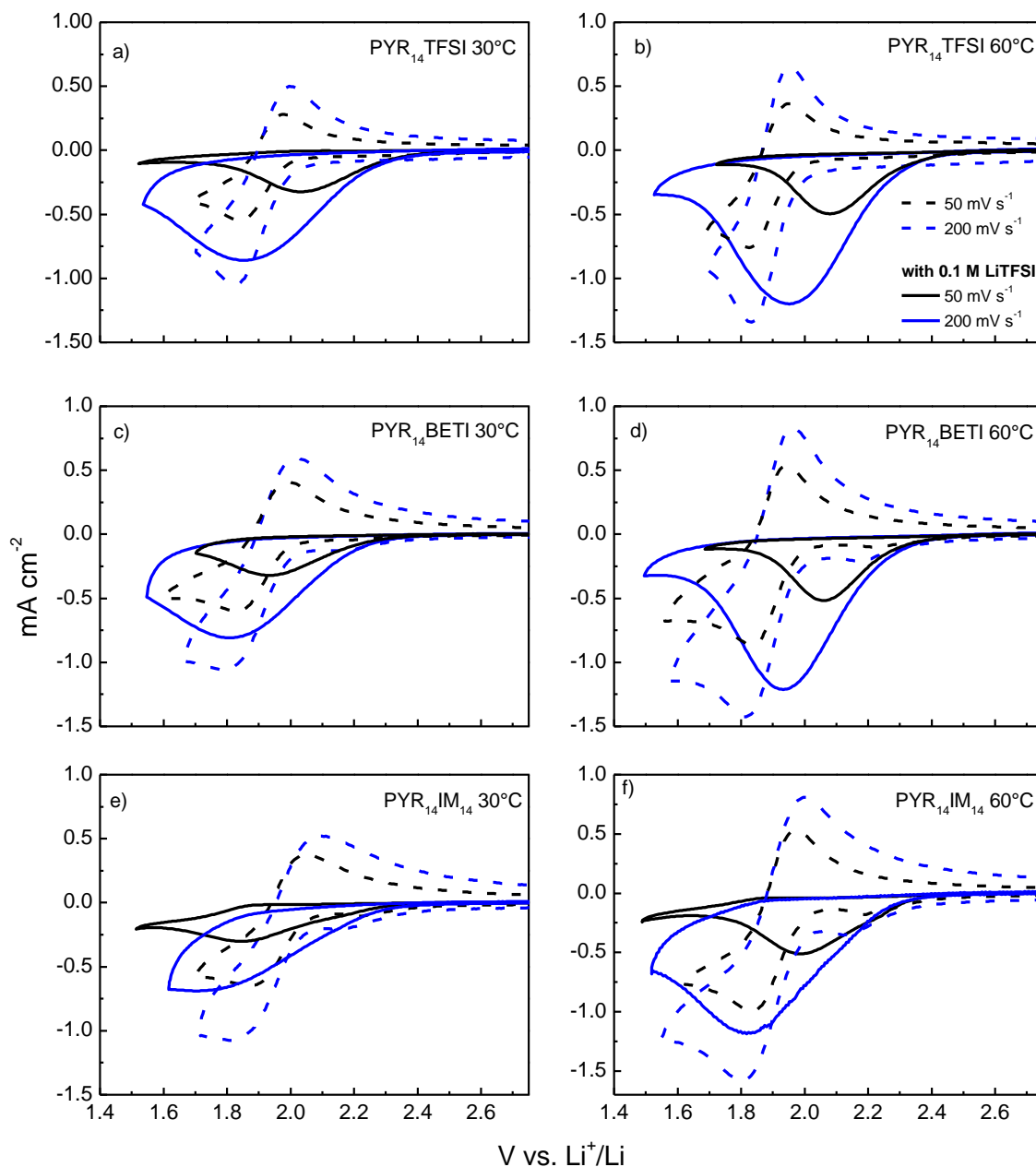


**Figure 4.1.13:** GC CVs in  $\text{O}_2$ -saturated PYRILs with 0.1 M LiTFSI (solid lines) and without lithium salt (dashed lines) at  $50 \text{ mV s}^{-1}$  (black curves) and  $200 \text{ mV s}^{-1}$  (blue curves), at  $30 \text{ }^\circ\text{C}$  and  $60 \text{ }^\circ\text{C}$  [adapted from Ref. 4.1].

The effect of lithium salt addition on the  $O_2$  reduction peak potential and current is less pronounced at  $200 \text{ mV s}^{-1}$  than at  $50 \text{ mV s}^{-1}$ . This is probably due to the time scale of the reaction of the  $O_2^{\cdot -}$  with  $Li^+$  which can appear “slow” with respect to time scale of the experiment run at  $200 \text{ mV s}^{-1}$ . Consequently, formation of passivating products is less pronounced and, then, cathodic peak is both less anticipated and lowered at the faster sweep than at the slowest one. At  $60 \text{ }^\circ\text{C}$ , the gap between the CV data without and with LiTFSI seems to increase because at such temperature the chemical reaction is accelerated and appears “fast” with respect to the CV time scale.

In Table 4.1.4, the charge involved in the cathodic and anodic CV scans are not very different, hence the ORR processes in  $PYR_{14}$ -based ILs with LiTFSI have good recharge efficiencies, at least in the time scale of the CV experiments, and this is a good starting point toward the development of IL-based lithium/oxygen batteries. However, the stability of ILs in presence of products of high reactivity, like peroxides, should be proved upon the long time scale of the galvanostatic discharge/charge cycles of the battery. Given that some studies on the ORR in ether-based solvents, indicated that the ether chain is labile in presence of the superoxide anion [4.21], the use of  $PYR_{1(2O1)}TFSI$  in lithium/oxygen battery has not been further investigated.

### 4.1.3 Summary of ORR basic aspects in IL-based electrolytes

The voltammetric study of ORR in IL without lithium salt reveals that the first step which involves superoxide formation is a quasi-reversible electrochemical process. Quasi-reversibility implies that closed-form solutions are not viable for CV analysis. Hence, Nicholson and Matsuyama and Ayabe working functions have been used to evaluate such parameters like  $D_O$  and  $C_O$  (by combining UGC findings),  $\alpha$ ,  $E_{1/2}$  and  $k^\circ$ .

The study shows that the  $D_O$  values decrease with the increase of IL viscosity and that oxygen solubility is promoted by fluorine content in the IL anion. For each IL the temperature rise does not significantly alter  $C_O$  and has the major effect on oxygen diffusion which roughly doubles moving from  $30 \text{ }^\circ\text{C}$  up to  $60 \text{ }^\circ\text{C}$ . The charge of the superoxide anion causes that its  $D_R$  diffusion coefficient is much lower than  $D_O$ . The value of  $D_O/D_R$  affects the values of both the heterogeneous rate constants  $k^\circ$  and the formal

potential  $E^{\circ'}$ . The  $k^{\circ}$  data reported are in the order of  $10^{-3} \text{ cm s}^{-1}$  when calculated with the approximation of  $D_{\text{O}}/D_{\text{R}} = 60$  and only double when such ratio is set to 2. If the highest  $D_{\text{O}}/D_{\text{R}}$  ratio is considered, then  $E^{\circ'}$  would differ from the experimental  $E_{1/2}$  by c.a. 50 mV at maximum, and be of c.a. 2.2 V vs.  $\text{Li}^+/\text{Li}$ .

The presence of lithium ions causes chemical reactions following the first electrochemical step of superoxide formation that even yield insoluble products on the electrode surface. Such reactions anticipate the voltammetric peak and lower the cathodic currents with a different impact on the CV depending on the scan rates, and will also have a role in the galvanostatic discharge/charge response of an IL-based lithium/oxygen battery. Porous electrodes would buffer the electrode passivation effects caused by the presence of lithium ions and could even modify the rate of the electron transfer process by the inherent electronic and surface chemistry properties of carbon.

As it concerns the re-oxidation processes in IL-LiTFSI, it involves both lithium superoxide ( $\text{LiO}_2$ ) and lithium peroxide ( $\text{Li}_2\text{O}_2$ ) and take place below 4 V vs.  $\text{Li}^+/\text{Li}$ , which would mark the upper limit of the galvanostatic charge of an IL-based lithium/oxygen battery. Finally, in view of the development of such kind of batteries, the rate of the process occurring at the lithium anode has to be considered. Indeed, the  $k^{\circ}$  for this process and the lithium diffusion coefficients in pyrrolidinium-based ILs are more than one order of magnitude lower than the data here reported for the ORR at the battery cathode [4.22]. Hence, efforts should be devoted to improve the kinetics at the anode side as well as to evaluate the rate of oxygen solubility in IL which is a crucial parameter affecting the battery capacity particularly at high discharge currents.

## 4.2 Synthesis and characterization of porous carbons as cathode materials for high capacity Li/O<sub>2</sub> batteries

According to literature [4.23, 4.24], carbon electrode for ORR should feature high meso-macroporous specific volume in order to host high amounts of Li<sub>2</sub>O<sub>2</sub> or Li<sub>2</sub>O formed during the cell discharge. These species may clog the cathode reactive sites, and, hence, limits the cell discharge capacity. Also carbon surface chemistry, including carbon doping with heteroatoms like nitrogen or boron, has been demonstrated to be crucial for ORR [4.23-4.29]. Literature reports that a wide range of carbons and carbon/catalyst systems are under study in order to find the best cathode material for ORR. SuperP carbon (ERCHEM), among the tested commercial carbons, is one of the best performing and this seems related to the presence of 50 nm interstitial pores. Carbons with bimodal pore distribution, where the ORR redox process takes place in catalyzed pores and non catalyzed large pores account for O<sub>2</sub> diffusion, have also been proposed [4.30]. Inorganic catalytic systems typically supported or mixed with carbons, were widely used; for example manganese dioxide-coated aerogel carbons were proposed, showing that the discharge capacity increases when pore size increased from 6 to 15 nm and when the volume of these pores increased [4.31]. However the catalyst role in ORR is still unclear [4.24, 4.32, 4.33]. From the data available in literature it is possible to conclude that the specific capacity of Li/O<sub>2</sub> batteries is notably affected by cathode composition and is related to carbon specific pore volume and pore size and is not much affected by carbon specific surface area.

In this PhD work different porous carbons, even with heteroatoms as N and B were synthesized and characterized by porosity and structural analyses (Sections 4.2.1 and 4.2.2). The electrochemical behaviour toward ORR in IL-based electrolyte was evaluated (Section 4.2.3) also in comparison with the other carbons as well as carbon/catalyst systems (Sections 4.2.4 and 4.2.5) provided by the group of Kiev University, partner of European project LABOHR. The electrochemical experiments were carried out in PYR<sub>14</sub>TFSI-based electrolyte.

### 4.2.1 Syntheses of novel carbon architectures by disordered template method

Synthesis by template methods enables a fine control over the organization of the porous electrode network, which mainly depends on the template structure, allowing the introduction of changes in composition by the use of different carbon precursors, without major variations of the morphology.

The synthetic route adopted to obtain the different porous carbons implied simple, low-cost sol-gel methods using resorcinol (R) - formaldehyde (F) resin as carbon precursor and disordered commercial colloidal silica as template [4.34, 4.35].

The gel formation is a consequence of resorcinol and formaldehyde endothermic polymerisation and the structure and properties of the resin strongly depend on the working conditions. The polycondensation between R and F, proceeds via addition reaction followed by a condensation reaction leading methylene and methylene ether bridges. The heating conditions, as well as the pH of the R-F solution are key factors that influenced the final carbon porosity [4.36], using colloidal silica as template agent the carbon porosity is mainly related to the silica particles size, allowing easier control of the working condition and synthesis reproducibility.

Table 4.2.1 reports the silica size and content, dispersing media, pH of the colloidal silicas used for carbons synthesis and the code of the obtained carbons. Mesoporous carbons doped with nitrogen (NZL) or boron (BZL) were also prepared, melamine and boric acid were selected as N and B precursors. N-doping was performed on the basis of literature data which indicate that nitrogen promotes 4-electron  $O_2$  reduction. B-doping was carried out in order to promote a Lewis acidic behavior of the carbon, that in turn may enhance superoxide adsorption and disproportionation with positive effect on oxygen reduction potential.

**Table 4.2.1:** Code, size, content, dispersing media and pH of the commercial colloidal silicas used as template, last column reports the code of the disordered meso-macroporous carbons.

Producer	Code	SiO <sub>2</sub> size nm	SiO <sub>2</sub> % wt.	Media	pH	Carbon code
LUDOX Sigma Aldrich	LUDOX TM-40	22	40%	water	9.8	TMb
NYACOL NANO TECHNOLOGIES, Inc.	NYACOL DP 5480	50	30%	ethylene glycol	3 in H <sub>2</sub> O	NY
NISSAN CHEMICAL INDUSTRIES ,Ltd.	SNOWTEX ZL	70-100	40.6	water	9.3	ZL NZL BZL

For the synthesis of non-doped carbons, resorcinol was completely dissolved in the aqueous formaldehyde solution with a R/F molar ratio = 0.5 and then, silica was added. The mixture was aged at 80-90 °C for few days.

For the N-doped carbon synthesis, melamine was dissolved in 500 mL of water at 100 °C for the low solubility of the base. Then, resorcinol was dissolved in the melamine solution and Silica added. Formaldehyde was added and the pH was adjusted to 8-9 by NH<sub>4</sub>OH (30%). The solution was concentrated up to a volume of ca. 450 mL and then heated in close vessels at 90°C. After 4 days two phases were formed: one light brown in the bottom of the vessel and one white in the upper part. In order to dry the gel the vessels were further heated for one day at 90°C with open plugs.

For the B-doped carbon synthesis, boric acid was completely dissolved in the aqueous formaldehyde solution and resorcinol-silica suspension was added, pH was 5 and was not adjusted to higher values. The gel was aged in closed vessels at 85°C over few days.

Each dry gel was pyrolysed at 900 °C for 2 h (10 °C min<sup>-1</sup>), under Ar flow (200 mL min<sup>-1</sup>). The pyrolysed powder was milled at 250 rpm in tungsten carbide jar with tungsten spheres: 2 minutes with 4 spheres with Ø = 2 cm, followed by 5 minutes with 11 additional spheres with Ø = 1 cm. The silica template was removed by stirring the powder in boiling 6 M NaOH hydroalcoholic solution (50 vol % ethanol-50 vol % H<sub>2</sub>O) twice (250 mL each) up to complete evaporation of the solution. The first washing step was performed by wetting the SiO<sub>2</sub>-C under vacuum. After each NaOH treatment the carbon was washed with MilliQ water using Ederol filters with 8-12 µm pores. Then, the carbon was rinsed with H<sub>2</sub>O/ethanol and with acetone and, finally dried at 60 °C over night. The residual

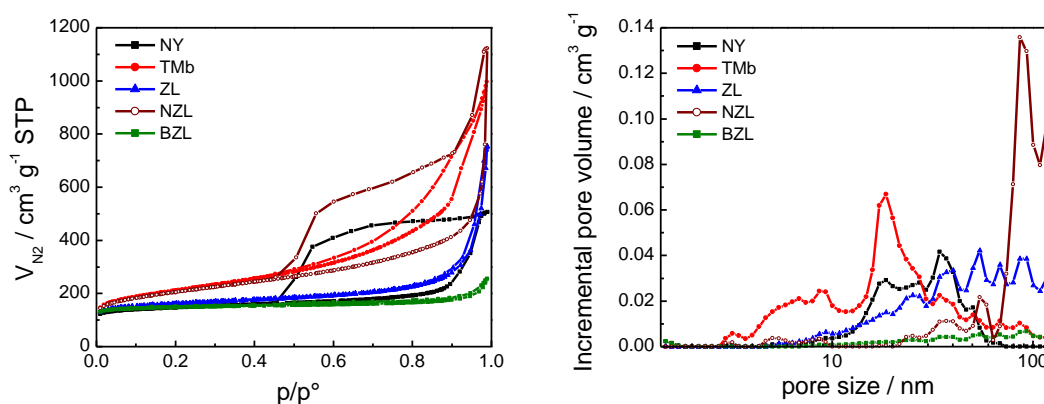
SiO<sub>2</sub> was checked by TGA with a ramp of 20 °C min<sup>-1</sup> up to 950 °C under O<sub>2</sub> flow. The BZL required a stronger NaOH and washing treatments in order to remove silica and NaOH. Table 4.2.2 summarizes the R/F gel composition, the amount of carbon obtained in each batch and the ash content, corresponding to residual SiO<sub>2</sub>.

**Table 4.2.2:** Composition of the gel, carbon mass and SiO<sub>2</sub> residual in the synthesized template carbons.

Carbon	Gel composition					Carbon mass g	SiO <sub>2</sub> residual %
	Silica mol	R mol	F mol	N- or B- precursor mol	H <sub>2</sub> O mol		
TMb	1.8	0.2	0.4		10.4	3.4	2.9
NY	0.4	0.2	0.4		1.5	17.1	--
ZL	0.4	0.2	0.4		3.1	14.1	2.1
NZL	0.4	0.04	0.4	0.16	>3.1	6.0	3.3
BZL	0.14	0.07	0.14	0.015	1.1	5.4	2.1

#### 4.2.2 Porosity analysis of disordered template carbons

The porosity of the template carbons was evaluated by an ASAP 2020 system (Micromeritics) which collects the nitrogen adsorption isotherms at 77 K; the carbon samples were dried for at least 2 h at 120 °C before testing. Figure 4.2.1 shows the N<sub>2</sub>-adsorption/desorption isotherm and the incremental pore volume distribution evaluated by the Density Functional Theory analysis (DFT) of template carbons.



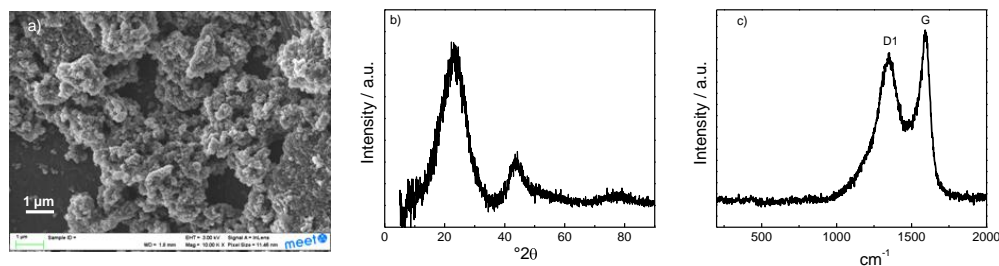
**Figure 4.2.1:** N<sub>2</sub>-adsorption/desorption isotherm (a) and incremental pore volume distribution (b) of the synthesized template carbons.

Table 4.2.3 reports, for the synthesized carbons, the total specific surface area ( $S_{BET}$ ) evaluated by B.E.T. theory and main pore size ( $d$ ), specific microporous volume ( $V_{< 2 \text{ nm}}$ ), specific volume ( $V_{2-100 \text{ nm}}$ ) and specific area ( $A_{2-100 \text{ nm}}$ ) from pores with diameters between 2 nm and 100 nm evaluated by DFT analysis with the assumption of a cylindrical pore geometry.

**Table 4.2.3:** Results of porosity analysis of template mesoporous carbons

Carbon	$S_{BET}$ $\text{m}^2 \text{g}^{-1}$	$d$ nm	$V_{< 2 \text{ nm}}$ $\text{cm}^3 \text{g}^{-1}$	$V_{2-100 \text{ nm}}$ $\text{cm}^3 \text{g}^{-1}$	$A_{2-100 \text{ nm}}$ $\text{m}^2 \text{g}^{-1}$
TMb	740	18	0.12	0.91	276
NY	565	34	0.15	0.51	89
ZL	610	54	0.16	0.73	94
NZL	715	90	0.12	0.62	55
BZL	583	90	0.18	0.10	12

As previously discussed the discharge capacity of cathode is related to carbon specific pore volume and pore size. A high specific meso-macroporous volume of the carbon favors cathode capacity because it makes it possible to host high amounts of insoluble discharge products. ZL carbon featured the most promising porosity compared to the other synthesized carbons and was selected for further studies. As reported in Table 4.2.3, ZL showed a pore size distribution centered at 54 nm and a  $V_{2-100 \text{ nm}}$  of  $0.73 \text{ cm}^3 \text{g}^{-1}$ , porosity in the macropore domain was evinced by the SEM image reported in Figure 4.2.2a. XRD (Figure 4.2.2b) and Raman (Figure 4.2.2c) analyses indicated that ZL is a carbon made of small graphitic domains of ca. 2 graphene layers 2.5 nm wide. The  $I_{D1}/I_G$  height ratio of the Raman bands D1 attributed to graphene layer edges and G, corresponding to the in-plane vibrational mode of surface graphene layers, is 1.7.



**Figure 4.2.2:** SEM image (a), XRD pattern (b) and Raman spectra (c) of ZL carbon powder [adapted from Ref. 4.2].

### 4.2.3 Electrochemical characterization of meso-macro porous ZL carbon in O<sub>2</sub>-saturated PYR<sub>14</sub>TFSI - 0.1 M LiTFSI

The electrochemical characterization of ZL carbon was carried out in the conventional 3-electrode cell described in Section 2.2.3 (Figure 2.3a). Figure 4.2.3 shows the voltammetric response of bare (GC) and ZL-coated (ZL/GC) glassy carbon electrodes in O<sub>2</sub>-saturated PYR<sub>14</sub>TFSI - 0.1 M LiTFSI, at 20 mV s<sup>-1</sup> and 30 °C. The ZL/GC cyclic voltammetry of Figure 4.2.3 is reported subtracted by the capacitive background current in order to define better the voltammetric pecks.

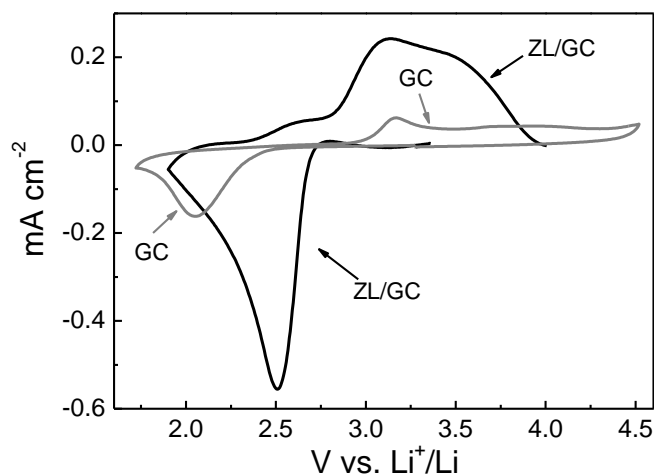
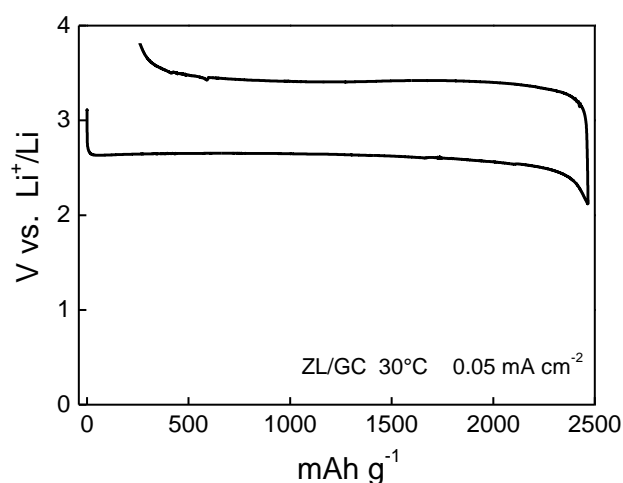


**Figure 4.2.3:** CVs at 20 mV s<sup>-1</sup> and 30 °C of bare (GC) and ZL-coated (ZL/GC, 0.5 mg cm<sup>-2</sup> of ZL, subtracted by capacitive background current) glassy carbon electrodes in O<sub>2</sub>-saturated PYR<sub>14</sub>TFSI - 0.1 M LiTFSI.

The voltammetric reduction peak at the bare GC at 2.05 V vs. Li<sup>+</sup>/Li is related to the oxygen reduction to superoxide that because of the presence of lithium ions further reacts to give insoluble products on the electrode surface. These products are, then, oxidized in the back anodic scan featuring a narrow peak at 3.17 V vs. Li<sup>+</sup>/Li and a broader one in the 3.5-4.3 V vs. Li<sup>+</sup>/Li region [4.10, 4.19]. The oxygen reduction charge for the CV reported in Figure 4.2.3 at GC electrode is 3.9 mC cm<sup>-2</sup>, and the efficiency of the recharge process, calculated on the entire anodic scan, is 92%, a high value that is achievable thanks

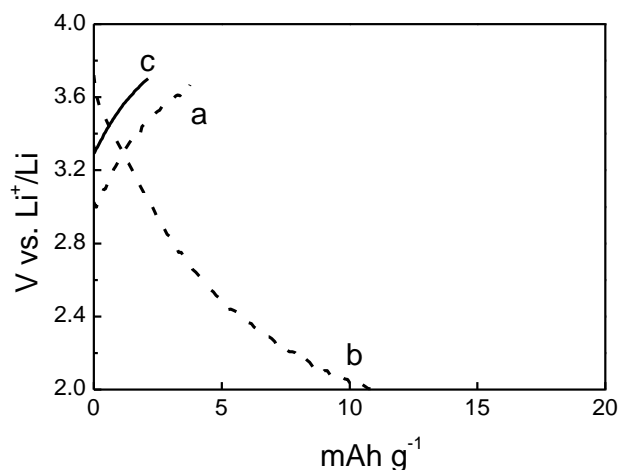
to the wide electrochemical stability window of the IL. The CV at the ZL/GC electrode, free from any additional catalyst, features the oxygen reduction peak at 2.5 V vs.  $\text{Li}^+/\text{Li}$  which is positively shifted by c.a. 500 mV with respect to the value found for bare GC. This significant potential shift can be related to the porous carbon nanotexture since ZL is a low graphitic carbon with a high number of exposed graphene edges that favor  $\text{O}_2$ -adsorption and reduction. Furthermore, a large 3.0-3.9 V vs.  $\text{Li}^+/\text{Li}$  reoxidation region appears which corresponds to the overlapping of the two anodic peaks observed at the GC electrode. The high surface area of the ZL carbon accounts for voltammetric current densities that are much higher than those observed with the bare GC. The oxygen reduction charge at this electrode is  $45 \text{ mC cm}^{-2}$  with a recharge efficiency of 97%. These results indicate that the nature of the ZL carbon electrode notably influences ORR and should be beneficial for the discharge/charge potentials and capacity of the  $\text{Li}/\text{O}_2$  battery cathode. This is further demonstrated by the galvanostatic studies.

Figure 4.2.4 reports the voltage profile of the catalyst-free ZL/GC electrode upon galvanostatic discharge/charge at  $0.05 \text{ mA cm}^{-2}$  and  $30 \text{ }^\circ\text{C}$  with 2.0 and 3.8 V vs.  $\text{Li}^+/\text{Li}$  voltage cut-off, the discharge capacity is c.a.  $2500 \text{ mAh g}^{-1}$ .



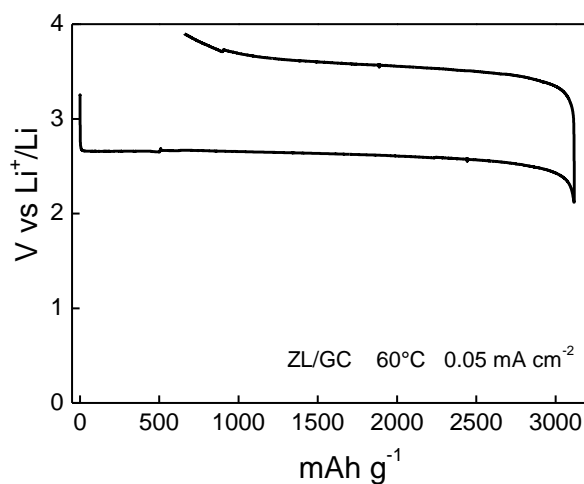
**Figure 4.2.4:** Voltage profiles upon galvanostatic discharge/charge of the ZL/GC electrode ( $0.5 \text{ mg cm}^{-2}$  of ZL carbon) at  $0.05 \text{ mA cm}^{-2}$  and  $30 \text{ }^\circ\text{C}$  in  $\text{O}_2$ -saturated  $\text{PYR}_{14}\text{TFSI} - 0.1 \text{ M LiTFSI}$  [adapted from Ref. 4.2].

The sharp variation of the voltage profiles clearly indicates the end of the oxygen electrode discharge and recharge processes. Upon discharge, the active area of the ZL/GC electrode is progressively clogged by insoluble oxygen reduction species and at the end of discharge the overvoltage abruptly increases. The recharge ends when the insoluble species are reoxidized and the electrode active area is recovered. In agreement with the voltammetric results, the electrode discharge takes place at 2.65 V vs.  $\text{Li}^+/\text{Li}$ . The recharge is at 3.4 V vs.  $\text{Li}^+/\text{Li}$ , well below the anodic stability limit of the  $\text{PYR}_{14}\text{TFSI}$ -based electrolyte (4.5 V vs.  $\text{Li}^+/\text{Li}$ , at ZL electrode). The flat charge plateau indicates that only one species is involved, presumably  $\text{Li}_2\text{O}_2$ . Indeed, superoxide oxidation is not detectable because the discharge reported in Figure 4.2.3a lasts c.a. 24 hours, and hence any produced  $\text{LiO}_2$  has time to completely disproportionate to  $\text{Li}_2\text{O}_2$  [4.20]. The recharge takes place at potentials that are lower than those reported in literature thus far for  $\text{Li}/\text{O}_2$  cathodes working with organic or IL-based electrolytes [4.24, 4.33, 4.37-4.39]. The low charge voltage makes it possible to achieve a recharge efficiency ( $\eta$ ) of 90%, which is one of the highest value reported up to now for discharge/charge cycles not limited by time; the charge was stopped when the electrode potential abruptly increased. No charge plateau was observed when the ZL/GC electrode was polarized up to 3.8 V vs.  $\text{Li}^+/\text{Li}$  without being previously discharged (Figure 4.2.5).



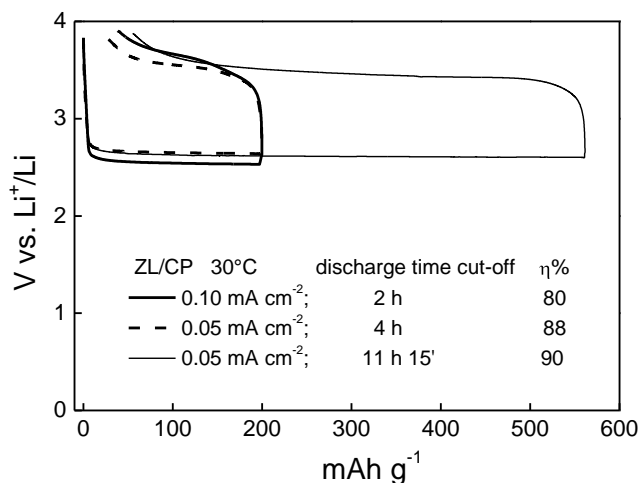
**Figure 4.2.5:** Voltage profile upon galvanostatic cycling at  $0.10 \text{ mA cm}^{-2}$  and  $30 \text{ }^\circ\text{C}$  of the ZL/GC electrode ( $0.5 \text{ mg cm}^{-2}$  of ZL carbon): first charge (a) and discharge (b) in  $\text{O}_2$ -free  $\text{PYR}_{14}\text{TFSI} - 0.1 \text{ M LiTFSI}$  and first charge (c) in  $\text{O}_2$ -saturated electrolyte solution [adapted from Ref. 4.2].

Figure 4.2.6 reports the voltage profile of the ZL/GC electrode upon the galvanostatic discharge/charge at  $0.05 \text{ mA cm}^{-2}$  and  $60 \text{ }^\circ\text{C}$  and demonstrates the viability of the  $\text{PYR}_{14}\text{TFSI}$ -based electrolyte in  $\text{Li}/\text{O}_2$  batteries operating above room temperature, where the use of conventional solvents is critical. The electrode capacity is 25 % higher at  $60 \text{ }^\circ\text{C}$  than at  $30 \text{ }^\circ\text{C}$ , presumably because of the higher solubility of  $\text{Li}_2\text{O}_2$  and  $\text{O}_2$  diffusion coefficient at the higher temperature, and  $\eta$  is c.a. 80% at  $60 \text{ }^\circ\text{C}$ .



**Figure 4.2.6:** Voltage profiles upon galvanostatic discharge/charge of the ZL/GC electrode ( $0.5 \text{ mg cm}^{-2}$  of ZL carbon) at  $0.05 \text{ mA cm}^{-2}$  and  $60 \text{ }^\circ\text{C}$  in  $\text{O}_2$ -saturated  $\text{PYR}_{14}\text{TFSI} - 0.1 \text{ M LiTFSI}$  [adapted from Ref. 4.2].

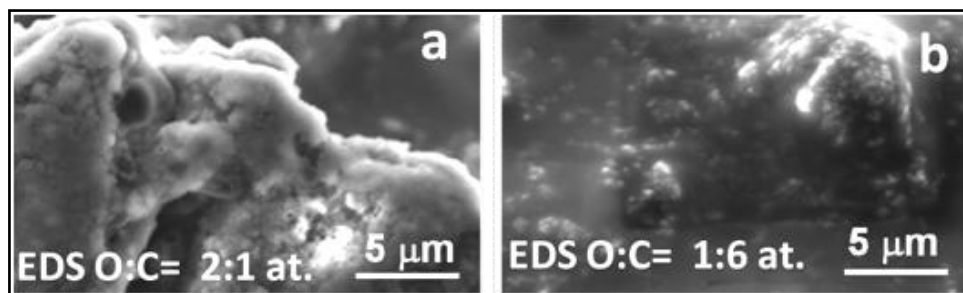
Figure 4.2.7 gives the voltage profiles of ZL-coated carbon paper electrodes (ZL/CP) during cycles that were performed at different discharge time cut-off, at  $30 \text{ }^\circ\text{C}$  and different current densities.



**Figure 4.2.7:** Voltage profiles upon galvanostatic discharge/charge of ZL/CP electrode ( $1.0 \text{ mg cm}^{-2}$  of ZL carbon) at 0.1 and  $0.05 \text{ mA cm}^{-2}$  at  $30^\circ \text{C}$  in  $\text{O}_2$ -saturated  $\text{PYR}_{14}\text{TFSI}$ - $0.1 \text{ M LiTFSI}$  [adapted from Ref. 4.2].

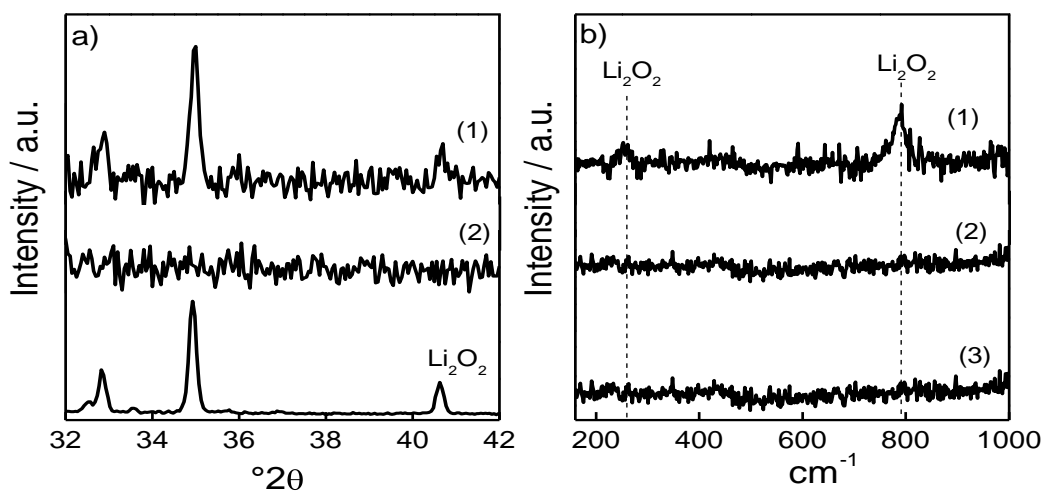
The amount of charge involved in electrode charging seems to be related to that of the discharge step, with a recharge efficiency ( $\eta$ ) as high as 90% for the longest discharge. The fact that the longer the discharge time, the higher is the reoxidation charge suggests that parasitic reactions upon discharge are not very important. Furthermore, the increase of efficiency with depth of discharge can be explained by taking into account that the increase of discharge time should increase peroxide anion concentration and, hence,  $\text{Li}_2\text{O}_2$  solubility should lower. Consequently, more  $\text{Li}_2\text{O}_2$  is formed on the electrode and can be reoxidized in the following charge. The increase of current density from  $0.05$  and  $0.10 \text{ mA cm}^{-2}$  only slightly affects discharge and charge voltage plateau, which respectively lower from  $2.6 \text{ V}$  to  $2.5 \text{ V}$  vs.  $\text{Li}^+/\text{Li}$  and increase from  $3.55 \text{ V}$  up to  $3.65 \text{ V}$  vs.  $\text{Li}^+/\text{Li}$ .

In order to unambiguously ascribe the charge plateau to the reoxidation of oxygen-reduced species formed during discharge, the ZL/CP electrodes were analyzed by SEM-EDS, XRD and Raman spectroscopy. The SEM-EDS analysis reported in Figure 4.2.8 indicates the formation of oxygen-rich products upon electrode discharge; the O to C atomic ratio changed from 2:1 in the discharged electrode to 1:6 in the charged one.



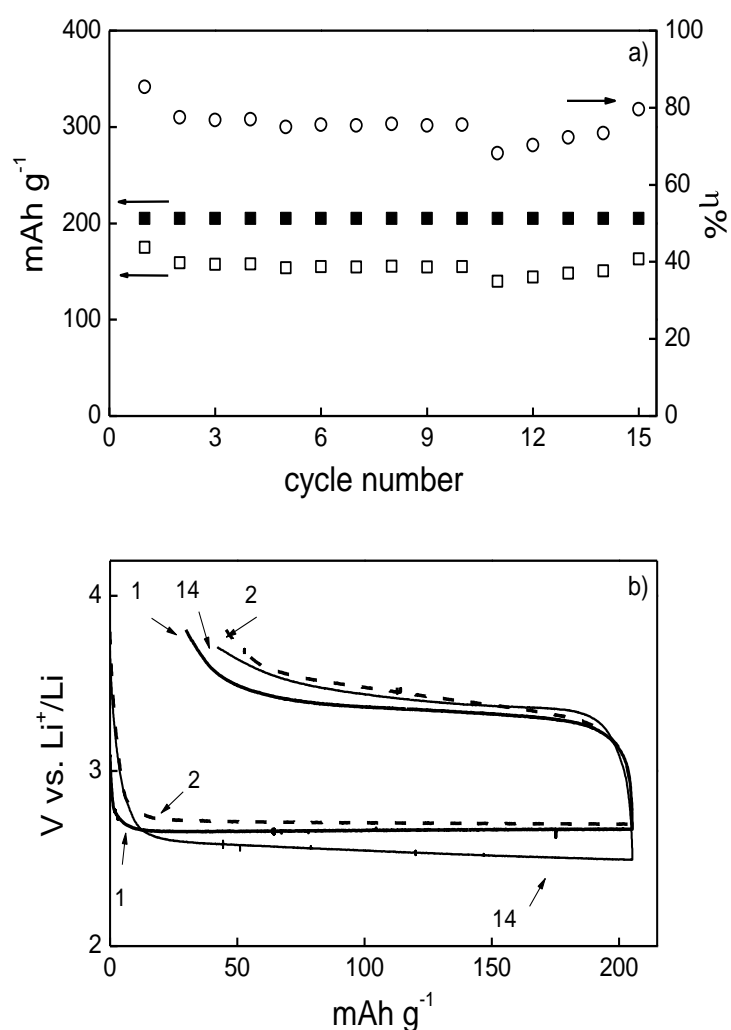
**Figure 4.2.8:** SEM images of the ZL/CP electrodes ( $1.0 \text{ mg cm}^{-2}$  of ZL carbon) cycled at  $0.1 \text{ A g}^{-1}$  after 20 h discharge (a) and after the first recharge (b); the EDS O:C atomic ratio is also reported [adapted from Ref. 4.2].

XRD and Raman spectroscopy patterns in Figure 4.2.9 unambiguously identified such oxygen-based species as  $\text{Li}_2\text{O}_2$ ; no secondary ORR products were detected. XRD analysis of the discharged electrode indicates that  $\text{Li}_2\text{O}_2$  crystallites are 42 nm wide, a size that well fits the ZL carbon pore size. If we take into account that the  $\text{Li}_2\text{O}_2$  density is  $2.3 \text{ g cm}^{-3}$  and the meso-macropore volume of ZL is  $0.73 \text{ cm}^3 \text{ g}^{-1}$ , then 1.7 g of peroxide per gram of carbon are required to clog ZL pores, which corresponds to a charge of ca. 2000 mAh  $\text{g}^{-1}$ , which compares well to the specific capacity data of ZL reported above.



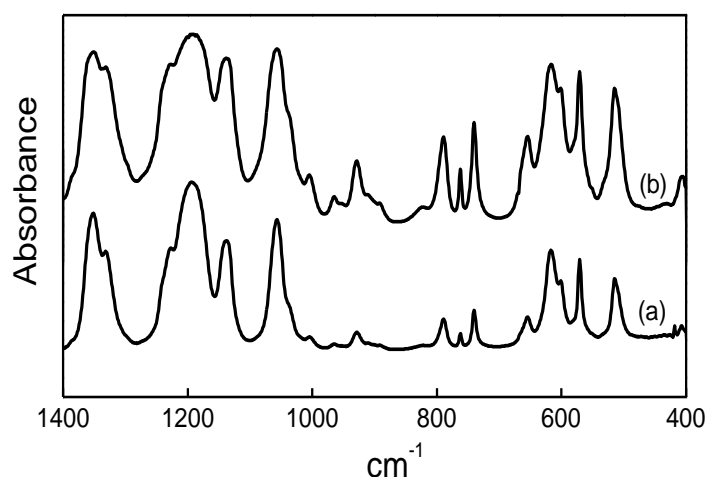
**Figure 4.2.9:** (a) XRD of ZL/CP electrodes ( $1.0 \text{ mg cm}^{-2}$  of ZL carbon) cycled at  $0.1 \text{ A g}^{-1}$  after 20 h-discharge (1) and after the first recharge (2), the pattern of the  $\text{Li}_2\text{O}_2$  powder is also reported; (b) Raman spectra of the fully discharged (1) and charged (2) ZL/CP electrodes and of the ZL carbon powder (3) [adapted from Ref. 4.2].

Figure 4.2.10 reports the trend of the specific discharge and charge capacities and recharge efficiency and of the electrode potential profiles over repeated cycles of a ZL/GC electrode at ca.  $0.08 \text{ mA cm}^{-2}$  with discharge time cut-off of 5 h, corresponding to ca.  $0.4 \text{ mAh cm}^{-2}$  and  $200 \text{ mAh g}^{-1}$ . The recharge was not time limited and, as shown in Figure 4.2.8b, it took place below 3.8 V vs.  $\text{Li}^+/\text{Li}$  in all cycles. The recharge efficiency was c.a. 80% because of the low depth of discharge.



**Figure 4.2.10:** (a) Discharge (■) and charge (□) specific capacities and recharge efficiency (○) and (b) potential profiles over cycling of a ZL/GC electrode (ca.  $2 \text{ mg cm}^{-2}$  of ZL) at  $0.08 \text{ mA cm}^{-2}$  with discharge time cut-off of 5 h and charge potential cut-off of 3.8 V vs.  $\text{Li}^+/\text{Li}$  up to the 10th cycle and 3.7 V vs.  $\text{Li}^+/\text{Li}$  for the following cycles (labels indicate cycle numbers) [adapted from Ref. 4.2].

FTIR spectroscopy was used to test the electrolyte solution before and after cycling and did not reveal any IL-decomposition products; Figure 4.2.11 shows only minor changes in the spectra due to conformational effects and related to the variation of  $\text{Li}^+$  concentration [4.40]. These data indicate a good cycling stability of the ZL carbon in  $\text{PYR}_{14}\text{TFSI}$ -based electrolyte. However, the lithium anode side has to be investigated in order to fully assess a long cycle life of a  $\text{Li}/\text{O}_2$  cell with these cathode and electrolyte.



**Figure 4.2.11:** FTIR spectra of the  $\text{PYR}_{14}\text{TFSI}e0.1 \text{ M LiTFSI}$  solution (a) fresh and (b) after 1 week's cycling [adapted from Ref. 4.2].

#### 4.2.4 Electrochemical characterization of TMb, NZL and BZL template carbons in $\text{O}_2$ -saturated $\text{PYR}_{14}\text{TFSI} - 0.4 \text{ M LiTFSI}$

The electrochemical response of the TMb, NZL, and BZL samples was investigated by galvanostatic measurements with carbon coated glassy carbon electrodes ( $0.5 \text{ mg cm}^{-2}$  or  $1 \text{ mg cm}^{-2}$  of sample). The concentration of LiTFSI salt in the electrolyte was increased from  $0.1 \text{ M}$  to  $0.4 \text{ M}$  to favor  $\text{Li}^+$  transport to electrode. Figure 4.2.12 shows the discharge/charge galvanostatic cycles of TMb, NZL and BZL samples. The measurements were performed at  $30 \text{ }^\circ\text{C}$  with an electrode coating of  $0.5 \text{ mg cm}^{-2}$  for TMb and NZL carbons and  $1 \text{ mg cm}^{-2}$  form BZL, at  $0.1 \text{ mA cm}^{-2}$  with  $2 \text{ V vs Li}^+/\text{Li}$  and  $3.8 \text{ V vs Li}^+/\text{Li}$  as discharge and charge cut-off, respectively. Table 4.2.4 reports the specific discharge capacity, the recharge efficiency ( $\eta$ ) and discharge ( $V_D$ ) and charge ( $V_C$ ) plateau potentials

of the three studied samples. The results obtained for r ZL carbon tested in the same conditions of NZL and TMb are also reported.

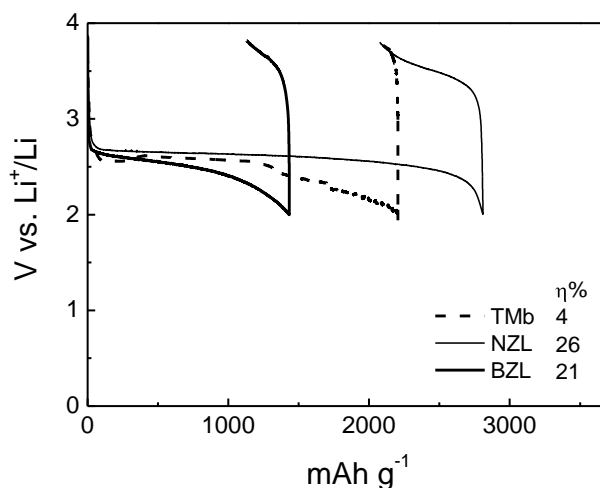


**Figure 4.2.12:** Voltage profiles upon galvanostatic discharge/charge of TMb, NZL and BZL coated GC electrodes at  $0.1 \text{ mA cm}^{-2}$  in  $\text{O}_2$ -saturated  $\text{PYR}_{14}\text{TFSI} - 0.4 \text{ M LiTFSI}$ .

**Table 4.2.4:** Specific discharge capacity ( $\text{mAh g}^{-1}$ ), recharge efficiency ( $\eta$ ), discharge plateau potential ( $V_D$ ) and charge plateau potential ( $V_C$ ) of TMb, NZL, BZL and ZL samples studied in  $\text{O}_2$ -saturated  $\text{PYR}_{14}\text{TFSI} - 0.4 \text{ M LiTFSI}$

Sample	First cycle specific discharge capacity $\text{mAh g}^{-1}$	$\eta$ %	$V_D$ V vs $\text{Li}^+/\text{Li}$	$V_C$ V vs $\text{Li}^+/\text{Li}$
TMb	2210	4	2.6	--
NZL	2805	26	2.6	3.5
BZL	1428	21	2.5	--
ZL	1560	87	2.5	3.5

From Table 4.2.4 it is possible to see that the ZL carbon show the best performance upon the other. NZL carbon gave the best response in terms of specific capacity for the first discharge step but, as BZL and TMb, after the first low-efficiency recharge, cannot be cycled anymore, while ZL carbon coated electrode can be cycled for more than one cycle with efficiency higher than 80 %.

### 4.2.5 Electrochemical characterization of carbon/catalyst systems in O<sub>2</sub>-saturated PYR<sub>14</sub>TFSI - LiTFSI solutions

To evaluate the role of a catalyst on the performance of a carbon-based cathode, the carbon/catalyst systems listed in Table 4.2.5 and provided by the group of Kiev University (partener of European project LABOHR) were tested.

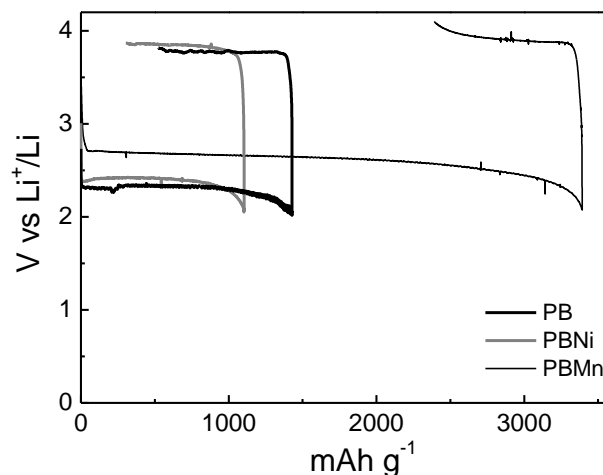
**Table 4.2.5:** Carbon/catalyst system prepared by the group of Prof. Barsukov

Sample Material	Code
5% NiCo <sub>2</sub> O <sub>4</sub> on PureBlack 205 Carbon	PBNi
5% MnO <sub>2</sub> on PureBlack 205 Carbon	PBMn
10% polypyrrole , 5% NiCo <sub>2</sub> O <sub>4</sub> on PureBlack 205 Carbon	PBPyNi
5% NiCo <sub>2</sub> O <sub>4</sub> on ZL Carbon	ZLNi
10% polypyrrole, 5% NiCo <sub>2</sub> O <sub>4</sub> on ZL Carbon	ZLPyNi

The electrochemical response of the PBNi and PBMn was investigated by galvanostatic measurements with carbon coated glassy carbon electrode (0.5 mg cm<sup>-2</sup> of sample). Table 4.2.6 compares the specific discharge capacity, the recharge efficiency ( $\eta$ ) and discharge ( $V_D$ ) and charge ( $V_C$ ) plateau potentials of PBNi and PBMn with that of bare Pure Black 205 (PB) obtained from the first discharge/charge galvanostatic cycle (Figure 4.2.13) performed in O<sub>2</sub>-saturated PYR<sub>14</sub>TFSI-0.4 M LiTFSI at 0.1 mA cm<sup>-2</sup> with 2 V vs Li<sup>+</sup>/Li and 3.9 V vs Li<sup>+</sup>/Li as discharge and charge cut-off, respectively. For PBMn sample the charge cut-off was set at 4.1 V vs Li<sup>+</sup>/Li.

**Table 4.2.6:** First cycle specific discharge capacity (mAh g<sup>-1</sup>), recharge efficiency ( $\eta$ ), discharge plateau potential ( $V_D$ ) and charge plateau potential ( $V_C$ ) of the PB-based carbon/catalyst systems.

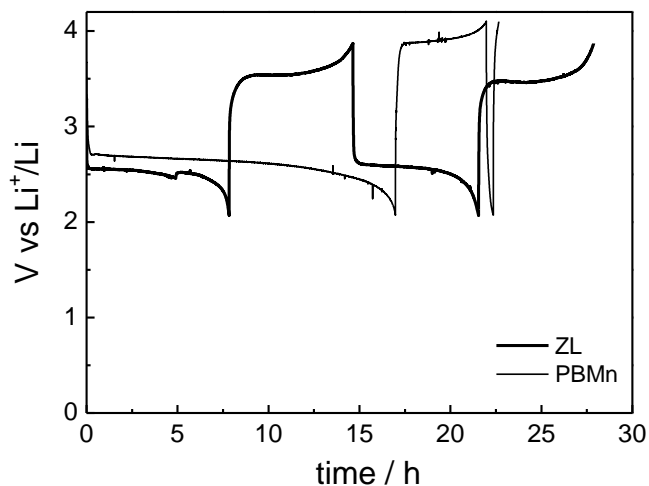
Sample	First cycle specific discharge capacity mAh g <sup>-1</sup>	$\eta$ %	$V_D$ V vs Li <sup>+</sup> /Li	$V_C$ V vs Li <sup>+</sup> /Li
PB	1426	63	2.3	3.8
PBNi	1100	73	2.4	3.9
PBMn	3400	30	2.6	3.9



**Figure 4.2.13:** Voltage profiles upon galvanostatic discharge/charge of the PB, PBNi and PBMn coated GC electrodes ( $0.5 \text{ mg cm}^{-2}$  of carbon) at  $0.1 \text{ mA cm}^{-2}$  and  $30 \text{ }^\circ\text{C}$  in  $\text{O}_2$ -saturated  $\text{PYR}_{14}\text{TFSI} - 0.4 \text{ M LiTFSI}$ .

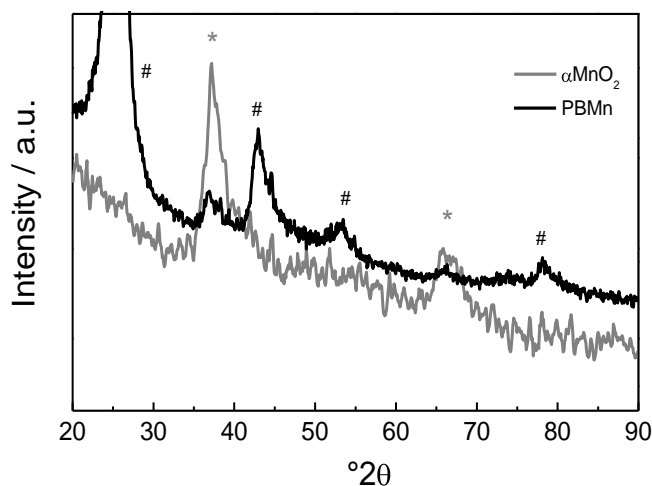
From Table 4.2.6 and Figure 4.2.13 it is possible to see that the presence of  $\text{NiCo}_2\text{O}_4$  does not affect significantly the performance of pristine PureBlack 205 carbon in term of charge and discharge plateau potentials but seems to lower the specific discharge capacity. The sample functionalized with  $\text{MnO}_2$  gives the best response in terms of discharge potential and specific capacity. The latter triplicates with respect to the value featured by PB and PBNi. The galvanostatic cycle performed with PBMn in  $\text{O}_2$ -free electrolyte gives a very low discharge capacity ( $35 \text{ mAh g}^{-1}$ ) with no well defined plateau, confirming that the reduction process in  $\text{O}_2$ -saturated media is due to ORR.

Figure 4.2.14 compares the galvanostatic discharge/charge profiles of the first and the second cycles of PBMn and ZL carbon, tested in the same conditions. The ZL carbon yield a discharge capacity of ca.  $1500 \text{ mAh g}^{-1}$  which is lower than those of PBMn sample, but it shows a less positive recharge plateau potential of  $3.5 \text{ V vs Li}^+/\text{Li}$ . Moreover, while ZL carbon can be undergoes more than one cycle, the PBMn electrode, after the first low-efficiency recharge, cannot be discharged. The PBMn behaviour is similar to what observed for NZL and reported in Section 4.2.4.



**Figure 4.2.14:** Voltage profile upon galvanostatic discharge/charge of the ZL carbon and PBMn coated GC electrodes ( $0.5 \text{ mg cm}^{-2}$  of carbon) at  $0.1 \text{ mA cm}^{-2}$  and  $30 \text{ }^\circ\text{C}$  in  $\text{O}_2$ -saturated  $\text{PYR}_{14}\text{TFSI} - 0.4 \text{ M LiTFSI}$ .

The products of the galvanostatic discharge/charge of the catalytic system PBMn and of the bare PB carbon were evaluated by *ex-situ* XRD analyses. Figure 4.2.15 shows the XRD patterns of the  $\alpha\text{MnO}_2$  and PBMn powders. The spectrum of the PBMn powder shows the reflexes of the manganese oxide (\*) overlapped to those of the PB carbon (#).



**Figure 4.2.15:** XRD patterns of the  $\alpha\text{MnO}_2$  and PBMn powders ( $\Delta 2\theta = 0.067$ ,  $26 \text{ s/step}$ ); the reflexes of the manganese oxide and of the PB carbon are labeled with \* and #, respectively.

In order to evaluate the GLV discharge/charge products, XRD spectra were collected after that the PBm and PB electrodes were discharged and recharged at  $0.05 \text{ mA cm}^{-2}$  under  $\text{O}_2$  bubbling in  $\text{PYR}_{14}\text{TFSI} - 0.4 \text{ M LiTFSI}$ . Discharge was stopped after 24 h and charge was limited by working electrode voltage cut-off of 4.0 V vs  $\text{Li}^+/\text{Li}$ . The PBm electrodes were obtained by pipeting aliquots of an N-methyl pyrrolidone/PVDF-based ink on glassy carbon disk. Figure 4.2.16 compares the XRD patterns ( $0.02^\circ 2\theta$ , 10 s/step) of PBm/PVDF electrodes before any electrochemical tests, after discharge at  $0.05 \text{ mA cm}^{-2}$  and after recharge at  $0.025 \text{ mA cm}^{-2}$  with that of tabulated LiOH (ICDD diffraction pattern 00-032-0564) and  $\text{Li}_2\text{O}_2$  (ICDD diffraction pattern 00-002-1006).

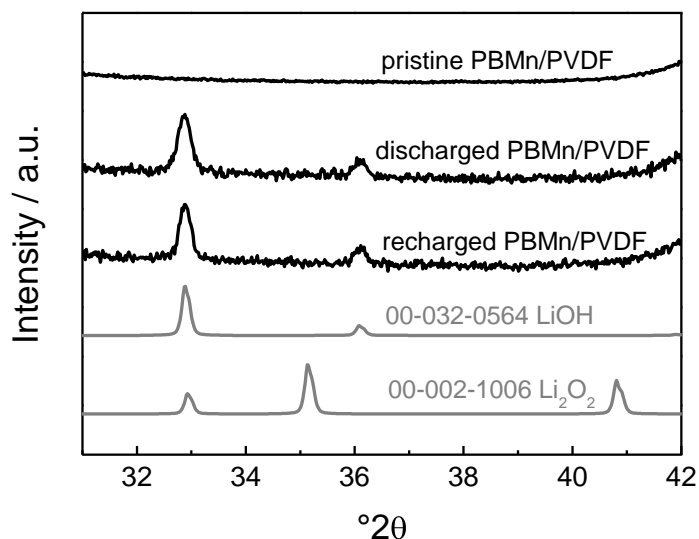


**Figure 4.2.16:** XRD of PBm/PVDF electrodes ( $1 \text{ mg cm}^{-2}$ ) pristine, after discharge and after recharge ( $0.02^\circ 2\theta$ , 10 s/step), LiOH (ICDD diffraction pattern 00-032-0564) and  $\text{Li}_2\text{O}_2$  (ICDD diffraction pattern 00-002-1006).

Figure 4.2.16 suggests that after discharge, PBm electrodes are coated by lithium hydroxide and do not feature  $\text{Li}_2\text{O}_2$ . After recharge, the peaks of lithium hydroxide are still present. From these attributions, it could be stated that manganese oxide promotes LiOH formation as demonstrated in Ref. [4.41] which reports that in presence of  $\alpha\text{MnO}_2$ , the  $\text{O}_2^-$  ion irreversibly reacts with PVDF to yield LiF and LiOH.

Hence, were tested PVDF-free electrodes prepared by casting of an hydroalcoholic ink of PureBlack-based powder - 5% Lithiate Nafion (Ion Power) on glassy carbon disk.

Figure 4.2.17 compares the XRD patterns of the PBMn/Nafion electrodes, before any electrochemical tests, after discharge and after recharge ( $0.02^\circ 2\theta$ , 10 s/step) at  $0.05 \text{ mA cm}^{-2}$ , with that of tabulated LiOH (ICDD diffraction pattern 00-032-0564) and  $\text{Li}_2\text{O}_2$  (ICDD diffraction pattern 00-002-1006).

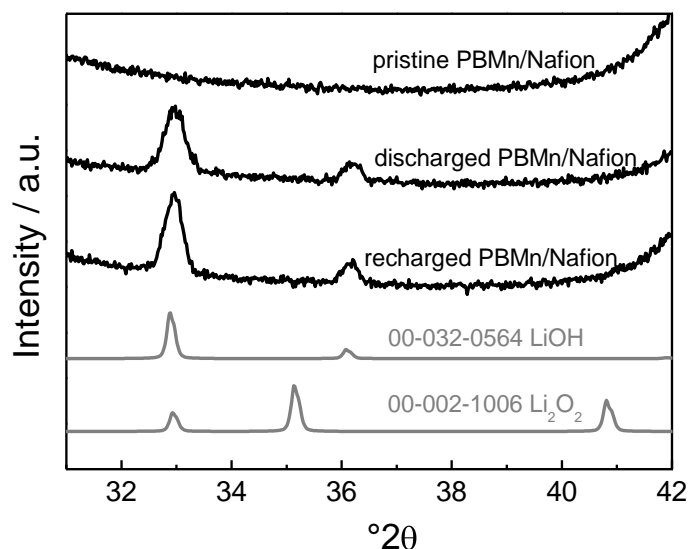
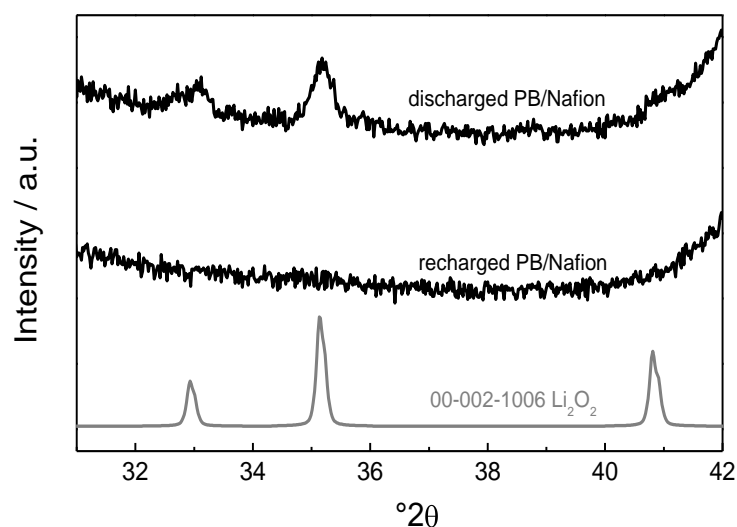


**Figure 4.2.17:** XRD of PBMn/Nafion electrodes ( $1 \text{ mg cm}^{-2}$ ) pristine, after discharge and after recharge ( $0.02^\circ 2\theta$ , 10 s/step), LiOH (ICDD diffraction pattern 00-032-0564) and  $\text{Li}_2\text{O}_2$  (ICDD diffraction pattern 00-002-1006)

The XRD patterns of the discharged and recharged electrodes overlap, but it has to be underlined that the recharge was very short and lasted only 2.5 h. Recharge current lower than  $0.05 \text{ mA cm}^{-2}$  had to be used to restore the electrode surface; however the carbon surface was not cleaned even by using lower charge currents. The XRD spectra of the discharge and charge electrodes do not match those of lithium oxide or lithium superoxide and are similar to those of lithium hydroxide but shifted to higher angles. Comparison of Figure 4.2.17 with Figure 4.2.16 suggests that substitution of PVDF with lithiated Nafion doesn't change any of the reduction products in contrast with how reported in Ref. [4.41] which shows that the use of lithiated Nafion as binder allows the formation of  $\text{Li}_2\text{O}_2$  avoiding that of LiOH.

In order to highlight the role of  $\alpha\text{MnO}_2$  in the  $\text{O}_2$  reduction process, were also tested electrodes based on bare PureBlack 205 carbon with 5% lithiated Nafion binder. In agreement with the results previously reported, the discharge of PB lasted 13h, much less than that of PBMn. Discharges stopped when electrode potential reached the voltage cut-off of 2 V vs  $\text{Li}^+/\text{Li}$ . Also for these electrodes, recharge was not possible at  $0.05 \text{ mA cm}^{-2}$ , hence the recharge current was set at  $0.025 \text{ mA cm}^{-2}$ . Figure 4.2.18 compares the XRD patterns of the PB/Nafion electrodes after discharge (a) and after recharge (b) ( $0.02^\circ 2\theta$ , 10 s/step), with that of  $\text{Li}_2\text{O}_2$  powder (c) and indicates that after discharge lithium peroxide is formed on the carbon surface and that such layer is not present in the recharged electrode (the small shift in peak position could be due to different focus plane of the two samples). These results are in agreement with those reported in Section 4.2.3 for ZL carbon.

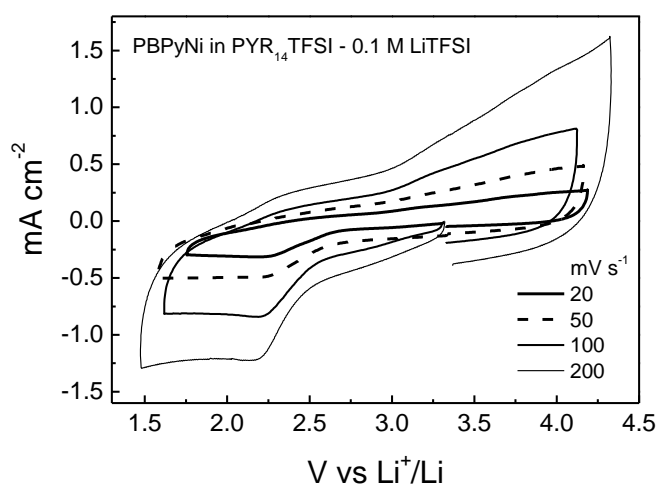
The presence of  $\text{LiOH}$  in PBMn electrodes containing both  $\alpha\text{MnO}_2$  and Nafion is presumably due to protons or water in the  $\alpha\text{MnO}_2$  structure. The importance to find a synthetic root which avoid crystallization water in the inorganic catalyst result fundamental for the use of these material in rechargeable non aqueous  $\text{Li}/\text{O}_2$  batteries.



**Figure 4.2.18:** XRD of PB/Nafion electrodes ( $1 \text{ mg cm}^{-2}$ ) after discharge (a) and after recharge (b) ( $0.02^\circ 2\theta$ , 10 s/step) and  $\text{Li}_2\text{O}_2$  powder (c).

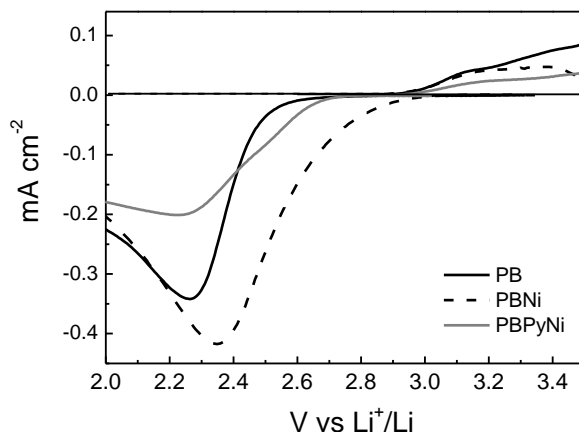
In order to evaluate the possible catalytic properties of Polypyrrole, the group of Kiev University functionalized PureBlack205 carbon with a mixture of inorganic ( $\text{NiCo}_2\text{O}_4$ ) and organic (Polypyrrole) catalysts (PBPyNi). For comparison also ZL carbon

was functionalized with  $\text{NiCo}_2\text{O}_4$  (ZLNi) and both  $\text{NiCo}_2\text{O}_4$  and PBPyNi (ZLPyNi), see Table 4.2.5 for the detailed composition. The materials were tested by cyclic voltammetry in  $\text{O}_2$ -saturated  $\text{PYR}_{14}\text{TFSI}$ -0.1 M LiTFSI. The electrodes were coated by  $0.5 \text{ mg cm}^{-2}$  of the different powder with 5% of PVDF as binder. Figure 4.2.19 shows the CVs of PBPyNi, background currents in  $\text{O}_2$ -saturated IL with lithium salt linearly increase with the scan rate, as expected for a double-layer capacitive carbon electrode. The voltammogram shows the same behavior previously described in Section 4.1.2 for pristine ZL carbon.



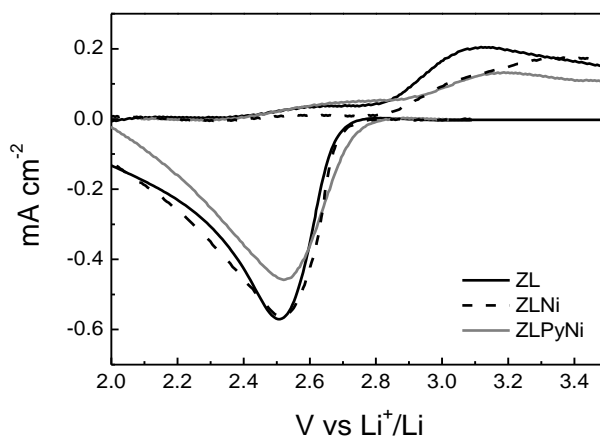
**Figure 4.2.19:** CVs of PBPyNi in  $\text{O}_2$ -saturated  $\text{PYR}_{14}\text{TFSI}$  - 0.1 M LiTFSI at  $30 \text{ }^\circ\text{C}$  at different scan rates.

Figure 4.2.20 compares the CVs in the 2 - 3.5 V vs.  $\text{Li}^+/\text{Li}$  range, corrected by background currents, at  $20 \text{ mV s}^{-1}$  of PBPyNi, pure PureBlack205 (PB) and PureBlack205 with 5% wt. of  $\text{NiCo}_2\text{O}_4$  (PBNi) samples. Figure 4.2.20 shows that PureBlack205 carbon has a different behavior after functionalizations. Modification of PB with  $\text{NiCo}_2\text{O}_4$  increases the reduction current while the presence of 10% in weight of polypyrrole seems to worsen the performance with respect to both PB and PBN.



**Figure 4.2.20:** CVs of PB (solid line), PBNi (dashed line), and PBPyNi (solid gray line) in  $O_2$ -saturated  $PYR_{14}TFSI - 0.1 M LiTFSI$  at  $30\text{ }^\circ C$  and  $20\text{ mV s}^{-1}$ .

In order to evaluate if the carbon nature influences the catalytic system behavior, CVs were also performed on ZL carbon samples modified with  $NiCo_2O_4$  and/or polypyrrole. Figure 4.2.21 compares the CVs in the 2 - 3.5 V vs.  $Li^+/Li$  range, corrected by background currents, at  $20\text{ mV s}^{-1}$  of ZLNi, ZLPyNi and pristine ZL carbon.



**Figure 4.2.21:** CVs of ZL (solid line), ZLNi (dashed line) and ZLPyNi (solid gray line) in  $O_2$ -saturated  $PYR_{14}TFSI - 0.1 M LiTFSI$  at  $30\text{ }^\circ C$  and  $20\text{ mV s}^{-1}$ .

From the Figure it is clear that the functionalization of ZL carbon with  $NiCo_2O_4$  without and with polypyrrole doesn't produce any relevant effect on the carbon performance. Moreover from the data obtained for PB and ZL carbons, the presence of polypyrrole seems to decrease the current intensity independently from the nature of the carbonaceous matrix.

### 4.2.6 Summary of the synthesis and characterisation of meso-macro porous carbons for ORR process

Different disordered template porous carbons were synthesized and characterized. The meso-macroporous carbon named ZL, featuring a pore size distribution centered at 54 nm and a  $V_{2-100\text{ nm}}$  of  $0.73\text{ cm}^3\text{ g}^{-1}$ , was tested as cathode material and delivered a specific discharge capacity of  $2500\text{ mAh g}^{-1}$  at  $0.05\text{ mA cm}^{-2}$ . Carbon derivatization with etheroatoms or catalytic systems did not shown any improvement of ZL electrochemical performance, hence the bare ZL carbon was selected as the best cathodic material to be used in LABOHR project.

ZL carbon obtained by a simple, low-cost template synthesis and commercial  $\text{PYR}_{14}\text{TFSI}$ -based IL provides a real possibility for the development of rechargeable  $\text{Li}/\text{O}_2$  batteries that can safely operate even above room temperature.

## 4.3 Limiting factors to the electrode capacity and cell cycle life

From the data obtained in  $\text{O}_2$ -saturated  $\text{PYR}_{14}\text{TFSI} - 0.1\text{ M LiTFSI}$  at the low discharge current of  $0.05\text{ mA cm}^{-2}$ , and reported in Section 4.2, ZL carbon was chosen as the best performing electrode material for ORR. One of the aspects of IL-based  $\text{Li}/\text{O}_2$  batteries that needs to be improved is cell response at higher discharge rates which is of interest for automotive applications. Literature reports that specific capacity lowers with the increase of the discharge current and the decrease of operating temperature [4.38, 4.42, 4.43].

In this PhD work the different factors that can have an influence on the  $\text{Li}/\text{O}_2$  battery performance were investigated. Section 4.3.1 reports the study of the role of  $\text{O}_2$  mass transport on the discharge capacity, Section 4.3.2 reports consideration about the recharge efficiency and cathode cycle life.

### 4.3.1 Role of oxygen mass transport

With the aim of understanding the role of  $O_2$  mass transport on  $O_2$  reduction at carbon electrode operating in IL, several experiments were carried out with and without  $O_2$  bubbling in  $O_2$ -saturated electrolyte in different experimental conditions. The study was performed with ZL carbon-based electrodes in  $PYR_{14}TFSI - 0.4 \text{ M LiTFSI}$ , in the conventional 3-electrode cell described in Section 2.2.3 (Figure 2.3a).

Figure 4.3.1 shows the galvanostatic discharge/charge profiles of a ZL-coated glassy carbon (ZL/GC) electrode under vigorous bubbling at  $0.05 \text{ mA cm}^{-2}$  (red line, I) and  $0.10 \text{ mA cm}^{-2}$  (blue line, II).

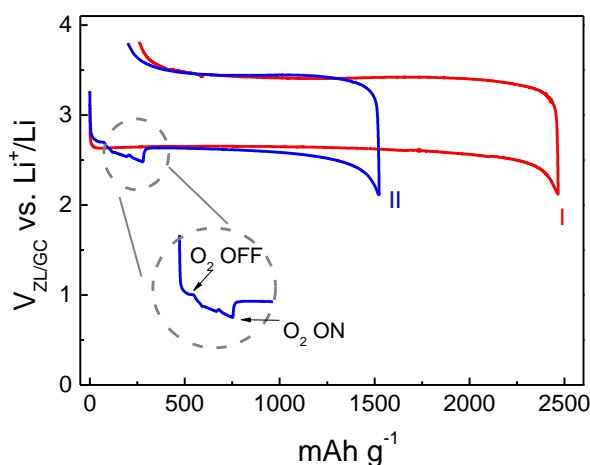


**Figure 4.3.1:** Voltage profiles upon galvanostatic discharge/recharge of the ZL/GC electrode in  $O_2$ -saturated  $PYR_{14}TFSI - 0.4 \text{ M LiTFSI}$  at (I)  $0.05$  and (II)  $0.10 \text{ mA cm}^{-2}$  with  $2.0$  and  $4.0 \text{ V vs. Li}^+/Li$  discharge and charge cut-off under vigorous  $O_2$  bubbling and  $30 \text{ }^\circ\text{C}$  ( $0.5 \text{ mg cm}^{-2}$  of carbon) [adapted from Ref. 4.3].

The shape of the curve at the lowest current was already explained considering that, upon discharge, the active area of the ZL/GC electrode is progressively clogged by insoluble oxygen reduction species which, at the end of discharge, cause electrode polarization. During recharge, insoluble species are reoxidized, the electrode active area is recovered and, at the end of charge, electrode potential raises (see Section 4.2.3). The electrode capacity decreases by 40 % when the current increases from  $0.05 \text{ mA cm}^{-2}$  to  $0.10 \text{ mA cm}^{-2}$ , at  $30 \text{ }^\circ\text{C}$ , with only modest effects on discharge and charge voltage plateau

and this suggests that electrode clogging is not limiting capacity at the latter current. The inset of Figure 4.3.1, which is a magnification of the discharge curve at  $0.10 \text{ mA cm}^{-2}$ , shows that  $\text{O}_2$  flow is crucial: interruption of  $\text{O}_2$  bubbling in  $\text{O}_2$ -saturated electrolyte during the discharge at the highest rate, abruptly lowers the electrode discharge potential, which is then restored when  $\text{O}_2$  flow is re-established.

Figure 4.3.2a and b show the results of the galvanostatic tests of the ZL carbon in  $\text{O}_2$ -saturated electrolyte, without  $\text{O}_2$  bubbling at different currents and temperatures.

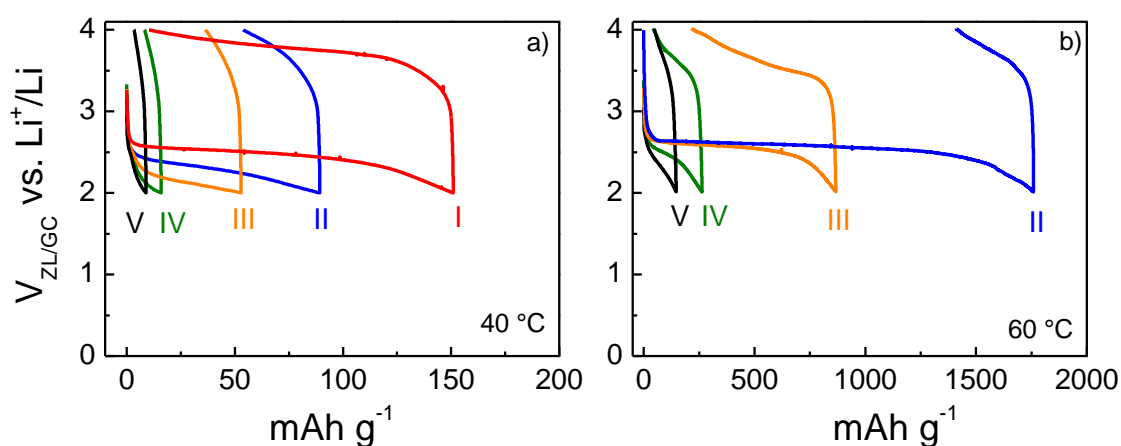


**Figure 4.3.2:** Voltage profiles upon galvanostatic discharge/recharge of the ZL/GC electrode in  $\text{O}_2$ -saturated  $\text{PYR}_{14}\text{TFSI} - 0.4 \text{ M LiTFSI}$  at (I)  $0.05$ ; (II)  $0.10$ , (III)  $0.15$ , (IV)  $0.20$  and (V)  $0.25 \text{ mA cm}^{-2}$  with  $2.0$  and  $4.0 \text{ V vs. Li}^+/\text{Li}$  discharge and charge cut-off, without  $\text{O}_2$  bubbling at (a)  $40 \text{ }^\circ\text{C}$  and (b)  $60 \text{ }^\circ\text{C}$  ( $1 \text{ mg cm}^{-2}$  of carbon) [adapted from Ref. 4.3].

At the lowest temperature of  $40 \text{ }^\circ\text{C}$  (Figure 4.3.2a), the specific capacity of the carbon electrode is one order of magnitude lower than that reported in Figure 4.3.1, which refers to experiments carried out under vigorous bubbling. The increase of current density from  $0.05 \text{ mA cm}^{-2}$  to  $0.25 \text{ mA cm}^{-2}$  causes severe electrode overvoltages and determines a marked decrease of the discharge specific capacity. Figure 4.3.2b shows that when the temperature is raised up to  $60 \text{ }^\circ\text{C}$ , the discharge capacity is greatly improved at each current density. The temperature increase does not significantly alter  $\text{O}_2$  concentration and has the major effect on  $\text{O}_2$  diffusion coefficient which almost doubles moving from RT to  $60 \text{ }^\circ\text{C}$  along with the decrease of the IL viscosity [4.44]. However, even at  $60 \text{ }^\circ\text{C}$  the

capacity lowers with current increase. Despite that the discharges at  $0.15 \text{ mA cm}^{-2}$  and  $0.10 \text{ mA cm}^{-2}$  and  $60 \text{ }^\circ\text{C}$  take place at almost the same plateau of  $2.6 \text{ V vs. Li}^+/\text{Li}$ , thus indicating that at such rates the overpotentials are not much affected by electrode kinetics, the capacity delivered at the former current is almost half than that at the latter and this can be explained with  $\text{O}_2$  mass transport limitations in IL which give rise to a Sand-like discharge behavior [4.12]. Upon discharge, the potential of the electrode moves to values characteristic of the ORR process and varies with time as the  $\text{O}_2/\text{O}_2^-$  concentration ratio at the electrode surface decreases. After the concentration of  $\text{O}_2$  drops to zero at the electrode surface, the flow of  $\text{O}_2$  to the surface could become insufficient to accomplish the applied discharge current (the diffusion layer extends into the bulk of the electrolyte solution and the concentration gradient decreases), and, consequently, the electrode potential rapidly shifts toward more negative values where different processes can occur. This transition time is related to  $\text{O}_2$  concentration and diffusion coefficient. Therefore, while electrode porous surface clogging is the main cause of the end of discharge at low currents and high temperatures,  $\text{O}_2$  mass transport in the electrolyte dominates electrode response at high currents and low temperatures. The role played by the  $\text{O}_2$  transport in the electrode discharge is clearly demonstrated by Figure 4.3.3 which reports the galvanostatic discharge/recharge at  $0.25 \text{ mA cm}^{-2}$  of the ZL/GC electrode under vigorous bubbling in unstirred and mechanically stirred solution.

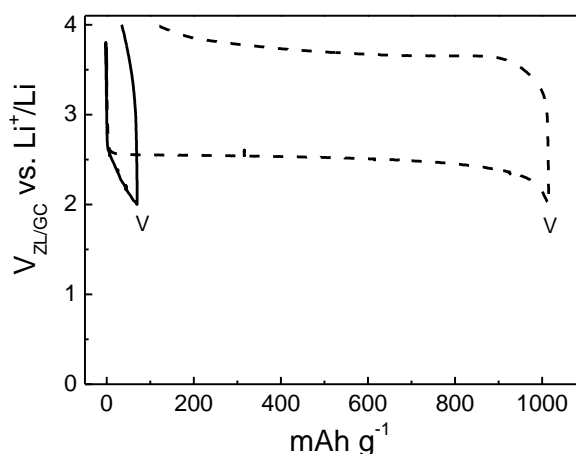


**Figure 4.3.3:** Voltage profiles upon galvanostatic discharge/recharge of the ZL/GC electrode in  $\text{O}_2$ -saturated  $\text{PYR}_{14}\text{TFSI} - 0.4 \text{ M LiTFSI}$  at (V)  $0.25 \text{ mA cm}^{-2}$  with  $2.0$  and  $4.0 \text{ V vs. Li}^+/\text{Li}$  discharge and charge cut-off, under vigorous  $\text{O}_2$  bubbling in unstirred (solid line) and mechanically stirred (dashed line) electrolyte and  $40 \text{ }^\circ\text{C}$  ( $1 \text{ mg cm}^{-2}$  of carbon) [adapted from Ref. 4.3].

Comparison of Figure 4.3.3 with Figure 4.3.2a evidences that vigorous bubbling in unstirred solution allows a 10 fold increase of the specific capacity (from ca. 10 to ca. 100 mAh g<sup>-1</sup>) at the high current density of 0.25 mA cm<sup>-2</sup> and at 40 °C. When stirring is on, O<sub>2</sub> mass transport is enhanced, the transition time increases and up to more than 1000 mAh g<sup>-1</sup> discharge capacity is achieved.

In order to perform a better control of O<sub>2</sub> mass transport and to evaluate the ZL carbon response at high current rate, the discharge/recharges were carried out at 0.5 mA cm<sup>-2</sup> (corresponding to 0.5 mA mg<sup>-1</sup>) and different temperatures by rotating the electrode (ZL/RGC) at different rates and the results are reported in Figure 4.3.4.

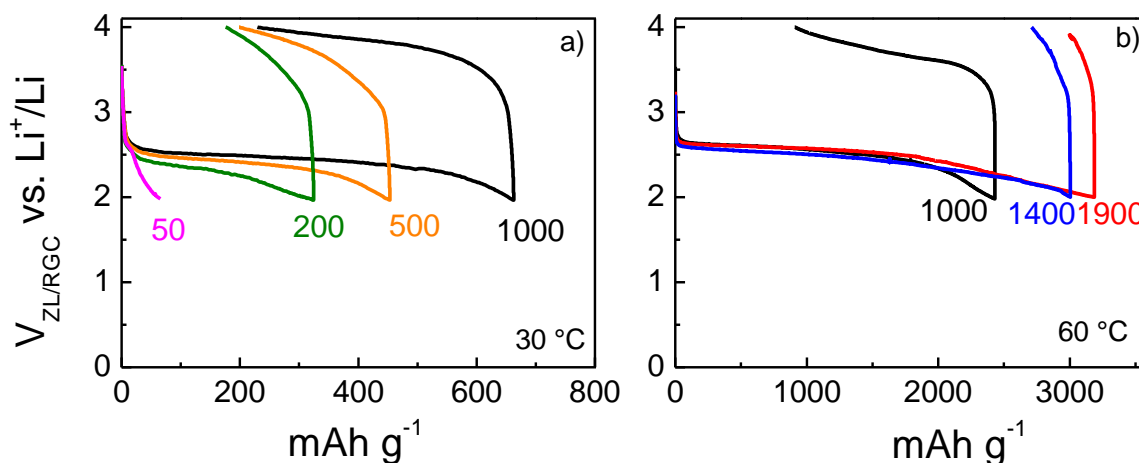


**Figure 4.3.4:** Voltage profiles upon galvanostatic discharge/recharge of the ZL/RGC electrode (1 mg cm<sup>-2</sup> of carbon) at 0.5 mA cm<sup>-2</sup> and different rpm in O<sub>2</sub>-saturated PYR<sub>14</sub>TFSI:LiTFSI 9:1 at (a) 30 °C and (b) 60 °C; labels indicate the electrode rotation rate in rpm [adapted from Ref. 4.3].

At 30 °C (Figure 4.3.4a), the discharge is feasible only when the rotation is faster than 200 rpm; the specific capacity increases with rotation rates reaching only 700 mAh g<sup>-1</sup> at 1000 rpm. This indicates that, in such conditions, electrode rotation is not sufficiently fast with respect to the applied current to provide a stationary concentration gradient and O<sub>2</sub> mass transport is still limiting the capacity. Figure 4.3.4b demonstrates that when O<sub>2</sub> mass transport is enhanced by increasing temperature and electrode rotation, the discharge is further improved and reaches the high value of 3150 mAh/g at 1400 rpm, comparing well to that displayed by ZL/GC electrodes at 10 fold lower current (see Figure 4.3.1). The curves at 1400 and 1900 rpm reported in Figure 4.3.4b almost overlap thus suggesting that,

in such conditions, electrode rotation is sufficiently fast to provide a stationary concentration gradient and that electrode saturation by insoluble discharge products is determining the discharge capacity. This kind of measurement strongly supports the idea that the achievable specific capacity at high discharge rate is limited by mass transport of  $O_2$  from the electrolyte bulk to the electrode surface.

The effect of  $O_2$  mass transport was investigated in the full flow-cell described in the experimental section (Section 2.2.3, Figure 2.3b) where the oxygen electrode is completely wetted with the liquid electrolyte and operates in two-phase reaction mode. The cell was fed with  $O_2$ -saturated IL-TFSI electrolyte which was circulated through the Li/ZL-coated carbon paper (ZL/CP) cell core by a peristaltic pump and continuously enriched with  $O_2$ . The cell also featured a reference electrode that was used to separately monitor the positive and negative electrode potentials upon the discharge/recharge tests which were performed at room temperature. Figure 4.3.5a reports the cell voltage and the positive and negative electrode potentials upon discharge/recharge cycles that were performed at  $0.2 \text{ mA cm}^{-2}$  without and with electrolyte circulation after 1 h of vigorous  $O_2$  bubbling. It is evident that in static conditions the cell is not able to operate at such high current rate. Only when the  $O_2$ -saturated electrolyte is flowed, the cell delivers  $600 \text{ mAh g}^{-1}$  (only considering  $1 \text{ mg cm}^{-2}$  ZL carbon loading) with a high 91.8 % recharge efficiency. This result, that can be ameliorated by cell and operative condition optimization, suggests that it is possible to cycle the IL-based Li/ $O_2$  cell even at high currents, provided that  $O_2$  mass transport and, hence electrolyte flow rate, is tuned to the applied discharge rate. Notwithstanding electrolyte circulation, and unlike previously reported good cyclability data performed in conventional 3-electrode cell (see Section 4.2.3), the capacity of the flow-cell was not retained over cycling. It is worth noting that unlike single electrode tests, that were carried out using a great excess of lithium counter electrode, flow-cell measurements were carried out with positive and negative electrodes featuring the same geometric area. This implies that cell performance was also affected by lithium anode behavior. Lithium was not coated by any protective layer and was separated from the cathode only by a fiber glass separator. Figure 4.3.5a shows that the lithium metal overpotential increased over the 3 h discharge of the 2<sup>nd</sup> cycle by ca. 180 mV. After 1 day test the lithium surface was coated by a black, resistive passivation layer. Evolution of electrode resistance before and after cycling was monitored by electrochemical impedance

spectroscopy (EIS) in three-electrode mode and the results are reported as Nyquist plots in Figure 4.3.5b. The impedance response of the ZL/CP electrode is almost unmodified before and after the galvanostatic tests and corresponds to that of a porous carbon in IL which features a high frequency semicircle due to electronic and ionic contact resistances that contribute by  $50 \Omega \text{ cm}^2$  to the electrode impedance and a low frequency transmission line due to the capacitive properties of the carbon. The Nyquist plot of the lithium anode is dominated by a low frequency semicircle which is ascribed to the solid electrolyte interphase with a real axis intercept of  $165 \Omega \text{ cm}^2$  which increases up to  $200 \Omega \text{ cm}^2$  after 1 day cycling, thus dominating the overall the cell impedance evolution.

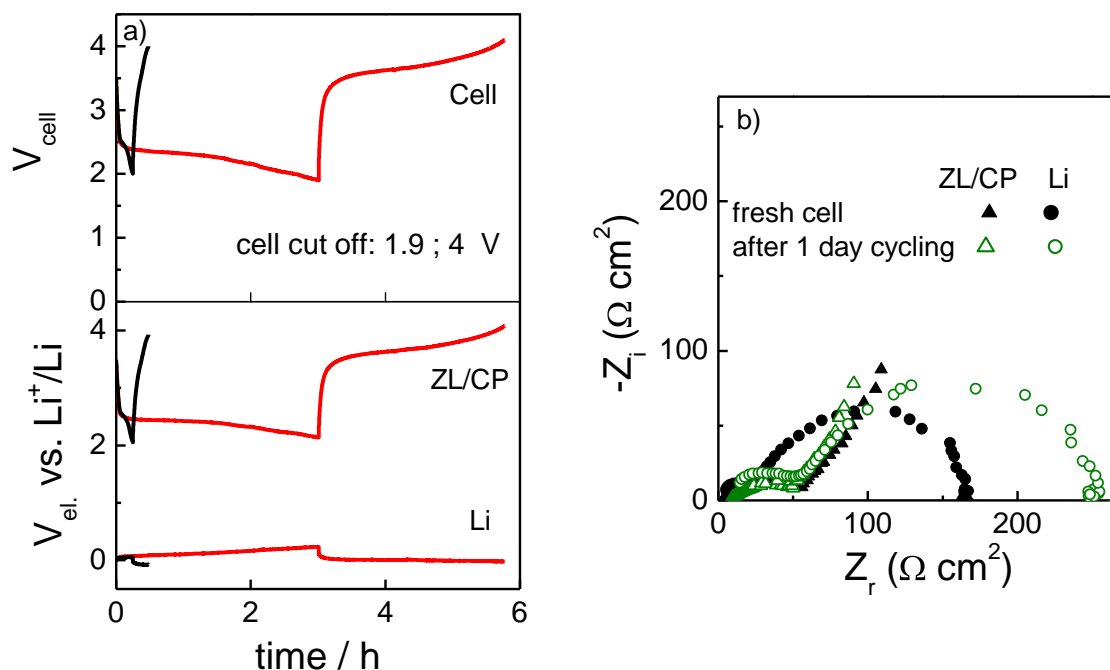


**Figure 4.3.5:** a) flow battery voltage and ZL/CP and Li electrode potentials vs.  $\text{Li}^+/\text{Li}$  upon discharge/recharge cycles at RT and  $0.2 \text{ mA cm}^{-2}$ : 1<sup>st</sup> cycle (black curves) with pump off and 2<sup>nd</sup> cycle (red curves) with pump on; b) Nyquist plots of the ZL/CP cathode and Li anode before (black symbols) and after 1 day (green symbols) discharge/recharge tests (100 kHz-200 mHz) [adapted from Ref. 4.3].

In order to increase the lithium stability in the same flow-cell previously used (see Section 2.2.3, Figure 2.3b), a ternary Poly(ethylene oxide)-based solid electrolyte was tested as feasible electrode protective membrane. Figure 4.3.6 shows the cell voltage and the positive and negative electrode potentials upon discharge/charge cycle that were

performed at  $0.2 \text{ mA cm}^{-2}$  with electrolyte circulation after 1 h of vigorous  $\text{O}_2$  bubbling. Due to the presence of PEO-based layer the cell was cycled at  $60 \text{ }^\circ\text{C}$  to increase the  $\text{Li}^+$  mobility through the membrane. The potential profile of lithium evidences that Li protection by the membrane which should prevent the direct contact of metal lithium with the  $\text{O}_2$ -rich electrolyte, was not good, at least in the used flow-cell.

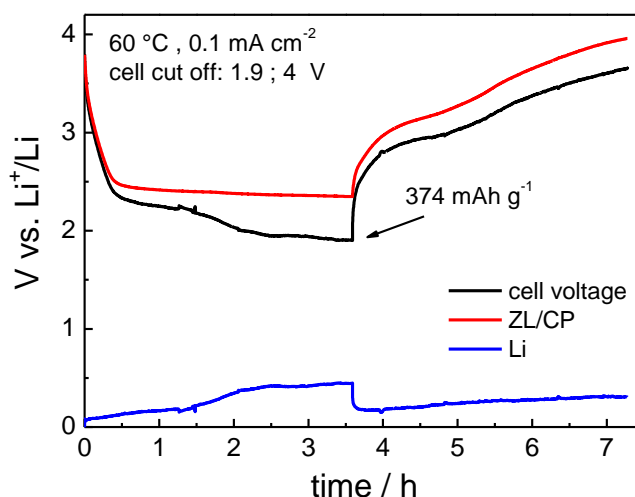


**Figure 4.3.6:** Flow battery voltage (black line), ZL/CP (red line) and Li electrode (blue line) potentials upon discharge/recharge cycle at  $60 \text{ }^\circ\text{C}$  and  $0.2 \text{ mA cm}^{-2}$ .

Other different flow-cell designs (reported in Figure 4.3.7a-c) were tested with the aim of finding an optimum cell geometry which can avoid lithium passivation. The cell designs of Figure 4.3.7b and c are still under development at the MEET Institute, Münster - Germany (partner of the European project LABOHR).

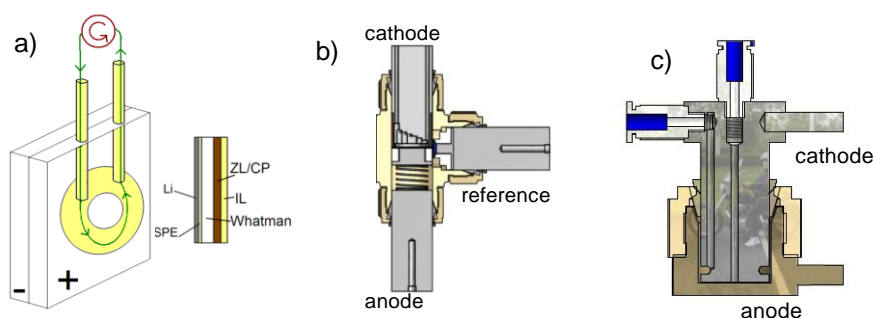


**Figure 4.3.7:** Scheme of three different  $\text{Li}/\text{O}_2$  flow-cell designs.

### 4.3.2 Recharge efficiency and cathode cycle life

Due to the fact that, as previously described in Section 4.3.1, in the flow-cell configuration adopted (see Section 2.2.3, Figure 2.3b) the lithium anode seems to be the electrode which limits the cyclability, the cathode cycle life was studied in a conventional 3-electrodes cell (see Section 2.2.3, Figure 2.3a) where an excess of the lithium metal at the counter electrode should account for a good operation of the working electrode. All the experiments were performed in  $O_2$ -saturated  $PYR_{14}TFSI - 0.4 M LiTFSI$  using ZL-coated ( $1 mg cm^{-2}$ ) RDE positive electrodes that were only partially discharged.

In the two galvanostatic discharge/charge cycles shown in Figure 4.3.8 the RDE rotation speed was set at 1000 rpm for all the discharges and varied from 1000 rpm to 500 rpm for the recharges. The discharge capacity was limited to  $750 mAh g^{-1}$ . Figure 4.3.8 reports also the recharge efficiency ( $\eta$ ) for each cycle. From the obtained results it is possible to conclude that the recharge efficiency is not much affected by the rotation speed of the electrode, i.e. the it is not affected by the mass transport of the oxidation products of  $Li_2O_2$ .

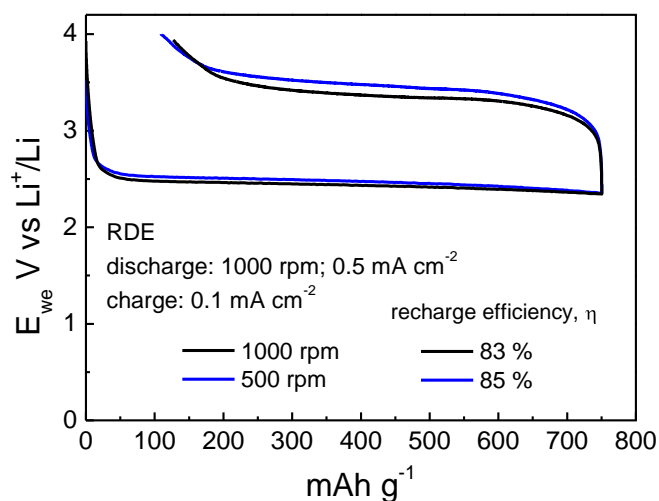


**Figure 4.3.8:** Voltage profiles upon galvanostatic discharge/recharge of the ZL/RGC electrode ( $1 mg cm^{-2}$  of carbon) at  $0.5 mA cm^{-2}$ , in  $O_2$ -saturated  $PYR_{14}TFSI - 0.4 M LiTFSI$  at  $30 ^\circ C$ . RDE rotation speed was set at 1000 rpm for all the discharges and varied from 1000 rpm (black line) to 500 rpm (blue line) for the recharges.

Figure 4.3.9 reports the influence of the charge current on the recharge efficiency. The measurements were carried out with the RDE rotation speed set at 1000 rpm during the cycling. The discharge current was set to  $0.5 \text{ mA cm}^{-2}$  while for the recharge three different current values were applied. The discharge capacity was fixed at  $370 \text{ mAh g}^{-1}$ .

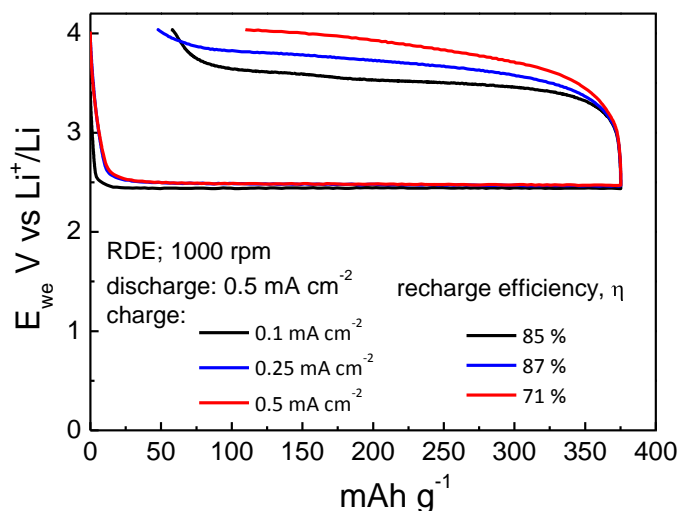


**Figure 4.3.9:** Voltage profiles upon galvanostatic discharge/recharge of the ZL/RGC electrode ( $1 \text{ mg cm}^{-2}$  of carbon) at discharge current of  $0.5 \text{ mA cm}^{-2}$ , in  $\text{O}_2$ -saturated  $\text{PYR}_{14}\text{TFSI} - 0.4 \text{ M LiTFSI}$  at  $30 \text{ }^\circ\text{C}$ ; the recharge current was  $0.1 \text{ mA cm}^{-2}$  (black line),  $0.25 \text{ mA cm}^{-2}$  (blue line) and  $0.5 \text{ mA cm}^{-2}$  (red line).

The increasing of the charge current reflects in the increase of charge overpotential, which in turn negatively influences the recharge efficiency. When the current densities was varied from  $0.1 \text{ mA cm}^{-2}$  to  $0.25 \text{ mA cm}^{-2}$  the recharge plateau increased by c.a. 200 mV and the recharge efficiency did not change significantly, with a values of 85-87 %. When a charge current of  $0.5 \text{ mA cm}^{-2}$  was used the oxidation plateau increased by other 200 mV with respect to the value at  $0.25 \text{ mA cm}^{-2}$  and the recharge efficiency dropped to c.a. 70 %.

The data reported in Figure 4.3.8 and 4.3.9 gave indications about suitable operative conditions for the cyclability tests that were performed at rotation speed of 1000 rpm, and current density of  $0.5 \text{ mA cm}^{-2}$  and  $0.25 \text{ mA cm}^{-2}$  for discharge and charge respectively. The cycled discharge capacity was fixed to  $750 \text{ mAh g}^{-1}$ . The experiments were carried out at  $30 \text{ }^\circ\text{C}$  and  $60 \text{ }^\circ\text{C}$  with potential cut-off of  $2 \text{ V vs Li}^+/\text{Li}$  and  $4 \text{ V vs Li}^+/\text{Li}$  and are reported in Figure 4.3.10a and b respectively.

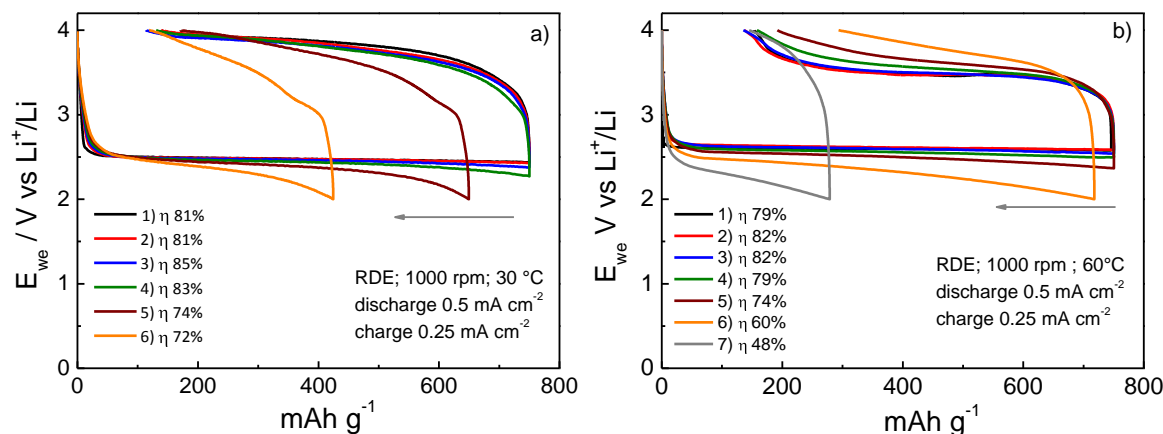


**Figure 4.3.10:** Voltage profiles upon galvanostatic discharge/recharge of the ZL/RGC electrode ( $1 \text{ mg cm}^{-2}$  of carbon) in  $\text{O}_2$ -saturated  $\text{PYR}_{14}\text{TFSI} - 0.4 \text{ M LiTFSI}$  at current density of  $0.5 \text{ mA cm}^{-2}$  and  $0.25 \text{ mA cm}^{-2}$  for discharge and charge respectively and 1000 rpm at (a)  $30 \text{ }^\circ\text{C}$  and (b)  $60 \text{ }^\circ\text{C}$ ; labels indicate the recharge efficiency of each cycle.

Figure 4.3.10 shows a poor electrode cycle life both at  $30 \text{ }^\circ\text{C}$  and  $60 \text{ }^\circ\text{C}$ . For few cycles the electrodes were able to provide the fixed discharge capacity at potential higher than  $2.4 \text{ V vs Li}^+/\text{Li}$ , with recharge efficiency of c.a.  $80 \%$ . After the first 4 or 6 cycles, it is visible a gradual loss of capacity and the discharge profiles reached the potential cut-off of  $2 \text{ V vs Li}^+/\text{Li}$ , then the discharge capacity dropped below  $400 \text{ mAh g}^{-1}$ . The observed poor cycle life was presumably due to the low recharge efficiency of each cycle and to the increase of the electrode resistance.

With the aim to verify if the low recharge efficiency could be due to low  $\text{Li}_2\text{O}_2$  oxidation kinetics [4.45], the electrochemical characterization of the RDE electrode was also carried out at  $30 \text{ }^\circ\text{C}$  in  $\text{O}_2$ -saturated  $\text{PYR}_{14}\text{TFSI} - 0.4 \text{ M LiTFSI}$  by galvanostatic discharge (CC, at  $0.5 \text{ mA cm}^{-2}$  down to  $2 \text{ V vs. Li}^+/\text{Li}$ ) and galvanostatic (CC, at  $0.25 \text{ mA cm}^{-2}$  up to  $3.8 \text{ V vs. Li}^+/\text{Li}$ )-potentiostatic (CV, down to  $5 \%$  of the recharge current) recharge cycles. The potentiostatic recharge should overcome any kinetic limitations, allowing the complete reoxidation of the reduction product; the evolution of electrode resistance before and after cycling was monitored by electrochemical impedance spectroscopy (EIS). Figure 4.3.11a reports the discharge profiles of the electrode tested by discharge (CC)-charge (CC-CV) and Figure 4.3.11b shows the evolution of impedance spectra before and after cycling.

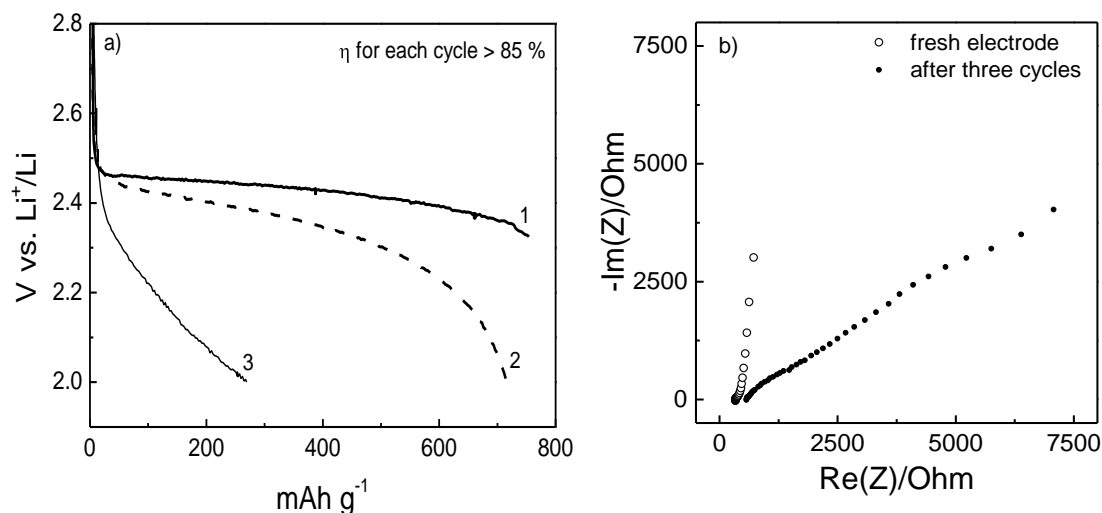


**Figure 4.3.11:** a) CC discharge curves (30 °C) at 0.5 mA cm<sup>-2</sup> of fully charged, CC(0.25 mA cm<sup>-2</sup>)-CV ZL/RDE (1 mg cm<sup>-2</sup> of ZL, 1000 rpm), labels indicate the cycle number; b) Nyquist plots of the ZL/RDE electrode before cycling (empty symbols) and after the 3<sup>rd</sup> cycle (black symbols) (3 kHz-200 mHz).

Figure 4.3.11a shows that the electrode cyclability remains very low even by CV charge mode and this suggests that low efficiency cannot be related to slow Li<sub>2</sub>O<sub>2</sub> oxidation kinetics. The impedance spectra reported in Figure 4.3.11b confirm the increase of electrode resistance after discharge/charge cycling. The Nyquist plot changes from that typical of a capacitive electrode before cycling to that for diffusion controlled processes after cycling. Figure 4.3.12 reports the XRD spectra recorded after the first discharge and the last recharge which are similar to those described in Section 4.2.3, Figure 4.2.9. Li<sub>2</sub>O<sub>2</sub> is the only discharge product and after the recharge no crystalline product was observed; further studies are needed to determine the nature of the passivation layer which may form on the electrode surface which is critical for diffusion of the chemical species involved in ORR into the electrode, as suggested by EIS.

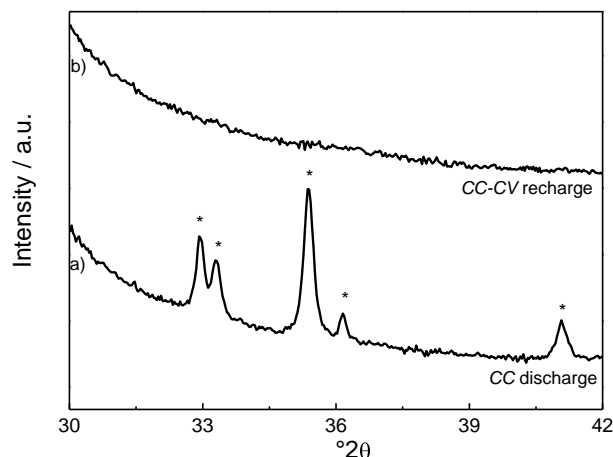


**Figure 4.3.12:** XRD of ZL/RDE electrodes ( $1 \text{ mg cm}^{-2}$ ) after the 1<sup>st</sup> discharge (a) and after the 3<sup>rd</sup> CC-CV recharge (b) ( $\text{Li}_2\text{O}_2$  powder peaks are marked).

It is worth noting that the reported poor cyclability seems to be independent from electrolyte nature. Indeed, literature reports that even  $\text{Li}/\text{O}_2$  batteries operating in DMSO-based electrolyte [4.46] show the behavior reported above for the LABOHR IL-based cells.

### 4.3.3 Summary of limiting factors to the electrode capacity and cell cycle life

Section 4.3 demonstrates that oxygen electrode response in IL at high discharge currents is dominated by the  $\text{O}_2$  properties in the electrolyte. While electrode characteristics like porosity and catalytic activity towards ORR can be effective at the slowest currents,  $\text{O}_2$  mass transport in the bulk of IL becomes crucial at the fastest discharges which are of interest for automotive applications. The study also demonstrates that it is possible to overcome intrinsic limitation of  $\text{O}_2$  mass transport to the electrode surface by a novel flow-cell concept which is the core of the EU LABOHR Project (where oxygen-harvesting from air is split from the oxygen reaction process) [4.47]. Further advances in IL-based  $\text{Li}/\text{O}_2$  cell performance are expected by optimization of the overall cell design in relation to the target operative conditions. The main drawbacks that still remain to be overcome to make  $\text{Li}/\text{O}_2$  batteries operating in ILs feasible for application is the not sufficient high recharge efficiency which is detrimental for cell cycle-life.

## 4.4 References

- [4.1] S. Monaco, A. Arangio, F. Soavi et al, *Electrochim. Acta*, **83** (2012) 94  
(Reproduced with permission Copyright 2012 Elsevier)
- [4.2] F. Soavi, S. Monaco, M. Mastragostino, *J. Power Sources*, **224** (2013) 115  
(Reproduced with permission Copyright 2012 Elsevier)
- [4.3] S. Monaco, F. Soavi, M. Mastragostino, *J. Phys. Chem. Lett.*, **4** (2013) 1379  
(Reproduced with permission Copyright 2013 American Chemical Society)
- [4.4] R.G. Evans, O.V. Klymenko, S.A. Saddoughi, et al, *J. Phys. Chem. B*, **108** (2004) 7878
- [4.5] Y. Katayama, H. Onodera, M. Yamagata, et al, *J. Electrochem. Soc.*, **151** (2004) A59
- [4.6] Y. Katayama, K. Sekiguchi, M. Yamagata, et al, *J. Electrochem. Soc.*, **152** (2005) E247
- [4.7] M. Hayyan, F.S. Mjalli, M.A. Hashim, et al, *J. Electroanal. Chem.*, **657** (2011) 150
- [4.8] L. Damen, M. Lazzari, M. Mastragostino, *J. Power Sources*, **196** (2011) 8692
- [4.9] Q. Zhou, W.A. Henderson, G.B. Appetecchi, et al, *J. Phys. Chem. B*, **112** (2008) 13577
- [4.10] F. De Giorgio, F. Soavi, M. Mastragostino, *Electrochem. Commun.*, **13** (2011) 1090
- [4.11] M. Ishikawa, T. Sugimoto, M. Kikuta, et al, *J. Power Sources*, **162** (2006) 658
- [4.12] A.J. Bard, L.R. Faulkner, “*Electrochemical methods: Fundamentals and Applications*”, 2<sup>nd</sup> ed., John Wiley & Sons, Inc., New York, 2001  
(Figures reproduced with permission Copyright Wiley)
- [4.13] H. Matsuda, Y. Ayabe, *Z. Elektrochemie*, **59** (1955) 494
- [4.14] R.S. Nicholson, *Anal. Chem.*, **37** (1965) 1351
- [4.15] M.C. Buzzeo, O.V. Klymenko, J.D. Wadhawan, et al, *J. Phys. Chem. A*, **107** (2003) 8872
- [4.16] E.I. Rogers, X.-J. Huang, E.J.F. Dickinson, et al, *J. Phys. Chem. C*, **113** (2009) 17811
- [4.17] D. Zigah, A. Wang, C. Lagrost, et al, *J. Phys. Chem. B*, **113** (2009) 2019

- [4.18] C.O. Laoire, S.Mukerjee, K.M. Abraham, et al, *J. Phys. Chem. C*, **114** (2010) 9178
- [4.19] C.J. Allen, S. Mukerjee, E.J. Plichta, et al, *J. Phys. Chem. Lett.*, **2** (2011) 2420
- [4.20] Z. Peng, S.A. Freunberger, L.J. Hardwick, et al, *Angew. Chem. Int. Edit.*, **50** (2011) 6351
- [4.21] S.A. Freunberger, Y. Chen, N.E. Drewett, et al, *Angew. Chem. Int. Edit.*, **50** (2011) 8609
- [4.22] R. Wibowo, S.E. Ward Jones, R.G. Compton, *J. Phys. Chem. B*, **113** (2009) 12293
- [4.23] X. Yang, P. He, Y. Xia, *Electrochem. Commun.* **11** (2009)1127
- [4.24] R. Padbury, X. Zhang, *J. Power Sources*, **196** (2011) 4436
- [4.25] J. Xiao, D. Wang, W. Xu, et al, *J. Electrochem. Soc.*, **157** (2010) A487
- [4.26] G.O. Shitta-Bey, M. Mirzaeian, P.J. Hall, *J. Electrochem. Soc.*, **159** (2012) A315
- [4.27] C. Tran, J. Kafle, X. Yang, et al, *Carbon*, **49** (2011) 1266
- [4.28] Y. Li, J. Wang, X. Li, et al, *Electrochem. Commun.*, **13** (2011) 668
- [4.29] L. Yang, S. Jiang, Y. Zhao, et al, *Angew. Chem. Int. Ed.*, **50** (2011) 7132
- [4.30] C. Tran, X. Yang, D. Qu, *J. Power Sources*, **195** (2010) 2057
- [4.31] M. Mirzaeian, P.J. Hall, *Electrochim. Acta*, **54** (2009) 7444
- [4.32] A. Kraytsberg, Y. Ein-Eli, *J. Power Sources*, **196** (2011) 886
- [4.33] J. Christensen, P. Albertus, R.S. Sanchez-Carrera, et al, *J. Electrochem. Soc.*, **159** (2012) R1
- [4.34] S. Han, K.T. Lee, S.M. Oh, et al, *Carbon*, **41** (2003) 1049
- [4.35] J. Bong Joo, P. Kim, W. Kim et al, *J. Electroceram*, **17** (2006) 713
- [4.36] S.A. Al-Muhtaseb, J.A. Ritter, *Adv. Mater.*, **15** (2003) 101
- [4.37] P.G. Bruce, S. Freunberger, L.J. Hardwick, et al, *Nat. Mater.*, **11** (2012) 19
- [4.38] A. Garsuch, D.M. Badine, K. Leitner, et al, *Z. Phys. Chem.*, **226** (2012) 107
- [4.39] L. Cecchetto, M. Salomon, B. Scrosati, et al, *J. Power Sources*, **213** (2012) 233
- [4.40] M. Herstedt, M. Smirnov, P. Johansson, et al, *J. Raman Spectrosc.*, **36** (2005) 762
- [4.41] R. Black, S.H. Oh, J. Lee, et al, *J. Am. Chem. Soc.*, **134** (2012) 2902
- [4.42] F. Mizuno, K. Takechi, S. Higashi, et al, *J. Power Sources*, **228** (2013) 47
- [4.43] Z.H. Cui, W.G. Fan, X.X. Guo, *J. Power Sources*, **235** (2013) 251
- [4.44] C.J. Allen, J. Hwang, R. Kautz, et al, *J. Phys. Chem. C*, **116** (2012) 20755

[4.45] Y. Lu, Y. Shao-Horn, *J. Phys. Chem. Lett.*, **4** (2013) 93

[4.46] M.J. Trahan, S. Mukerjee, E. Plichta, et al, *J. Electrochem. Soc.*, **160** (2013) A259

[4.47] [www.laboehr.eu](http://www.laboehr.eu)

# Chapter 5

## Conclusions

This PhD work pursued two strategies to improve the energy of rechargeable lithium batteries for automotive applications. The first was the increase of the working voltage of lithium-ion batteries (LIBs) by the development of new cathodes operating in conventional electrolyte while the second was the increase of battery capacity by the development of Li/O<sub>2</sub> battery operating in ionic liquid (IL)-based electrolyte.

Regarding the study of LIBs the findings of LiMnPO<sub>4</sub> prepared by soluble precursors (method *II*) demonstrate that a good performing Mn-based olivine is viable, even without the coexistence of iron. The exclusion of Fe, which works at 3.5 V, is an advantage for battery energy because LiMnPO<sub>4</sub> delivers most part of the charge at 4 V. The proposed synthetic strategy has been further refined (in the frame of the Italian national program “*Ricerca di sistema elettrico*”) leading to an electrode material with a long cycle-life.

Regarding Li/O<sub>2</sub> battery, in the last 2 years an increasing number of papers focusing on the instability of conventional carbonate-based electrolytes underlined the importance to identify a stable electrolyte. In the frame of the European project “*Lithium-Air Batteries with split Oxygen Harvesting and Redox processes*” ILs were chosen as electrolytes media. In this PhD work the ORR was studied from the basic point of view and D<sub>O</sub> and C<sub>O</sub> values in different pure ILs were obtained. The studies performed in IL-0.1 M LiTFSI solutions showed that the presence of lithium ions causes chemical reactions following the first electrochemical step of superoxide formation that even yield LiO<sub>2</sub> and Li<sub>2</sub>O<sub>2</sub> as insoluble products on the electrode surface.

The stability of the selected IL, PYR<sub>14</sub>TFSI, to oxygen reduced species was demonstrated, confirming the good choice of this organic melted salt as electrolyte. The main disadvantages in the use of ILs are the low O<sub>2</sub> solubility and diffusion coefficient compared to those in more conventional electrolytes. This study highlighted that the key factor that limits the Li/O<sub>2</sub> capacity at the high currents of interest for automotive

application is the  $O_2$  mass transport in the bulk of the IL. Furthermore it gave indication on how to increase capacity by the use of a flow-cell and a cathode constituted by a meso-macro porous carbon obtained by a simple, low-cost template synthesis. Carbon/catalyst systems were also studied but their electrochemical performances were found worse than that of a synthesized unfunctionalized meso-macro porous carbon, the main reason is that the rate determining step of ORR in IL, that limits the  $Li/O_2$  capacity at high discharge rate, is the  $O_2$  mass transport to the electrode surface and not the electron transfer process, for which a catalyst can be useful.

This work provided indications useful for the design of a  $Li/O_2$  battery prototype which is under development by other partner in the frame of the European project LABOHR.

The main drawbacks that still remain to be overcome to make  $Li/O_2$  batteries operating in ILs feasible for application is recharge efficiency not sufficient high to guarantee a long cell cycle-life.

# Acknowledgements

First of all, I wish to thank my supervisor, Prof. Marina Mastragostino for the opportunity of pursuing PhD studies and for her scientific support during this thesis project. I also wish to acknowledge all my colleagues of the Laboratorio di Elettrochimica dei Materiali per l'Energetica (LEME) of the University of Bologna for their friendship, specially Dr. Francesca Soavi as my co-supervisor. I acknowledge Prof. Stefano Passerini for giving me the possibility to spent a period of two months at the battery research centre, Münster Electrochemical Energy Technology (MEET, Münster – Germany) and all the partners of EU-LABOHR project and of the Italian nation program “*Ricerca di sistema elettrico*” for the fruitful discussions on IL-based Li/O<sub>2</sub> batteries and high-voltage lithium-ion batteries.

Finally, I acknowledge the financial support provided by European Commission in the Seventh Framework Programme FP7-2010-GC-ELECTROCHEMICAL STORAGE “*Lithium-Air Batteries with split Oxygen Harvesting and Redox processes*” (LABOHR, contract no. 265971) and by Italian national program “*Ricerca di sistema elettrico*”, promoted by Ministero dello Sviluppo Economico and ENEA (Agenzia Nazionale per le Nuove Tecnologie, l'Energia e lo Sviluppo Economico Sostenibile).



## List of Presentations to Conferences

03-08/06/2012: Co-author of the presentation on “**Non-nobel Nano-composites for Oxygen Reduction**” at: *7<sup>th</sup> International Workshop on the Electrochemistry of Electroactive Materials- Szeged/Hungary*

\*28/06-01/07/2012: Presenting author of poster contribution on “**Synthesis and characterization of carbon-coated  $\text{LiMn}_{1-x}\text{Fe}_x\text{PO}_4$  (x=0, 0.2, 0.3 and 0.5) materials as high potential cathode for lithium-ion batteries**” at: *8<sup>th</sup> ECHEMS Meeting, Electrochemistry in Molecular Surface Science and Catalysis – Bertinoro/Italy.*

05-07/07/2012: Co-author of the presentation on “**High voltage lithium-ion batteries**” at: *6<sup>th</sup> Japanese-Italian-German Meeting of Electrochemists– Ulm/Germany*

\*06-07/05/2013: Presenting author of poster contribution on “**Tonic Liquid-based Li/O<sub>2</sub> batteries**” at: *Workshop Batteries for the future – Como/Italy*

08-13/09/2013: Co-author of the poster on “**Rechargeable Li/O<sub>2</sub> battery with Pyrrolidinium-Based Electrolyte**” presented at: *64<sup>th</sup> Annual Meeting of the International Society of Electrochemistry, Electrochemistry for a New Era – Santiago de Queretaro/Mexico*

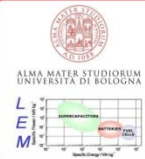
\*Posters are hereinafter reported



## Synthesis and characterization of carbon-coated $\text{LiMnPO}_4$ and $\text{LiMn}_{1-x}\text{Fe}_x\text{PO}_4$ ( $x=0.2, 0.3$ ) materials for lithium-ion batteries

**L. Damen, F. De Giorgio, S. Monaco, F. Veronesi, M. Mastragostino**

Università di Bologna, Dipartimento di Scienza dei Metalli, Elettrochimica e Tecniche Chimiche  
Via S. Donato 15, 40127 Bologna, Italy  
simone.monaco2@unibo.it



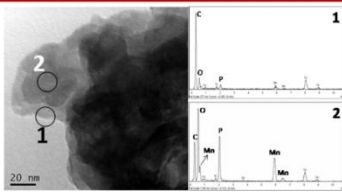
*Lithium transition metal phosphates are very attractive cathode materials for rechargeable lithium-ion batteries because of their chemical and thermal stability. The high performance of  $\text{LiFePO}_4$  has stimulated the search for other compounds as  $\text{LiMnPO}_4$  and  $\text{LiMn}_{1-x}\text{Fe}_x\text{PO}_4$ .  $\text{LiMnPO}_4$  is more advantageous material than  $\text{LiFePO}_4$  in terms of battery specific energy because of its higher working voltage (4.1 V vs. Li instead of 3.5 V) and the same theoretical capacity ( $170 \text{ mAh g}^{-1}$ )<sup>[1]</sup>. However, the delivered capacity and the cycling stability of  $\text{LiMnPO}_4$  phosphate are still under study.*

**Synthesis and structural, morphological and electrochemical characterizations in EC:DMC-LiPF<sub>6</sub> of carbon-coated  $\text{LiMnPO}_4$  and  $\text{LiMn}_{1-x}\text{Fe}_x\text{PO}_4$  ( $x=0.2, 0.3$ ) cathode materials are reported [2].**

**SYNTHESIS:** the precursors were dissolved in water in stoichiometric molar ratio and the aqueous systems were heated to rapidly evaporate water and to obtain dry gels. The gels were ground and then pyrolyzed in furnace in argon flow (ca. 200 ml/min) for 1 h at 700°C (20°C/min). The resulting black powders were further ground by wet ball milling in WC.

ABBREVIATION	SAMPLE	
M100(I)	$\text{LiMnPO}_4$	(I) synthesis from partially soluble precursors
MF8020(I)	$\text{LiMn}_{0.8}\text{Fe}_{0.2}\text{PO}_4$	
MF7030(I)	$\text{LiMn}_{0.7}\text{Fe}_{0.3}\text{PO}_4$	
M100(II)*	$\text{LiMnPO}_4$	(II) synthesis from totally soluble precursors

\* 2:1 molar ratio of  $\text{C}_6\text{H}_8\text{O}_7 \cdot \text{H}_2\text{O}$  to enhance cation chelating effect and source of carbon-coating



1

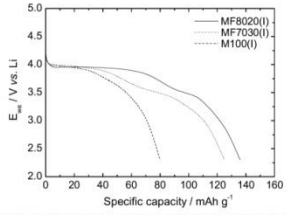
2

20 nm

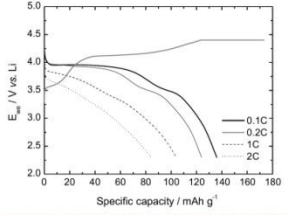
Confirm of carbon coated  $\text{LiMnPO}_4$  particles

### ELECTROCHEMICAL TESTS

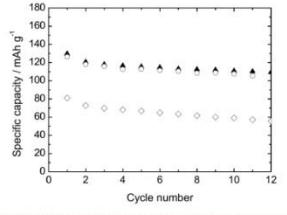
First discharge curves at 0.1C and 50°C of fully charged electrodes based on materials from *synthesis (I)*



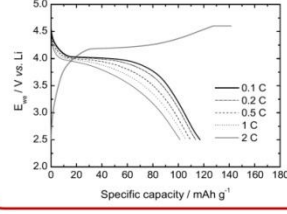
Discharge capability from 0.1C to 2C of fully charged MF8020(I) electrode, at 50°C.



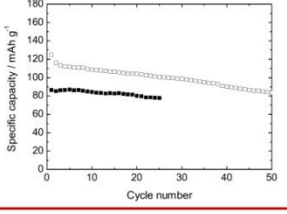
Specific discharge capacity at 0.1C and 50°C of (◇) M100(I), (▲) MF8020(I), and (○) MF7030(I)



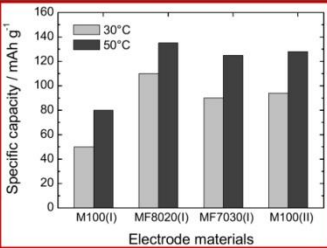
Discharge capability from 0.1C to 2C of fully charged *M100(II)* electrode at 50°C



Specific discharge capacity at 0.1C at 50°C (□) and 30°C (■) of M100(II)



Comparison of the 1<sup>st</sup> discharge capacity of the fully charged electrodes, at 30° and 50°C



**CONCLUSIONS:** Carbon-coated  $\text{LiMnPO}_4$  and  $\text{LiMn}_{1-x}\text{Fe}_x\text{PO}_4$  ( $x=0.2, 0.3$ ) were prepared. Synthesis (II) of  $\text{LiMnPO}_4$  from totally soluble precursors provided an attractive carbon-coated material with the following performance at 0.1C:  $125 \text{ mAh g}^{-1}$  at 50°C and  $95 \text{ mAh g}^{-1}$  at 30°C, and a capacity fade per cycle of 0.5% at 50°C and 0.4% at 30°C. These results are very promising, particularly in consideration of the inexpensive synthesis procedure, and evidence that a well performing Mn-based olivine is viable and this is an advantage for battery energy because of the most charge is delivered at a voltage higher than 3.5 V.

**REFERENCES**

[1] H. Ji et al., *Electrochimica Acta* 2011, 56, 3093–3100  
[2] L. Damen et al., submitted to *Journal of Power Sources*

Project funded by ENEA and Italy's Ministero dello Sviluppo Economico under the program "Ricerca di sistema elettrico"



# Ionic Liquid-based Li / O<sub>2</sub> Batteries

Simone Monaco, Francesca Soavi, Marina Mastragostino  
 Università di Bologna, Dipartimento di Chimica "Giacomo Ciamician"  
 Via Selmi 2, 40126 Bologna, Italy  
 simone.monaco2@unibo.it



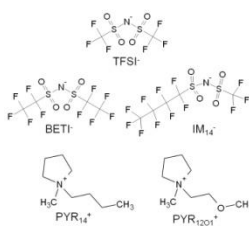
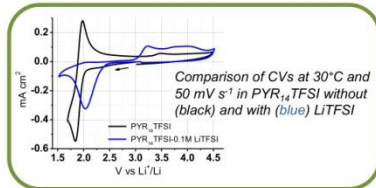
In the frame of the European LABOHR Project the oxygen redox reaction (ORR) in pyrrolidinium-based ionic liquids (ILs) without and with lithium bis(trifluoromethanesulfonyl)imide (LiTFSI) has been investigated at different temperatures for Li/O<sub>2</sub> batteries which are a breakthrough in battery technology for powering long-range electric vehicles. The viability of high efficiency, rechargeable Li/O<sub>2</sub> battery is demonstrated by the use of catalyst-free mesomacroporous carbon cathode that features a high specific capacity of 2500 mAh g<sup>-1</sup> and, more importantly, a recharge potential lower than 3.8 V vs Li<sup>+/</sup>Li that prevents detrimental secondary reactions. The effect of O<sub>2</sub> mass transport in ILs on the battery discharge process is also discussed.

www.labohr.eu

## O<sub>2</sub> redox in Ionic Liquids

ORR in IL without lithium salt is a quasi-reversible electrochemical process that involves superoxide formation as the first step.

The presence of lithium ions causes chemical reactions following the first electrochemical step of superoxide formation that even yields processes that involve formation of superoxide and insoluble products on the electrode surface.



Oxygen diffusion coefficient (D<sub>O</sub>), concentration (C<sub>O</sub>), heterogeneous rate constant (k<sup>0</sup>) and half-wave potential (E<sub>1/2</sub>) of ORR in ILs without lithium salt by CV and psCA at UME (GC electrodes)

IL	T °C	10 <sup>6</sup> D <sub>O</sub> cm <sup>2</sup> s <sup>-1</sup>	10 <sup>6</sup> C <sub>O</sub> mol cm <sup>-3</sup>	10 <sup>3</sup> k <sup>0</sup> cm s <sup>-1</sup>	E <sub>1/2</sub> V vs Li <sup>+/</sup> Li
PYR <sub>14</sub> TFSI	30°C	12	2.9	1.6	1.93
	60°C	27	2.1	3.7	1.90
PYR <sub>1(201)</sub> TFSI	30°C	11	3.0	1.2	2.12
	60°C	18	3.8	2.8	2.08
PYR <sub>14</sub> BET1	30°C	3	10.7	0.8	1.94
	60°C	8	7.8	2.1	1.90
PYR <sub>14</sub> IM <sub>14</sub>	30°C	2	14.3	0.5	1.99
	60°C	5	14.1	0.9	1.92

S. Monaco, A. M. Arangio, F. Soavi, M. Mastragostino, E. Paillard, S. Passerini, *Electrochimica Acta* 83 (2012) 94-104

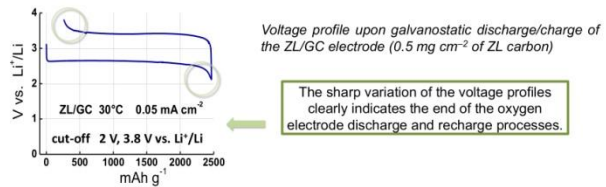
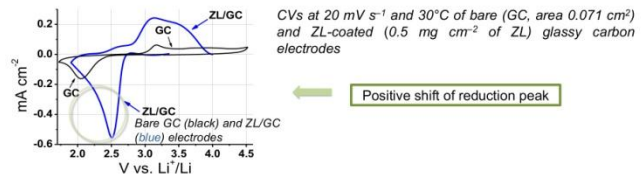
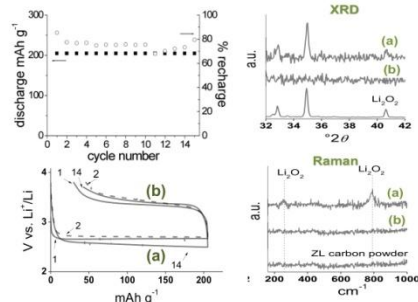
## Electrode screening

ZL/GC electrode: 95% carbon – 5% PVDF, 0.28 cm<sup>2</sup>; O<sub>2</sub>-saturated PYR<sub>14</sub>TFSI – 0.1 M LiTFSI (5 mL)

Cathode material disordered template meso-macroporous carbon (ZL carbon)

S <sub>BET</sub> m <sup>2</sup> /g	d nm	V <sub>2-200 nm</sub> cm <sup>3</sup> /g	V <sub>2-100 nm</sub> cm <sup>3</sup> /g	A <sub>2-100 nm</sub> m <sup>2</sup> /g
610	54	0.16	0.73	94

Discharge (■) specific capacity and recharge efficiency (○) and potential profiles over cycling of ZL/GC electrode (2 mg cm<sup>-2</sup> of ZL) at 0.08 mA cm<sup>-2</sup> with discharge time limited at 5 h and charge potential cut-off at 3.8 V vs. Li<sup>+/</sup>Li (labels indicate cycle numbers).



Meso-macroporous carbon obtained by a simple, low-cost template synthesis and PYR<sub>14</sub>TFSI-based electrolyte provide a real possibility for the development of rechargeable Li/O<sub>2</sub> batteries that can safely operate even above room temperature.

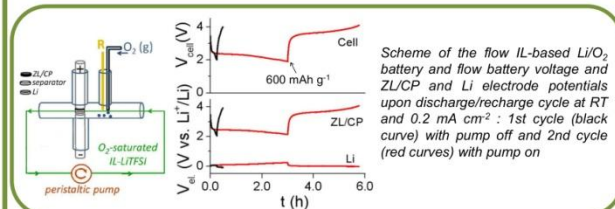
F. Soavi, S. Monaco, M. Mastragostino, *Journal of Power Sources* 224 (2013) 115-119

## O<sub>2</sub> mass transport limitation

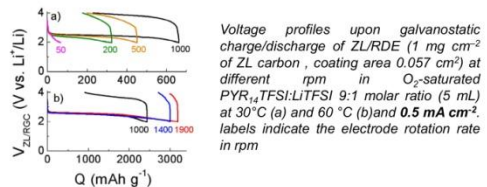
RDE at defined ω permits a fine control of the diffusion layer close to the electrode surface, causing a constant concentration gradient between this surface and the bulk of the solution. RDE discharge/charge galvanostatic cycles were performed to evaluate the limit of the specific capacity due to O<sub>2</sub> mass transport.

The oxygen electrode response in IL at high discharge currents is dominated by the O<sub>2</sub> properties in the electrolyte. O<sub>2</sub> mass transport in IL becomes crucial at fast discharge currents which are of interest for automotive applications.

It is possible to overcome intrinsic limitation of O<sub>2</sub> mass transport in IL by a novel flow-cell concept which is the core of the EU LABOHR Project.



S. Monaco, F. Soavi, M. Mastragostino *Journal of Physical Chemistry Letters* 4 (2013) 1379-1382



Acknowledgements: Work funded by the European Commission in the 7<sup>th</sup> Framework Programme FP7-2010-GC-ELECTROCHEMICAL STORAGE, contract no. 255971 "Lithium-Air Batteries with self Oxygen Harvesting and Redox processes" (LABOHR). All the partners of the LABOHR Project are acknowledged for the fruitful discussions on Li/O<sub>2</sub> batteries with ILs.



## List of Publications

L. Damen, F. De Giorgio, S. Monaco, F. Veronesi, M. Mastragostino *J. Power Sources* **2012**, *218*, 250–253 “Synthesis and characterization of carbon-coated LiMnPO<sub>4</sub> and LiMn<sub>1-x</sub>Fe<sub>x</sub>PO<sub>4</sub>(x = 0.2, 0.3) materials for lithium-ion batteries”

S. Monaco, A.M. Arangio, F. Soavi, M. Mastragostino, E. Paillard, S. Passerini *Electrochim. Acta* **2012**, *83*, 94–104 “An electrochemical study of oxygen reduction in pyrrolidinium-based ionic liquids for lithium/oxygen batteries”

F. Soavi, S. Monaco, M. Mastragostino *J. Power Sources* **2013**, *224*, 115–119 “Catalyst-free porous carbon cathode and ionic liquid for high efficiency, rechargeable Li/O<sub>2</sub> battery”

S. Monaco, F. Soavi, M. Mastragostino *J. Phys. Chem. Lett.* **2013**, *4*, 1379–1382 “Role of oxygen mass transport in rechargeable Li/O<sub>2</sub> batteries operating with Ionic Liquids”